

Resonance Ionization Spectroscopy of Atomic Uranium using Tunable Pulsed Dye Lasers

By

Pijush Kanti Mandal

(Enrolment No.: PHYS 01201304041)

Bhabha Atomic Research Centre, Mumbai

*A thesis submitted to the
Board of Studies in Physical Sciences
In partial fulfillment of requirements
for the Degree of*

DOCTOR OF PHILOSOPHY

of

HOMI BHABHA NATIONAL INSTITUTE, MUMBAI



October, 2018

Homi Bhabha National Institute

Recommendations of the Viva Voce Committee

As members of the Viva Voce Committee, we certify that we have read the dissertation prepared by **Pijush Kanti Mandal** entitled **Resonance Ionization Spectroscopy of Atomic Uranium using Tunable Pulsed Dye Lasers** and recommend that it may be accepted as fulfilling the thesis requirement for the award of Degree of Doctor of Philosophy.

Chairman - < **Dr. N. K. Sahoo** >



Date: 28/2/2019

Guide / Convener - < **Dr. Vas Dev** >



Date: 28/2/2019

Examiner - < **Prof. D. Narayana Rao** >



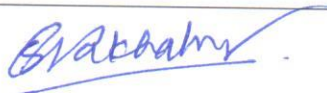
Date: 28.02.2019

Member 1- < **Dr. S. K. Dixit** >



Date: 28/02/2019

Member 2- < **Dr. S. G. Nakhate** >



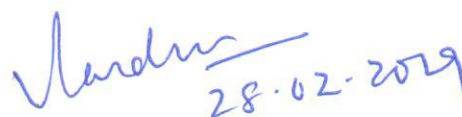
Date: 28/02/2019

Final approval and acceptance of this thesis is contingent upon the candidate's submission of the final copies of the thesis to HBNI.

I hereby certify that I have read this thesis prepared under my direction and recommend that it may be accepted as fulfilling the thesis requirement.

Date: 28-02-2019

Place: Mumbai



<Signature>

Guide

STATEMENT BY AUTHOR

This dissertation has been submitted in partial fulfillment of requirements for an advanced degree at Homi Bhabha National Institute (HBNI) and is deposited in the Library to be made available to borrowers under rules of the HBNI.

Brief quotations from this dissertation are allowable without special permission, provided that accurate acknowledgement of source is made. Requests for permission for extended quotation from or reproduction of this manuscript in whole or in part may be granted by the Competent Authority of HBNI when in his or her judgment the proposed use of the material is in the interests of scholarship. In all other instances, however, permission must be obtained from the author.

(Pijush Kanti Mandal)

DECLARATION

I, hereby declare that the investigations presented in the thesis have been carried out by me. The work is original and has not been submitted earlier as a whole or in part for a degree / diploma at this or any other Institution / University.

(Pijush Kanti Mandal)

List of Publications arising from the thesis

Journals

1. "Even-parity autoionizing levels of atomic uranium and their total angular momenta", **P. K. Mandal**, A. C. Sahoo, R. C. Das, M. L. Shah and Vas Dev, Applied Physics B **123**, 192 (2017).
2. "Understanding photoexcitation dynamics in a three-step photoionization of atomic uranium and measurement of photoexcitation and photoionization cross sections", **P. K. Mandal**, A. C. Sahoo, R. C. Das, M. L. Shah, A. K. Pulhani, K. G. Manohar and Vas Dev, Applied Physics B **120**, 751 (2015).
3. Radiative lifetimes, branching ratios and absolute transition probabilities of atomic uranium by delayed photoionization measurements", **P. K. Mandal**, R. C. Das, A. U. Seema, A. C. Sahoo, M. L. Shah, A. K. Pulhani, K. G. Manohar and Vas Dev, Applied Physics B **116**, 407 (2014).
4. "Observation of even-parity autoionization states of uranium by three-color photoionization optogalvanic spectroscopy in U-Ne hollow cathode discharges", **P. K. Mandal**, A. U. Seema, R. C. Das, M. L. Shah, Vas Dev and B. M. Suri, Journal of Quantitative Spectroscopy & Radiative Transfer **124**, 79 (2013).

Conferences

1. "Total angular momenta of even-parity autoionization levels of atomic uranium using laser photoionization polarization spectroscopy", **P. K. Mandal**, A. C. Sahoo, R. C. Das, M. L. Shah and Vas Dev, Proceedings of 25th DAE-BRNS National Laser Symposium (NLS-25), KIIT University, Bhubaneswar, Odisha, Dec. 20–23, (2016).
2. "Study of even parity autoionizing levels of atomic uranium and observation of Rydberg series converging to second ionizing limit", **P. K. Mandal**, A. C. Sahoo, R. C. Das, M. L. Shah, A. K. Pulhani, K. G. Manohar and Vas Dev, Proceedings of 24th DAE-BRNS National Laser Symposium (NLS-24), Raja Ramanna Centre for Advanced Technology, Indore, Dec. 2–5, 2015, (2015).
3. "Understanding photoexcitation dynamics in a multistep photoionization of U I using time resolved two- and three-color three-photon photoionization signals", **P. K. Mandal**, R. C. Das, A. C. Sahoo, M. L. Shah, A. K. Pulhani, K. G. Manohar and Vas Dev, Proceedings of 23rd DAE-BRNS National Laser Symposium (NLS-23), Sri Venkateswara University, Tirupati, Dec. 3–6, (2014).
4. "Measurement of Isotope Shifts of odd-parity high-lying levels of uranium by two-color photoionization optogalvanic spectroscopy in Hollow cathode discharge tube", **P. K. Mandal**, A. C. Sahoo, M. L. Shah, R. C. Das, A. K. Pulhani and Vas Dev, Proceedings of 23rd DAE-BRNS National Laser Symposium (NLS-23), Sri Venkateswara University, Tirupati, Dec. 3–6, (2014).

5. "Three-color photoionization optogalvanic spectroscopy in U-Ne hollow cathode discharges: Observation of even-parity autoionization states of uranium", **P. K. Mandal**, A. U. Seema, R. C. Das, M. L. Shah, Vas Dev and B. M. Suri, Proceedings of 21st DAE-BRNS National Laser Symposium (NLS-21), BARC, Mumbai, Feb. 6–9, (2013).
6. "Measurement of radiative lifetimes, branching ratios and absolute transition probabilities of atomic uranium by delayed photoionization technique", **P. K. Mandal**, R. C. Das, A. U. Seema, A. C. Sahoo, M. L. Shah, A. K. Pulhani, K. G. Manohar and Vas Dev, Proceedings of 21st DAE-BRNS National Laser Symposium (NLS-21), BARC, Mumbai, Feb. 6–9, (2013).

Other publications not included in the thesis

1. "Radiative lifetimes of even-parity high-lying levels of Sm I by delayed photoionization measurements", A. U. Seema, **P. K. Mandal**, A. C. Sahoo, M. L. Shah, G. K. Bhowmick and Vas Dev, Journal of Quantitative Spectroscopy & Radiative Transfer, **216**, 1 (2018).
2. "Blue Fluorescence as a Frequency Offset Reference in the Rubidium 5S-5P-5D Transition", **P. K. Mandal**, V. Naik, Vas Dev, A. Chakrabarti, And A. Ray, Applied Optics, 57, 13 / 1, (2018).
3. "The Blue Light in a Ladder System: from Double Resonance Optical Pumping to Autler-Townes Splitting", W. Raja, **P. K. Mandal**, V. Naik, A. Chakrabarti, A. Ray, The European Physical Journal D, 72, 123 (2018).
4. "Effect of magnetic field on isotope-selective photoionization of atomic samarium using polarized lasers", A. C. Sahoo, **P. K. Mandal**, M. L. Shah, R. C. Das and Vas Dev, Journal of Physics Communications **1**, 055010 (2017) .
5. "Polarization-based isotope-selective two-color photoionization of atomic samarium using broadband lasers", A.U. Seema, Asawari D. Rath, **P.K. Mandal**, Vas Dev, Applied Physics B **118**, 505 (2015).
6. "New even-parity high-lying levels of Sm I and measurement of isotope shifts by two-color resonance ionization mass spectrometry", A.U.Seema, **P.K. Mandal**, Asawari D. Rath and Vas Dev, Journal of Quantitative Spectroscopy & Radiative Transfer, **145**, 197 (2014).

(Pijush Kanti Mandal)

Dedicated to.....

.....all my Teachers

ACKNOWLEDGEMENTS

I would like to express my deepest gratitude and respect to my guide **Prof. Vas Dev** for his able guidance, mentorship, encouragements and wonderful support throughout the course of this work. I would also like to thank him for introducing me to the field of laser spectroscopy.

I am grateful to my colleagues **Dr. M. L. Shah, Dr. R. C. Das, and Shri. A. C. Sahoo** for their sustained cooperation in conducting experiments, valuable suggestions and discussions throughout this work. I sincerely thank **Shri. G. R. Zende** for preparation of the U-Ne hollow cathode discharge tube. I am thankful to **Shri. D. R. Rathod** and **Smt. B. K. Sodhi** for technical support. I am grateful to **Shri. N. O. Kawade** for developing data acquisition system and pulsed power supply for the present work. I am indebted to **Smt. A. U. Seema** for valuable suggestions, generous cooperation and tireless support throughout the work, especially during preparation of the thesis. I am thankful to **Dr. A. D. Rath** and **Smt. Jigyasa** for providing achromatic quarter and half wave plates for the experiments. I sincerely thank **Dr. M. L. Shah** and **Dr. K. G. Manohar** whose doctoral thesis was helpful during preparation of the thesis.

I am grateful to **Shri. R. K. Rajawat, AD BTDG & Head L&PTD**, for the encouragement and support. I am grateful to **Dr. D. J. Biswas, Dr. A. K. Ray, Dr. J. Mukherjee, Dr. B. M. Suri, Dr. G. P. Gupta, Dr. K. G. Manohar, and Dr. B. N. Jagatap** for their encouragement and fruitful discussions.

I am grateful to my present and previous doctoral committee members **Prof. N. K. Sahoo, Prof. S. G. Nakhate, Prof. S. K. Dixit** and **Prof. A. K. Das, Prof. P. A. Naik, Prof. K. Dasgupta** for their constructive criticism and suggestions. I sincerely thank **Prof. B. K. Nayak**, Dean Academic, Physical and Mathematical Sciences, HBNI for his encouragement and timely support.

I sincerely thank **Dr. S. Kumar, Dr. A. K. Pulhani, Dr. J. P. Nilaya, Shri. S. Sethi, Shri. A. Majumder, Dr. V. S. Rawat, Dr. G. Sridhar, Dr. A. D. Rath, Dr. S. Pradhan, Dr. B. Jana, Shri. Paramjit, Shri. A. K. Tiwari, Shri. S. P. Sahoo, and Shri. S. K. Agarwalla** for their cooperation during this work.

I am thankful to **workshop staffs, office staffs** and **colleagues** of Laser and Plasma Technology Division for support and cooperation during the whole PhD tenure.

I would like to thank **Dr. Ayan Ray** for his encouragement and support during preparation of the thesis. I sincerely acknowledge the support rendered by **Dr. Suvendhu Jena** during preparation of the thesis.

It is my pleasure to acknowledge the ever willing moral support rendered by my friends **Ayan, Tanay, Sreemoyee, Pratap, Somnath, Biswaranjan, Partha, Manish, Hirakendu, Santanu, Nurauddin, Kajal, Subrata** throughout the course of this work.

I would like to express my heartfelt gratitude to my school teachers (**Shri. T. K. Mandal, Md. A. Hossain, Shri. J. Mandal, Shri. K. Pramanick, Shri. S. Pramanick**) and Professors (**Dr. P. Datta, Dr. M. Bhattacharya, Dr. S. P. Khastgir, Dr. P. K. Datta**) right from my primary level to the Masters degree for their blessings and moral support.

I am extremely grateful to my mother **Smt. Pritikana Mandal**, father **Shri. Paritosh Mandal**, mother-in-law **Smt. Pampa Hazra** and father-in-law **Shri. Probir Kumar Hazra** for their moral support and everlasting blessings. A special thanks to my sisters (**Paly and Pampa**), brother-in-law (**Dipankar**), niece (**Diptasree**) for their love and continuous support. I am especially thankful to my wife **Priyanka** for her endless support, love and inspiration.

Finally, I am grateful to **all** those who have supported me in the completion of this thesis. I apologize for any inadvertent omissions.

CONTENTS

	Page No.
SYNOPSIS	xvi
LIST OF FIGURES	xxvi
LIST OF TABLES	xxxii
CHAPTER 1 - INTRODUCTION.....	1
1.1 INTRODUCTION TO SPECTROSCOPY	1
1.2 SPECTROSCOPIC TECHNIQUES	2
1.2.1 SPECTROSCOPIC TECHNIQUES WITH TUNABLE LASERS.....	3
1.2.1 A) ABSORPTION SPECTROSCOPY	5
1.2.1 B) OPTOGALVANIC SPECTROSCOPY	6
1.2.1 C) LASER INDUCED FLUORESCENCE SPECTROSCOPY	7
1.2.1 D) RESONANCE IONIZATION SPECTROSCOPY.....	7
1.3 ATOMIC URANIUM AND ITS SPECTROSCOPIC IMPORTANCE.....	10
1.4: A LITERATURE REVIEW ON THE SPECTROSCOPY OF URANIUM AND SCOPE OF THE PRESENT WORK	11
1.5 ORGANIZATION OF THE THESIS	14
CHAPTER 2 - EXPERIMENTAL SET-UP.....	17
2.1 INTRODUCTION	17
2.2 LASER SYSTEMS	18
2.3 TIME-OF-FLIGHT MASS SPECTROMETER (TOF-MS)	20
2.3.1 WORKING PRINCIPLE	21
2.3.2 TEMPORAL WIDTH OF THE ION SIGNAL	22
2.3.2.A) EFFECT OF INITIAL VELOCITY DISTRIBUTION OF IONS ON THE TEMPORAL WIDTH	23
2.3.2.B) EFFECT OF SPATIAL DISTRIBUTION OF IONS ON THE TEMPORAL WIDTH.....	24
2.4 U-NE HOLLOW CATHODE DISCHARGE TUBE	25
2.5 SIGNAL MONITORING AND PROCESSING DEVICES	26
2.5.1 PHOTODIODE.....	26
2.5.2 FABRY-PEROT ETALON (FPE).....	27

2.5.3 DIGITAL STORAGE OSCILLOSCOPE.....	29
2.5.4 LASER POWER METER	29
2.5.5 WAVELENGTH METER.....	29
2.5.6 FAST PRE-AMPLIFIER.....	30
2.5.7 BOX-CAR AVERAGER.....	30
CHAPTER 3 - NUMERICAL STUDY OF PHOTOEXCITATION DYNAMICS	
USING POPULATION RATE EQUATIONS	31
3.1 INTRODUCTION	31
3.2 POPULATION RATE EQUATIONS.....	32
3.2.1 SINGLE STEP PHOTOEXCITATION IN A CLOSED TWO-LEVEL SYSTEM.....	33
3.2.1.1 EXCITATION BY PULSED LASER.....	35
3.2.1.2 EFFECTS OF BRANCHING RATIOS AND RADIATIVE LIFETIMES.....	36
3.2.1.3 SATURATION OF TRANSITIONS FOR DIFFERENT CROSS SECTIONS	37
3.2.2 SINGLE STEP PHOTOIONIZATION IN AN OPEN TWO-LEVEL SYSTEM.....	38
3.2.3 THREE-STEP PHOTOIONIZATION.....	39
3.2.3.1 POPULATION RATE EQUATIONS FOR THREE-STEP PHOTOIONIZATION PATHWAYS.....	40
3.2.3.2 TEMPORAL EVOLUTION OF ATOMIC POPULATIONS AMONG VARIOUS LEVELS.....	42
3.2.3.3 DEPENDENCE OF PHOTOIONIZATION YIELD ON LASER FLUENCE/PULSE ENERGY	44
3.2.4 EFFECTS OF LASER POLARIZATION ON THE SATURATION CURVE/PHOTOIONIZATION EFFICIENCY.	46
3.2.5 CALCULATION OF PHOTOIONIZATION EFFICIENCY IN UNITS OF SATURATION FLUENCE/ENERGY	49
CHAPTER 4 - DETERMINATION OF TRANSITION PROBABILITIES OF ATOMIC URANIUM BY MEASURING RADIATIVE LIFETIMES AND BRANCHING RATIOS USING DELAYED PHOTOIONIZATION METHOD	51
4.1 INTRODUCTION	51

4.2 PRESENT WORK ON THE MEASUREMENT OF RADIATIVE LIFETIMES AND BRANCHING RATIOS	57
4.2.1 EXPERIMENTAL DETAILS	57
4.2.2 RESULTS AND DISCUSSIONS.....	58
4.2.2.1 LIFETIME MEASUREMENT	58
4.2.2.2 BRANCHING RATIO MEASUREMENT	60
CHAPTER 5 - MEASUREMENT OF EXCITED-LEVEL TO EXCITED-LEVEL TRANSITION PROBABILITIES AND PHOTOIONIZATION CROSS SECTIONS OF EXCITED LEVELS OF ATOMIC URANIUM BY SATURATION METHOD.....	68
5.1 INTRODUCTION	68
5.2 PRESENT WORK ON PHOTOEXCITATION AND PHOTOIONIZATION CROSS SECTION MEASUREMENTS USING SATURATION METHOD	70
5.2.1 EXPERIMENTAL DETAILS	71
5.2.2 RESULTS AND DISCUSSION	73
5.2.2.1 MEASUREMENT OF PHOTOEXCITATION CROSS SECTION OF THE FIRST STEP TRANSITION.....	73
5.2.2.2 MEASUREMENT OF PHOTOIONIZATION CROSS SECTIONS OF EXCITED LEVELS (THIRD STEP TRANSITIONS) OF URANIUM.....	76
5.2.2.3 MEASUREMENT OF EXCITED-LEVEL-TO-EXCITED-LEVEL TRANSITION PROBABILITIES AND PHOTOIONIZATION CROSS SECTIONS	78
5.2.2.3 A) NUMERICAL ANALYSIS USING POPULATION RATE EQUATIONS.....	79
5.2.2.3 B) SIMULTANEOUS DETERMINATION OF SECOND AND THIRD STEP CROSS SECTION AT λ_2	82
5.2.2.3 C) INVESTIGATION OF TWO-COLOR THREE-PHOTON PHOTOIONIZATION SPECTRA	87
5.2.2.3 D) OBSERVATION OF DEPLETION OF POPULATION IN THE SECOND EXCITED LEVEL DUE TO TWO-COLOR THREE-PHOTON PHOTOIONIZATION	89
CHAPTER 6 -THREE-COLOR PHOTOIONIZATION SPECTROSCOPY OF ATOMIC URANIUM: DETERMINATION OF ENERGY VALUES AND	

TOTAL ANGULAR MOMENTA OF EVEN-PARITY AUTOIONIZING LEVELS.....	91
6.1 INTRODUCTION	91
6.1.1 ORIGIN OF AUTOIONIZING LEVELS	92
6.1.2 DECAY OF AUTOIONIZING LEVELS.....	93
6.1.3 STRENGTH OF AUTOIONIZING RESONANCE	94
6.1.4 SHAPES OF THE AUTOIONIZING RESONANCES	94
6.1.5 VALENCE AND RYDBERG AUTOIONIZING LEVELS	95
6.2 LITERATURE SURVEY ON THE STUDY OF AUTOIONIZING LEVELS AND ANGULAR MOMENTA OF ATOMIC URANIUM.....	96
6.2.1 AUTOIONIZING LEVELS.....	96
6.2.2 TOTAL ANGULAR MOMENTA	97
6.3 PRESENT STUDY OF AUTOIONIZING LEVELS AND THEIR ANGULAR MOMENTA	98
6.3.1 EXPERIMENTAL DETAILS	98
6.3.2 THEORETICAL: CALCULATIONS OF PHOTOIONIZATION YIELD FOR DIFFERENT COMBINATIONS OF LASER POLARIZATIONS	100
6.3.3 RESULTS AND DISCUSSION	104
6.3.3.1 STUDY OF PHOTOIONIZATION SPECTRA	104
6.3.3.2 DETERMINATION OF J-VALUES.....	119
6.3.3.3 ANALYSIS OF RYDBERG SERIES	121
CHAPTER 7 - RESONANCE IONIZATION SPECTROSCOPY OF ATOMIC URANIUM IN U-NE HOLLOW CATHODE DISCHARGE	125
7.1 INTRODUCTION	125
7.2 EXPERIMENTAL SETUP	127
7.2.1 CHARACTERIZATION OF THE CATHODE DARK SPACE	131
7.3 STUDY OF AUTOIONIZING LEVELS USING THREE-COLOR THREE-PHOTON PIG SPECTROSCOPY	133
7.4 MEASUREMENT OF ISOTOPE SHIFT OF ODD-PARITY HIGH LYING LEVELS (SECOND EXCITED LEVELS)USING TWO-COLOR PIG SPECTROSCOPY	137
7.5 MEASUREMENT OF PHOTOEXCITATION/PHOTOIONIZATION CROSS SECTION OF ATOMIC URANIUM	141

CHAPTER 8 - CONCLUSIONS AND FUTURE SCOPE OF THE WORK.....	143
APPENDIX-1: RADIATIVE LIFETIMES	148
APPENDIX-2: RADIATIVE LIFETIME OF CLASSICAL ATOM.....	149
APPENDIX-3: BRANCHING RATIO.....	150
APPENDIX-4: TRANSITION PROBABILITY	150
APPENDIX-5: PHOTOEXCITATION CROSS SECTION.....	152

Synopsis

Resonance ionization spectroscopy (RIS), owing to its high sensitivity and selectivity, is an excellent tool to study the complex electronic structure of atoms and molecules. RIS has played an important role in the measurement of atomic parameters such as energy level values, total angular momenta, radiative lifetimes, branching ratios, transition probabilities, photoionization cross sections, isotope shifts, hyperfine structures etc., especially, in the high energy regions [1-5] which are not accessible with the conventional spectroscopic techniques. In RIS, atoms are selectively excited up in the ladder of energy levels using resonant lasers in a stepwise manner before ionized. Number of lasers and excitation steps depend on the ionization potential and energy level structure of the atoms and the photon energy of the lasers. The RIS in combination with mass spectrometry has given birth to a still more powerful technique, known as Resonance Ionization Mass Spectrometry (RIMS). This technique offers mass selectivity in addition to the spectral selectivity achieved in RIS process. This enables RIMS application in ultra-sensitive trace detection of elements/isotopes, with minimum isotopic/isobaric interferences [6,7].

Accurate information on the abovementioned atomic parameters is a prerequisite to get deeper insight into basic atomic physics as well as to develop novel photoionization processes in applied research. For example, information on energy level values, transition wavelengths, transition probabilities are useful to understand the structure of atom using adequate theories or models. In addition transition probabilities play a key role in many areas of science such as, laser physics - to identify new laser materials, in astrophysics - to determine the abundance of elements in the solar system and in laser based applications like trace analysis of elements/isotopes, laser isotope separation etc. Isotope shift and hyperfine structure provide information about nuclear size, shape, magnetic dipole and electric quadrupole moments etc. Similarly, information on photo-excitation and photoionization

cross sections is important while selecting an efficient photoionization wavelength scheme and in quantifying the photoionization process.

Uranium ($Z = 92$) is the heaviest naturally available element in the actinide series of the periodic table having ground state electronic configuration $[\text{Rn}] 5f^3 6d7s^2$ [3]. Due to the presence of six valence electrons in its outer shell the atomic spectra of uranium is very complex. Because of its applications in nuclear industry uranium atom has been a subject of intense spectroscopic investigations over many decades [3-5, 8-10]. However, spectroscopic information on uranium available in the literature is far from complete.

The ionization potential (I.P) of uranium is 6.19 eV [5] and hence at least three photons of energy $\sim 2\text{eV}$ each (photon energy in the visible region), are required to ionize the neutral uranium atom. The simplest photoionization scheme is a single-color three-photon, where laser wavelength is tuned in resonance or near resonance to at least one of the transitions of the atom. Although this is not an efficient pathway for photoionization due to involvement of near resonant transitions, but it is useful to achieve elemental selectivity as these transitions are characteristic of an element. For obtaining isotopic selectivity, generally, two- or three-color photoionization schemes are used. In a photoionization scheme, the efficiency of the process is mainly decided by the choice of the final step transition, as the intermediated transitions, which are between bound states, can easily be saturated due to very large excitation cross sections. The final step transition can be a non-resonant transition terminating into continuum or a resonant transition to an autoionizing level. Since autoionizing levels are discrete/bound levels embedded in the continuum, the excitation of atoms to these levels is preferred over the transitions terminating into the continuum as its cross sections are higher than the later one. Also, similar high cross section in the final step transition can be realized through excitation into Rydberg states and ionization via collisions with inert gas atoms or by using delayed pulsed electric field or by using infrared laser etc. [1,

4]. However, in this case the requirement of additional equipments increases the complexity of the experimental setup. On the contrary, by using autoionizing level as the final level, almost 100% ionization efficiency can be realized without any additional instrumentation [1, 2]. Due to the presence of many electrons in the outer shell, the uranium atom exhibits dense autoionization spectra. Therefore, to construct an efficient and isotope selective photoionization scheme, a detailed knowledge of all the spectroscopic parameters such as atomic energy levels including autoionizing levels, J-values, transition probabilities/cross sections, branching ratios, radiative lifetimes, isotope shifts, and hyperfine structures, etc. is required.

The focus of this thesis is on the measurements of various spectroscopic parameters of atomic uranium using resonance ionization spectroscopy. The measurements of atomic parameters have been carried out in an atomic beam coupled with a time-of-flight mass spectrometer (TOF-MS) using Nd:YAG pumped dye lasers. As an alternate to the complex experimental setup consisting of an atomic beam source and a TOF-MS, the photoionization spectroscopy of uranium has also been carried out in a U-Ne hollow cathode discharge tube (HCDT), a simpler device, where HCDT is used as a source of spectroscopic grade atomic vapors as well as photoion/photoelectron detector. In this case, since the photoionization is detected as a variation in the discharge current, the technique is known as photoionization optogalvanic (PIOG) spectroscopy. It is basically a resonance ionization spectroscopy which is carried out in the cathode dark space of the HCDT.

The research work carried out and compiled here in the form of thesis has been published in four peer reviewed journals. An overview of the thesis contents grouped under eight chapters is as follows:

Chapter 1 begins with general introduction to spectroscopy. The problems and limitations associated with conventional absorption and emission spectroscopy techniques for

studying atomic structure have been discussed. Various laser based spectroscopic techniques have been discussed. Special emphasis has been given on resonance ionization spectroscopy and its applications. A brief literature survey on the spectroscopy of atomic uranium and its importance has been discussed. Organization of the thesis is presented at the end of this chapter.

Chapter 2 contains the details of the experimental setup used for carrying out resonance ionization spectroscopy of atomic uranium. It consists of various subsystems like Nd:YAG pumped Dye lasers, time-of-flight mass spectrometer (TOF-MS), hollow cathode discharge tube (HCDDT), box car averager (BCA), photo diode, Fabry-Perot etalon (FPE), oscilloscope etc. The working principle and specifications of the equipments used for atomic parameter measurements has been discussed in detail.

Chapter 3 deals with the numerical study of excitation dynamics in a three-step photoionization process using population rate equations. Study of the excitation dynamics in a multi-step photoionization process is essential to understand the role of various atomic parameters such as radiative lifetime, branching ratio, transition probability, photoexcitation, photoionization cross section and various laser parameters like laser linewidth, state of polarization, laser energy density, temporal delays among laser pulses etc. on the photoionization yield. Assuming certain atomic and laser parameters, photoionization yield as a function of laser photon fluence (saturation curve) have been studied numerically for all the transitions of a three-step photoionization scheme for both synchronous and delayed laser pulses. Effect of laser polarization on the photoionization yield has also been discussed.

Chapter 4 describes the measurements of branching-ratios and radiative lifetimes of atomic uranium by employing three-step delayed photoionization method. Radiative lifetime (τ), branching ratio (β) and transition probability (A) are important parameters of an atomic system. Transition probability is related to the radiative lifetime and branching ratio by the

expression $A=\beta/\tau$. Conventionally, transition probabilities are obtained either from the measurement of line strengths in the emission spectra acquired from arcs, sparks or discharge lamps or from the measurement of absolute absorption. The accuracy of these measurements is limited by the uncertainties associated with source temperature, relative emission intensities over wide wavelength range, atomic vapour density and its profile, path length, self absorption etc. Generally, β is obtained using Fourier transform spectroscopy and τ is measured independently [11]. In this method complete understanding of the emission spectra is necessary for accurate measurement of absolute transition probability. Branching ratio can also be measured using laser induced fluorescence [12]. However, one disadvantage of this method is that a large number of undetected infrared transitions, particularly in case of uranium may result in over estimation of transition probabilities. Carlson et al. [13] have developed an alternative method of measuring absolute transition probability based on the delayed photoionization technique which is not subjected to these difficulties. Using the same method, radiative lifetimes of ten even-parity energy levels of atomic uranium in the 15,500-19,000 cm^{-1} region and branching ratios of six transitions, starting either from the ground state (5L_6) or from the lowest metastable state (5K_3) at 620.32 cm^{-1} have been measured. By combining the measured values of radiative lifetimes and branching ratios absolute transition probabilities of six transitions have been determined [14]. Possible sources of error in these measurements and their remedies are also discussed. The details of the measurements and results are discussed in this chapter. However, due to the finite lifetime of the lower level of the second step transition, which results in poor signal to noise ratio, the measurement of branching ratio for second step transition by this method is rather difficult.

Chapter 5 describes the measurements of excited-level to excited-level transition probabilities and photoionization cross sections of atomic uranium using saturation method.

In this method, saturation in the photoionization yield is studied as a function of the laser photon fluence by keeping all other experimental parameters constant, and the resultant saturation curve is fitted with the solution of the population rate equations to extract the cross section values. Measurement of cross section becomes simpler when each transition of a three-step photoionization process can be considered separately i.e. each transition can be assumed to be an independent two-level system [3]. Such two-level systems were realized by temporally separating the laser pulses. However, in cases where the two-color three-photon ($\lambda_1 + 2\lambda_2 > \text{I.P.}$) process leads to photoionization; the assumption of an independent two level system for the second step is not valid. Here, λ_1 and λ_2 are the first and second step laser wavelength in energy units. In this case, there exist two different photoionization pathways: such as two-color three-photon and delayed three-color three-photon from the second excited levels. In such cases, detailed investigation of photoexcitation dynamics is necessary to obtain second-step cross section/transition probability.

Photoexcitation dynamics in a three-step photoionization of atomic uranium has been investigated using time-resolved two-color three-photon and delayed three-color three-photon photoionization signals. Dependence of both the signals on the second-step laser photon fluence is studied. Excited-level-to-excited-level photoexcitation cross section and photoionization cross section from the second-excited level are simultaneously determined by analyzing the two-color three-photon and three-color three-photon photoionization signals using population rate equation model. Using this methodology, photoexcitation and photoionization cross sections for seven values of the second-step laser wavelength have been measured [15]. From the measured values of the photoexcitation cross sections, the excited-level-to-excited-level transition probabilities have been obtained and compared these with the values reported in the literature. Detailed investigations of photoexcitation dynamics are presented in this chapter.

Chapter 6 presents an exhaustive study of autoionizing levels of atomic uranium in the energy region up to $1,550 \text{ cm}^{-1}$ above the ionization limit. The study of autoionizing levels and their total angular momenta is important to understand the complex atomic structure of multi-electron system, in basic research and more importantly in applied research, to identify efficient ionization pathways for elemental ultra-trace analysis and isotope selective photoionization processes. Since bound-to-bound transitions are generally strong, the photoionization pathways involving a resonant last-step transition terminating into an autoionizing (AI) level are preferred over those terminating into continuum. Photoionization spectra were measured using more than 10 different second excited levels. A detailed analysis of the photoionization spectra has revealed a large number of even-parity autoionizing levels including 199 new levels and a Rydberg series converging to the second lowest ionic level (${}^6\text{L}_{11/2}$) of uranium. The details of the investigations on the three-color photoionization spectra are presented in this chapter.

In addition to the level structure, the total angular momentum (J) is another important atomic parameter which determines the photoionization (PI) yield in a multi-step photoionization process. Therefore, information on the J-value of AI levels, particularly, when polarized laser is used in the photoionization process, is must as it decides the participation of number of magnetic sublevels in the process and the transition strength between the lower and upper magnetic sublevels. The J-values of AI levels are generally determined by exciting the level of interest from three different lower levels having J-values, J-1, J and J+1, based on the total angular momentum selection rules, i.e. $\Delta J = 0, \pm 1$ (J = 0 to J = 0 being not allowed). In a complex atom like uranium, where density of AI levels is very high and spectra are overlapping, the determination of J-values using J-selection method is generally cumbersome. Green et al. [16] have developed an alternative method based on laser polarization combination to determine J-values. In this method, experimentally obtained

photoionization yield pattern for different combination of laser polarizations used in the three-step process is compared with that of theoretically calculated yield pattern to determine the J-values. By using both the methods, the J-values of large number of autoionizing levels have been assigned unambiguously [17]. The J-values determined in these studies along with the values previously reported in the literature are presented in this chapter.

Chapter 7 describes three-color photoionization spectroscopy of atomic uranium using photoionization optogalvanic (PIOG) spectroscopy technique. Previously, Levesque et al. [18] have demonstrated the use of the PIOG technique to perform single color three-photon photoionization spectroscopy of uranium. Vas Dev et al. [19] have used two-color three-photon PIOG spectroscopy for studying high-lying bound and autoionizing levels of atomic uranium. The PIOG technique has now been extended for three-color photoionization spectroscopy. Using this technique, photoionization spectra of uranium have been investigated systematically in the energy region 52,150-52,590 cm^{-1} i.e. 2,200 cm^{-1} above the first ionization potential, through three different excitation pathways, originating from its ground state, 0 cm^{-1} (5L_6). Analysis of the photoionization spectra have resulted in identification of large number of even-parity autoionizing levels and for few of them J-values have been assigned unambiguously [20]. To explore the potential of PIOG spectroscopy technique, the photoexcitation/photoionization cross sections of a three-step photoionization scheme and isotope shift of high-lying odd-parity levels have been measured as a test case and compared with the measurements performed in the atomic beam coupled with TOF-MS.

Finally, the important conclusions from the present studies and scope for future work are summarized in Chapter 8.

References

1. V. S. Letokhov, V. I. Mishin and A. A. Poretzky: Prog. Quant. Electr. **5**, 139 (1977).
2. G. S. Hurst, M. G. Payne, S. D. Kramer, and J. P. Young, Rev. Mod. Phys. **4**, 767 (1979).
3. L.R. Carlson, J.A. Paisner, E.F. Worden, S.A. Johnson, C.A. May, R.W. Solarz, J. Opt. Soc. Am. **66**, 846 (1976)
4. R.W. Solarz, C.A. May, L.R. Carlson, E.F. Worden, S.A. Johnson, J.A. Paisner, L.J. Radziemski, Phys. Rev. A **14**, 1129 (1976).
5. A. Coste, R. Avril, P. Blanchard, J. Chatelet, D. Lambert, J. Legre, S. Liberman, J. Pinard, J. Opt. Soc. Am. **72**, 103 (1982).
6. H.-J. Kluge, Acta Physica Polonica A, **86**, 159 (1994).
7. C. Grüning, G. Huber, P. Klopp, J.V. Kratz, P. Kunz, G. Passler, N. Trautmann, A. Waldek, K. Wendt, Int. J. Mass spectrom. **235**, 171 (2004).
8. M. Miyabe, M. Oba and I. Wakaida: J. Phys. B: At. Mol. Opt. Phys. **33**, 4957 (2000).
9. M. Miyabe, C. Geppert, M. Oba, I. Wakaida and K. Wendt, J Phys B: At Mol Phys. **35**, 3865 (2002).
10. P. G. Schumann, K. D. A. Wendt and B. A. Bushaw, Spectrochem. Acta Part B **60**, 1402 (2005).
11. S. E. Bisson, E. F. Worden, J. G. Conway, B. Comaskey, J. A. D. Stockdale, F. Nehring, J. Opt. Soc. Am. B **8**, 1545 (1991).
12. A. Petit, R. Avril, D. L'Hermite, A. Pailloux, Phys. Scr. **T100**, 114 (2002).
13. L. R. Carlson, S. A. Johnson, E. F. Worden, C. A. May, R.W.Solarz, J. A. Paisner, Opt. Commun. **21**,116 (1977).
14. **P. K. Mandal**, R. C. Das, A. U. Seema, A. C. Sahoo, M. L. Shah, A. K. Pulhani, K. G. Manohar and Vas Dev, Appl. Phys. B **116**, 407 (2014).

15. **P. K. Mandal**, A. C. Sahoo, R. C. Das, M. L. Shah, A. K. Pulhani, K. G. Manohar and Vas Dev, Appl. Phys. B **120**, 751 (2015).
16. P. T. Greenland: J. Phys. B: At. Mol. Opt. Phys. **21**, 4117 (1988).
17. **P. K. Mandal**, A. C. Sahoo, R. C. Das, M. L. Shah and Vas Dev, Appl. Phys. B **123**, 192 (2017).
18. S. Levesque, J.-M. Gagne and F. Babin, Can J Phys. **76**, 207 (1998).
19. Vas Dev, M. L. Shah, A. K. Pulhani and B. M. Suri, Appl Phys B. **80**, 587 (2005).
20. **P. K. Mandal**, A. U. Seema, R. C. Das, M. L. Shah, Vas Dev and B. M. Suri, J. Quant. Spectrosc. Radiat. Transfer **124**, 79 (2013).

List of figures

Fig. 1.1:	Different types of photoionization pathways of atoms: a) single-color two-photon, b) two-color two-photon via autoionizing level, c) two-color two-photon via Rydberg level, d) near resonant single-color three-photon, e) two-color three-photon, f) three-color three-photon via autoionizing level, g) three-color three-photon via Rydberg level. Ionization of Rydberg level is done by using external electric field, inexpensive laser photons or through atom-atom collisions.....	9
Fig. 2.1:	Schematic of experimental set-up.....	17
Fig. 2.2:	Laser systems used in resonance ionization spectroscopy of atomic uranium.	18
Fig. 2.3:	Time-of-flight mass spectrometer used in resonance ionization spectroscopy of atomic uranium.	21
Fig. 2.4:	Schematic of the time-of-flight mass spectrometer (TOF-MS).....	22
Fig. 2.5:	Typical photoionization signal of $^{238}\text{U}^+$ in TOF-MS.	23
Fig. 2.6:	U-Ne HCDT used for photoionization optogalvanic spectroscopy of uranium.	25
Fig. 2.7:	Temporal profile of the laser pulses.....	26
Fig. 2.8:	Transmission intensity of the Fabry-Perot etalon ($\text{FSR} = 0.5 \text{ cm}^{-1}$) as a function of laser wavelength.....	27
Fig. 2.9:	Part of the circular fringe formed by the diverging laser beam. Separation between two bright fringes is 0.5 cm^{-1}	28
Fig. 3.1:	Single photon absorption and emission in a closed two level system.	33
Fig. 3.2:	Time evolution of the atomic populations in a closed two-level systems under continuous laser excitation for different excitation rates a) $W=1/\tau$, b) $W=10/\tau$	34
Fig. 3.3:	Probability of atoms in a closed two level system as a function of the photon fluence at the end of a laser pulse. Laser pulse width ($\Delta\tau$) have been taken as one tenth of the upper level lifetime (τ).	35
Fig. 3.4:	Saturation curves for different transitions with same cross section values but different branching ratios and radiative lifetimes in a two level system.	37

Fig. 3.5:	Saturation curves of different transitions with different cross section values in a two-level system	37
Fig. 3.6	Single step photoionization of excited atom via autoionizing (AI) level. Atom excited to an autoionizing level spontaneously decays to a free electron and an ion.	39
Fig. 3.7:	Typical three step photoionization pathways.....	40
Fig. 3.8:	Temporal profile of the laser pulses under a) delayed and b) synchronous condition.	43
Fig. 3.9:	Time evolution of atomic population in various levels for a) temporally separated laser pulses and b) temporally synchronous laser pulses.....	43
Fig. 3.10:	Photoionization efficiency as a function of a) first, b) second and c) third laser photon fluences for temporally separated laser pulses.	45
Fig. 3.11:	Photoionization efficiency as a function of a) first, b) second and c) third laser photon fluences for synchronous laser pulses.	45
Fig. 3.12:	a) Magnetic sublevel photoionization pathways for linearly polarized light. b) Relative transition strength between magnetic sublevels for linearly polarized light.	47
Fig. 3.13:	Photoionization yield as a function of second step laser photon fluence for unpolarized and linearly polarized lasers when laser pulses are temporally separated.	48
Fig. 3.14	Dependence of photoionization yield as a function of laser photon fluences in units of saturation photon fluence for J-sequences of a) $6 \rightarrow 6 \rightarrow 6$ and b) $6 \rightarrow 7 \rightarrow 8 \rightarrow 9$. Here, photon fluences of all the lasers are varied simultaneously.	50
Fig. 4.1:	Typical three-step photoionization pathway for atomic uranium using visible lasers.....	52
Fig. 4.2:	Schematic of experimental set up.	57
Fig. 4.3:	Population decay curve of uranium atomic level at $15,631.85 \text{ cm}^{-1}$. The solid line is an exponential fit of the data. Inset: Schematic of excitation pathways for lifetime measurements.	59
Fig. 4.4:	Energy level diagram of the transitions whose branching ratios have been measured.....	61
Fig. 4.5:	a) Schematic of excitation pathways for the pump and probe lasers to measure the branching ratios. The pump laser λ_{pump} pulse excites the	

	population from level 1 to level 2 of the transition whose branching ratio is to be determined and the laser pulses λ_{1P} plus 2 λ_{2P} generate probe signal. b) Representative probe signal versus time delay between the pump and the probe laser pulses.	62
Fig. 4.6:	Repopulation curves of ground level or metastable level at 620.3 cm^{-1} from the excited levels of the respective first step transitions of uranium. Solid line is a fit of the data using equation (4.5) for simultaneous measurement of β and τ	64
Fig. 5.1:	Three-color three-step photoionization pathways: a) without two-color three-photon photoionization, b) with two-color three-photon photoionization. AI level: autoionizing level.....	71
Fig. 5.2:	Photoionization pathways for measurement of cross section of $0 \rightarrow 16,900.38 \text{ cm}^{-1}$ transition of atomic uranium.....	73
Fig. 5.3:	Photoionization yield as a function of the first step laser photon fluence for $0 - 16,900.38 \text{ cm}^{-1}$ transition of atomic uranium.	74
Fig. 5.4:	Photoionization pathways for measurement of photoionization cross sections of excited levels	76
Fig. 5.5:	Dependence of delayed three-color photoionization signal intensity on the third-step laser photon fluence for $34,675.91 - 52,371.6 \text{ cm}^{-1}$ transition at $\lambda_3=564.95 \text{ nm}$. The third-step laser energy at the maximum of photon fluence $4.5 \times 10^{16} \text{ photon/cm}^2$, is 16 mJ/cm^2 . The solid line represents the least square fit of the equation 5.3.	77
Fig. 5.6:	Schematic diagram of a three-step photoionization with various excitation and decay processes.	80
Fig. 5.7:	Theoretical dependence of (a) two-color and (b) delayed three-color three-photon photoionization (PI) efficiency on the second-step laser photon fluence for different values of photoionization cross-section (σ_{2i}) at λ_2 , while keeping other parameters constant.....	82
Fig. 5.8:	Typical time-resolved time-of-flight spectrum of two-color and delayed three-color photoionization of uranium produced via three-step photoionization scheme $620.32 \text{ cm}^{-1} \rightarrow 17,361.89 \text{ cm}^{-1} \rightarrow 34,994.99 \text{ cm}^{-1} \rightarrow 52,558.9 \text{ cm}^{-1}$ by fixing the first-, second- and third-step laser wavelengths at 597.15 nm , 566.96 nm and 569.19 nm corresponding to the respective transitions.....	83

Fig. 5.9:	Dependence of two-color and delayed three-color photoionization efficiency on the second-step laser photon fluence for a chosen transition $17,361.89 \text{ cm}^{-1} \rightarrow 34,994.99 \text{ cm}^{-1}$ at $\lambda_2=566.96 \text{ nm}$. The 2 nd step laser energy at the maximum of photon fluence $1.2 \times 10^{15} \text{ photon/cm}^2$, is 0.44 mJ/cm^2 . The solid line represents the calculated photoionization yields.....	85
Fig. 5.10:	Two-color three-photon photoionization spectrum of uranium recorded along with FP etalon fringes for first-step laser wavelength, λ_1 , fixed at 597.15 nm , corresponding to uranium transition $620.32 \rightarrow 17361.89 \text{ cm}^{-1}$ and second-step laser wavelength, λ_2 , scanned from 565.2 to 567.3 nm	87
Fig. 5.11:	a) Three-color photoionization spectrum of uranium obtained by fixing first- and second-step lasers wavelengths at 597.15 and 566.22 nm corresponding to the respective transitions $620.32 \rightarrow 17361.89 \text{ cm}^{-1}$ and $17361.89 \text{ cm}^{-1} \rightarrow 35018.01 \text{ cm}^{-1}$ and scanning the third laser wavelength, λ_3 , from 565.57 nm to 567.9 nm . b) repeat of (a) with second laser blocked.	88
Fig. 5.12:	Repeat of Fig. 5.9 at higher photon fluence to verify depletion of population of the second-excited level through two-color three-photon photoionization process as shown in Fig. 5.7b. The pulsed energy of the 2 nd laser at the maximum of photon fluence is 13.64 mJ/cm^2 . The solid line represents the calculated photoionization yields.....	89
Fig. 6.1:	Schematics of the experimental set-up. Inset: arrangement for combining laser beams for polarization experiments.	98
Fig. 6.2:	Three-step three-color photoionization pathways of various magnetic sublevels of atomic uranium.	101
Fig. 6.3:	Ionization yield pattern of photoionization schemes $6 \rightarrow 6 \rightarrow 7 \rightarrow (6, 7, 8)$ for different excitation rates (W). In these calculations, excitation rates for all the three-steps are considered equal, i.e. $W_1 = W_2 = W_3 = W$. $\Delta\tau$ is the temporal width of the laser pulse. Polarization combinations 1 to 6 denote $\pi\pi\pi$, $\Pi\pi\pi$, $\pi\pi\Pi$, RRR , $R\pi L$, $\pi\pi L$, respectively; where π , Π , R , L represents state of polarization such as vertical linear, horizontal linear, right circular and left circular, respectively.	103
Fig. 6.4:	Schematic of the three-step excitation schemes used for observing the autoionizing states of atomic uranium.	105

Fig. 6.5:	Photoionization spectrum of uranium from 34,659.18 cm ⁻¹ level. Dense levels structure near 50,200 cm ⁻¹ is the Rydberg series converging to the second ionizing limit. To avoid complexity, the energy values and their J-values are shown only for few strong AI resonances.....	106
Fig. 6.6	Theoretical and experimental yield pattern for a photoionization scheme 6 → 6 → 7 → (6,7,8). In this scheme, the first and the second excited levels considered are 17,361.89 cm ⁻¹ and 34,659.18 cm ⁻¹ , respectively. Polarization combinations 1 to 6 denote πππ, Πππ, ππΠ, RRR, RπL, ππL, respectively; where π, Π, R, L represents state of polarization such as vertical linear, horizontal linear, right circular and left circular, respectively. Blue line represents experimentally measured yield patterns. Measured J-values for 50,331.9 cm ⁻¹ , 50,301.2 cm ⁻¹ and 50,197.17 cm ⁻¹ are 8, 6 and 7, respectively.	120
Fig. 6.7:	Autoionizing Rydberg series observed from 34659.18 cm ⁻¹ level.	122
Fig. 6.8:	Plot of quantum defect ($\delta = n - n^*$) versus principal quantum number (n) for various assumed second ionization limits for the AI Rydberg series of Table 3. The nearest integer corresponding to the calculated effective quantum number (n*) has been assumed as principal quantum number.	123
Fig. 7.1:	HCDT used in the present experiments.	128
Fig. 7.2:	Schematic of HCDT and electrical circuit diagram.	128
Fig. 7.3:	a) Cross sectional view of the hollow cathode discharge, b) The electric field (E) distribution in the CDS. Maximum electric field at the cathode (x = 0) is -2V ₀ /d. V ₀ is the voltage across the discharge, c) Laser induced photoionization in cathode dark space (CDS).	128
Fig. 7.4 :	Typical temporal wave forms of a) normal OG signal, b) OG signal in presence of two-color three-photon photoionization, c)Two-color (2C) PIOG signal when the oscilloscope scale was stretched from μs to ns, and d) two-color and delayed three-color PIOG signal.	130
Fig. 7.5:	a) Temporal profile of the PIOG and OG signal for focused laser beam, b) Radial profile of PIOG signal across the cylindrical cathode.	132
Fig. 7.6:	a) A part of a three-color three-photon photoionization spectra of uranium recorded using scheme A in the energy region 52,148–52,216 cm ⁻¹ . Third dye laser per pulse energy was ~200μJ. 1C: Single-color; 2C:	

	Two-color; 3C: three-color. b) Repeat of (a) with second dye laser (λ_2) blocked.....	135
Fig. 7.7:	a & b) Repeat of Fig. 7.6 a & b with third-step dye laser per pulse energy of $\sim 3\text{mJ}$, and c) Single-color three photon photoionization spectra of uranium recorded by blocking first and second lasers (λ_1 & λ_2).	135
Fig. 7.8:	A portion of the two color photoionization spectra for various λ_1 detuning (a) $+0.5\text{ cm}^{-1}$, b) $+0.28\text{ cm}^{-1}$, c) $+0.20\text{ cm}^{-1}$ and d) $+0.00\text{ cm}^{-1}$ from exact resonance of ^{238}U ($0 - 17369.54\text{ cm}^{-1}$). e) single color spectrum, f) Fabry Perot etalon fringes($\text{FSR}=0.5\text{ cm}^{-1}$).	139
Fig. 7.9:	Comparative studies of variation of photoionization signal as a function of particular laser photon fluence in HCDT using PIOG spectroscopy (a, b and c) and in TOF-MS (d, e and f) for first, second and third step respectively. Here, σ_1 and σ_2 represents the first and second step photoexcitation cross section. Also σ_3 represents the third step/photoionization cross section.	142

List of Tables

Table 4.1:	Measured values of radiative lifetime of even-parity excited levels of uranium.....	60
Table 4.2:	Measured values of branching ratio and gA values of uranium.....	66
Table 5.1:	Photoexcitation cross sections (σ_1) and transition probability (A) of $0 \rightarrow 16,900.38 \text{ cm}^{-1}$ transition of atomic uranium for 2.4 GHz laser line width.	75
Table 5.2:	Photoionization cross-sections (σ_i) of odd-parity high-lying levels of atomic uranium.	78
Table 5.3:	Radiative lifetimes of odd-parity excited levels of uranium.....	86
Table 5.4:	Measured values of excited-level-to-excited-level photoexcitation (σ_2) and photoionization (σ_{2i}) cross-sections for a given laser line width of 2.4 GHz.	86
Table 6.1:	Second excited levels used for the survey.	108
Table 6.2:	Energies and J-values of autoionizing levels of uranium	109
Table 6.3:	Autoionizing Rydberg levels of uranium. ‘n’ represents nearest integer corresponding to the calculated effective quantum number (n^*). $\delta = n - n^*$, represents the quantum defect.	124

Chapter 1 - INTRODUCTION

1.1 Introduction to spectroscopy

Spectroscopy is the study of interaction of electromagnetic radiation with matter, which leads to either absorption, emission, scattering of radiation or ionization of the matter. Spectroscopic study is often characterized by the functional dependence of intensity of radiation emitted, absorbed or photoion produced on the wavelength or frequency of radiation. Frequency, intensity and spectral width of a spectrum can provide a wealth of qualitative and quantitative information about the matter. In basic spectroscopy, the frequency of the spectral line reveals the energy level details of atoms and molecules, while its intensity provides information about the transition probability i.e. strength of coupling between the two energy levels. The width of the spectral lines, on the other hand, unfolds information about the collision processes, the inter-atomic potentials as well as the velocity distribution of the emitting or absorbing species. It may be of interest to note here that spectroscopic studies of the structure of atoms and molecules have contributed significantly to the development of quantum mechanics. As a matter of fact, spectroscopy has made considerable impact in many areas of science including laser physics, analytical chemistry, environmental science, medicine, astrophysics etc. In astrophysics, spectroscopic analysis of radiation emitted from the sun, the interstellar space and distant stars, etc. can provide invaluable information about their chemical composition, mass, density, distance, etc.

Spectroscopy has also been known to be playing a vital role in unraveling information on various atomic properties to gain an insight into the atomic structures [1-4]. Atomic parameters such as energy level values, total angular momenta, radiative lifetimes, branching ratios, transition probabilities, and photoionization cross sections etc. are fundamental characteristics of an atomic system. Accurate information of these parameters is a

prerequisite to get deeper insight into basic atomic physics as well as to develop novel photoionization pathways in applied spectroscopy [4]. In particular, information on energy level values, transition wavelengths, transition probabilities etc. are useful to understand the structure of atom using adequate theories or models. In addition, transition probabilities play a key role in many areas of science such as, laser physics - to identify new laser materials, in astrophysics - to determine the abundance of elements in the solar system and in laser based applications like trace analysis of radioactive elements/isotopes or in laser isotope separation etc. Isotope shift and hyperfine structure can provide information about nuclear size, shape, magnetic dipole and electric quadrupole moments etc. These parameters are known to play a decisive role in isotope selective photoionization processes. In addition, information on photoexcitation and photoionization cross sections is important for quantifying the photoionization process. For an atomic system with single valence electron, these atomic parameters can be calculated accurately using theoretical models. However, for a multi-electron atomic system theoretical determination of these parameters with desired accuracy pose serious problem. To this end various spectroscopic techniques, have proved to be most useful towards experimental determination of atomic parameters in case of multiple valence electron.

1.2 Spectroscopic techniques

Traditionally, absorption and emission spectroscopic techniques have been used for studying atomic spectra [1,5,6]. Emission spectra obtained from conventional atomic sources like arc, hollow cathode and electrode-less discharges are analyzed using either high-resolution grating spectrometer or Fourier transform spectrometer. Spectroscopic investigations utilizing these sources put stringent requirement on the resolution of the spectrometer as these sources have atoms, ions and multi-atomic species under varying level

of excitation resulting in complicated emission spectra. Despite these difficulties, a large number of atomic data have been generated using conventional spectroscopic techniques. However, emission spectroscopic techniques have limitations in studying high-lying excited levels of atoms that intrinsically contain less number of atoms. Absorption (single-photon) spectroscopic technique using white light source for studying high-lying atomic levels is not suitable either due to the following reasons: 1) spectral intensity of the white light source is very low, 2) absorption cross section decreases as transition frequency increases, 3) inaccessibility of an excited level with the same parity as that of the ground level. Laser based spectroscopy techniques have proved to be the most versatile method for obtaining detailed spectroscopic information in these cases.

1.2.1 Spectroscopic techniques with tunable lasers

The invention and subsequent development of narrowband, tunable and intense laser has revolutionized the field of spectroscopy and has led to the emergence of a number of new spectroscopic techniques over the years. The usage of lasers has not only simplified the spectra to be studied but also made those experiments possible, which were not possible with conventional sources, either due to the lack of intensity or insufficient resolution. When laser frequency is in resonance with the atomic transition frequency, photon emanated by the laser is absorbed and atom gets excited in turn into the higher energy level. Absorption of photons by atoms can lead to change of intensity of transmitted light, change of discharge impedance, emission of light and generation of photoions etc., which are characteristics of the energy levels of the atomic species. Owing to higher spectral intensity of the laser compared to that of the white-light source, it is possible to saturate the atomic transition and transfer a significant fraction of ground level atomic population to the excited level, thus making the detection easier.

In order to perform laser spectroscopy of atoms, one generally requires an atomic vapor source, tunable lasers and a detector [3]. There are various kinds of atomic vapor sources such as hollow cathode discharge, electrodeless discharge, arc, heat-pipe oven, inductively heated oven, electron beam heated oven, laser ablation source, ionic sputtering source, etc. for carrying out atomic spectroscopy. Among all these vapor sources, resistively heated effusive type atomic beam source offers the cleanest environment for spectroscopic studies. There are various types of tunable laser sources such as dye laser, Ti:Sapphire laser, diode laser etc. which have been used for laser spectroscopy. Based on the operation, tunable lasers can be classified into continuous wave (CW) and pulsed types. Choice of the laser is decided by the spectral linewidth, intensity and nature of the investigations. Typical spectral line widths and temporal width of commercially available pulsed dye lasers lie typically within 1 - 10 GHz and 4 -50 ns, respectively. Pulsed lasers that intrinsically have higher intensity are preferred over CW lasers to saturate the atomic transition and are essential in photoionization processes where high photoionization efficiency is required. For high-resolution spectroscopic studies, CW lasers are, however, preferred over pulsed laser as they intrinsically possess very narrow linewidths (< 1 MHz).

In laser spectroscopy, the line width of a resonance depends on both the laser line width and the atomic absorption line width. Atomic absorption line width, in turn, depends on various types of line broadening mechanisms [3] such as natural broadening due to finite lifetimes of the energy levels, collisional broadening due to various types of collisions, Doppler broadening due to velocity distribution of atoms and power broadening due to Rabi oscillations of atom between two levels at high laser powers, etc. In case of monochromatic excitation, overall line width of the resonance is governed primarily by the atomic absorption linewidth which is mostly Doppler limited. However, to observe naturally broadened spectral line in presence of large Doppler background, various types of high-resolution spectroscopic

techniques such as saturation absorption spectroscopy, inter-modulated optogalvanic/fluorescence spectroscopy, Doppler free two-photon absorption spectroscopy, and polarization spectroscopy has been developed using narrowband CW lasers [3]. In case of excitation by a multimode-pulsed laser, overall line width of a resonance is governed by the convolution of the atomic absorption linewidth and the laser line width.

Laser spectroscopic techniques such as absorption, optogalvanic, fluorescence, photoionization etc. are different variants of absorption spectroscopy that vary only in detection mechanism of the absorbed photon. The details of various types of laser spectroscopic techniques are given below.

1.2.1 a) Absorption spectroscopy

In this technique, absorption of photon is monitored by measuring relative intensities of the incident (I_0) and transmitted (I_T) radiation. For small absorption, the relation between I_0 and I_T according to the Beer-Lambert law [3] is expressed as

$$I_T(\omega) = I_0(\omega)e^{-n\sigma(\omega)l}$$

Where n is the number density, l is the path length and $\sigma(\omega)$ is the frequency dependent photo-absorption cross section. In order to reach very high detection sensitivity of absorption, the product of path length and absorption cross section should be large. To measure small absorption in presence of a large background, high signal to noise ratio is often realized by using phase sensitive detection. To achieve large path length, atomic vapor sample is placed inside a laser cavity (intra cavity absorption [3]) or inside a highly reflective external cavity (cavity ring down spectroscopy [3]). For refractory elements where generation of atomic vapor with sufficient number density is difficult, the conventional absorption spectroscopy is not usually applicable.

1.2.1 b) Optogalvanic spectroscopy

Optogalvanic spectroscopy is an excellent and simple technique to perform laser spectroscopy of atoms and molecules in the discharge environments [7]. This technique is based on the optogalvanic effect i.e. change of electrical properties of the discharge due to absorption of light. When molecules, atoms or ions in a discharge absorb light, the population distribution between the two levels changes due to optical pumping. The perturbation in the population distribution leads to change in the impedance of the discharge either due to difference in ionization probability of the two levels involved in the process or due to the change in electronic mobility via super elastic collision with excited atoms. The change in discharge tube impedance leads to corresponding variation in the discharge current, which is detected as a change in voltage across the discharge impedance or ballast resistor. This technique has been extensively used for studying high-lying energy levels of noble gas atoms [7-9]. Excitation of noble gas is very difficult due to non-availability of suitable lasers for first step excitation whose wavelength lie in the vacuum ultraviolet region. In contrast, using hollow cathode discharges, the metastable states of noble gases can be easily populated through electron impact excitation. This technique has also been proved to be useful for studying refractory elements, which have low vapor pressure at room temperature. This technique has been used extensively for spectroscopic investigations of various refractive elements [10-14].

In both absorption and optogalvanic spectroscopy techniques, the effect of absorption of photons is observed only when a large number of atoms participate in the absorption process. For very sensitive detection of atom, laser induced fluorescence or photoionization technique is often used, that has been reported to have the capability of detecting a single atom [15,16].

1.2.1 c) Laser induced Fluorescence spectroscopy

In this technique, atoms are promoted to excited level by absorbing UV or visible light photons. The excited level has finite lifetime and it eventually decays to various low-lying energy levels by way of emitting photons, which is known as fluorescence. Absorption of laser photons is monitored by monitoring laser induced fluorescence (LIF) that can be detected by using a photomultiplier tube (PMT). Unlike absorption spectroscopy, where the absorption is measured over a large background light, the fluorescence can be detected at very small background noise by selecting a wavelength different from that of the pump laser, which results in high detection sensitivity [3]. LIF has been used extensively for studying bound energy levels of many elements [17-20]]. Fast detection of LIF has facilitated accurate measurement of radiative lifetimes of atoms and molecules [17,21]. Detection of dispersed LIF has enabled to measure the branching ratio of a transition [22]. However, LIF is not suitable for studying the Rydberg levels because of their large radiative lifetimes resulting in a small fluorescence yield. LIF is also not useful for the study of autoionizing levels, the discrete levels above the first ionization limit of atom, as these levels decay instantaneously into an electron-ion pair.

1.2.1 d) Resonance Ionization Spectroscopy

Resonance ionization spectroscopy is a technique where the absorption of laser photons is monitored by detecting the photo ions. Here, the atoms are excited in a stepwise manner by resonant lasers before its ionization eventually [15,23,24-26]. Resonance ionization spectroscopy (RIS), owing to its high sensitivity and selectivity, has emerged as an excellent tool to study the complex electronic structure of atoms and molecules. Multistep RIS, in particular, has played an important role in the measurement of atomic parameters; especially in the high energy regions where the conventional and other laser based spectroscopic techniques have limitations. RIS has been extensively used to study the high-

lying atomic levels near and above the first ionization limit. RIS has found wide application in the accurate determination of ionization potentials of most of the elements in the periodic table through the observation of Rydberg series [27,28,29,30-33]. RIS has also found application in measuring photoionization cross section in the excited levels of many elements of the periodic table [34-46]. Due to its high sensitivity and selectivity, RIS is widely used to extract the nuclear information (nuclear spin, shape and size of the nucleus) of short lived nuclei by measuring isotope shift and hyperfine structure in online rare isotope facilities [47-49]. The combination of RIS with mass spectrometry (MS) has given birth to an even more powerful technique, known as Resonance Ionization Mass Spectrometry (RIMS). This technique offers mass selectivity in addition to the spectral selectivity achievable with RIS. RIMS can be used to detect isotopes/elements, with minimum isotopic/isobaric interferences [50-56]. Due to high sensitivity and selectivity of RIS, isotope selective RIS has been used for separation of isotopes of a variety of elements [57-62] that have applications both in nuclear industry and in nuclear medicine.

Number of lasers and excitation steps required basically depend on the ionization potential and energy level structure of the atoms and the laser frequency [15]. Fig. 1.1 shows various possible photoionization pathways of elements using visible and UV lasers. Here, laser frequencies are tuned in resonance to the transition frequencies of a photo ionization scheme of the desired element or isotopes, which causes selective ionization of the targeted atoms/isotopes. Among the different photoionization schemes, simplest type of scheme is single-color multi-photon photoionization scheme; here laser frequency is in resonance or near resonance with at least one of the transitions of the atoms [63-67]. Although this is not

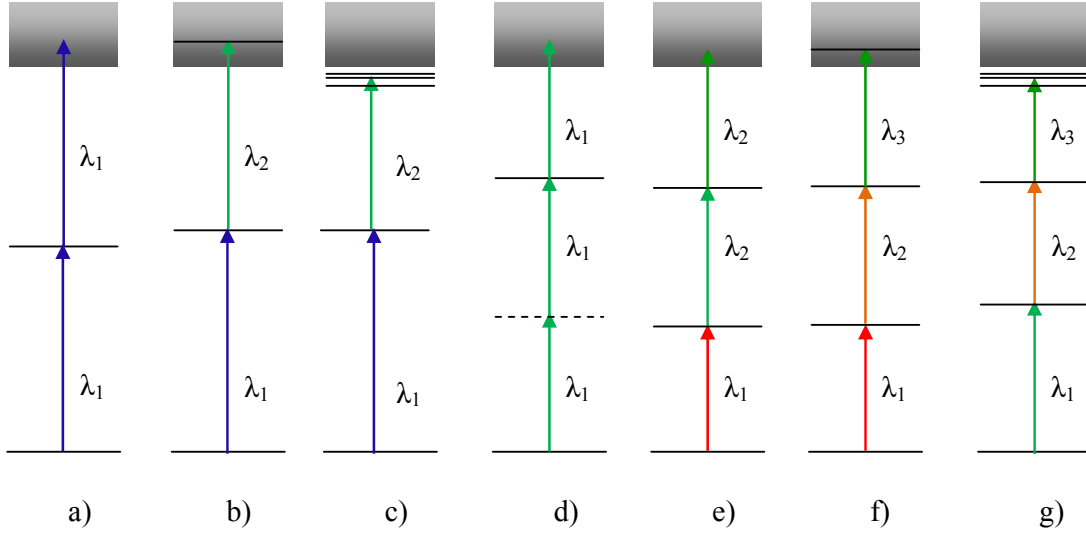


Fig. 1.1: Different types of photoionization pathways of atoms: a) single-color two-photon, b) two-color two-photon via autoionizing level, c) two-color two-photon via Rydberg level, d) near resonant single-color three-photon, e) two-color three-photon, f) three-color three-photon via autoionizing level, g) three-color three-photon via Rydberg level. Ionization of Rydberg level is done by using external electric field, inexpensive laser photons or through atom-atom collisions.

an efficient pathway for photoionization but it is a useful method when only elemental selectivity is required. Isotope selective excitation often demands two- or three-color multistep photoionization pathways. The efficiency of the ionization schemes depends mainly on the choice of final step transition, as intermediated transitions could be easily saturated due to their high excitation cross sections compared to that of the final step transitions. Choice of a final step transition can lead to ionization in continuum or excitation into Rydberg levels or autoionizing levels [26]. Rydberg and autoionizing levels are preferred over transitions into the continuum as their cross sections can easily exceed that of the latter by two to four orders of magnitude [27,68]. Rydberg levels are ionized using delayed pulsed electric field whereas autoionizing levels ionize spontaneously. Ionization of Rydberg level can also be achieved with infrared laser photons or through collisions with inert gas. It may be noted that while in case of excitation into Rydberg levels and ionization by delayed electric fields, only a fraction of the ground level population available in the Rydberg level

can be ionized, usage of autoionizing levels on the other hand results in almost 100% ionization of the ground level population [15,69]. This aspect has been discussed in sections 3.2.3.2 and 3.2.3.3 of chapter 3. Alkali atoms with single valence electron do not possess autoionizing levels near first ionization limit, thus efficient ionization of these atoms is only possible through Rydberg levels.

1.3 Atomic uranium and its spectroscopic importance

Uranium is the heaviest naturally occurring element ($Z = 92$) and is the fourth in the actinide series of the periodic table. This element is radioactive and has three naturally available isotopes, ^{238}U , ^{235}U and ^{234}U with abundances 99.278%, 0.72% and 0.0054%, respectively. Over the last many decades, the atomic spectroscopy of uranium has been investigated for a variety of reasons. The major interest of spectroscopic investigations of atomic uranium stems from its applications in nuclear technology. ^{235}U is the only naturally occurring fissile isotope and is a natural fuel for nuclear power plants. However, natural uranium has only 0.72 % of ^{235}U , its enrichment is prerequisite to sustain criticality of light water reactors. ^{238}U is fertile but it can be transmuted to fissile ^{239}Pu in a nuclear reactor, which can be used as a nuclear fuel in the fast breeder reactor. Another fissile isotope of uranium, which is equally important in nuclear technology, is ^{233}U . Since ^{233}U has no natural abundance, it is produced through transmutation of natural thorium. Measurement of isotope ratio of $^{235}\text{U}/^{238}\text{U}$ is important to differentiate natural and processed uranium in the nuclear reactor. Ultra trace detection of radioactive isotopes ^{236}U is important to know irradiation of natural uranium and migration of reactor irradiated uranium during nuclear accident [71]. The transitions of uranium measured accurately using Fourier transform spectroscopy are routinely used as wavelength references throughout the UV to near-IR spectral range [5,72,73].

1.4: A literature review on the spectroscopy of uranium and scope of the present work

Due to the presence of six optically active electrons in the outer shell of uranium atom accurate theoretical determination of its atomic parameters is an uphill task [74]. Information about the atomic parameters has been generated usually through experiments. Kiess et. al.[75] are credited with the first spectroscopic investigation of atomic uranium. They have reported 18 levels of the 2 low odd configurations f^3ds^2 and f^3d^2s and 280 even levels in uranium arc emission by studying Zeeman Effect. Development of high-resolution grating, Fourier transform spectroscopy technique, liquid nitrogen cooled hollow cathode discharge tube and electrode less discharge have led to the measurement of a large number of atomic data up to $40,000\text{ cm}^{-1}$ (mostly in the low-lying energy region). Blaise et al. [74] have reported 1,240 even levels between $7,020$ to $42,000\text{ cm}^{-1}$ and 360 odd levels up to $38,000\text{ cm}^{-1}$ by analyzing 92,000 emission lines. They have also reported electronic configurations wherever possible, J-values, isotope shifts, Lande g-factors etc. Palmer et al. [5] have reported an ATLAS of atomic uranium containing 4,928 emission spectral lines obtained from a U-Ne hollow cathode discharge tube. Parallel to these experimental studies, ab initio calculations based on Hartee-Fock method were carried out to calculate energy values, isotope shifts, hyperfine structure of pure configurations [76-78]. These calculations were used to analyze the large number of data obtained from emission spectra. Also, configurations of energy levels were assigned based on the measured energy level values, isotope shifts and hyperfine structures. However, assignment of configuration of the levels above $20,000\text{ cm}^{-1}$ was found to be very difficult due to configuration mixing [74].

The development of narrow linewidth tunable dye lasers has led to a multitude of studies using stepwise excitation and ionization to detect high-lying energy levels below and

above the first ionization potential. These studies formed a major precursor for both laser isotope separation and trace detection of atomic uranium. Two-step selective photoionization of ^{235}U , using CW dye laser and mercury arc lamp, was first demonstrated by Tuccio et al.[79]. Janes et al. [80] have performed detailed spectroscopic studies relevant to laser isotope separation of atomic uranium using two pulsed, tunable dye lasers. They have reported the measurements of the ionization potential, photoionization cross section of excited levels and radiative lifetimes of many even-parity levels of atomic uranium. Carlson et al. [81] have investigated in the energy region $32,600\text{-}34,200\text{ cm}^{-1}$ of uranium using three-color three-photon photoionization spectroscopy and reported more than 100 new high-lying odd levels, possible J-values. They have also measured radiative lifetimes, branching ratios and transition probabilities using delayed photoionization method [81, 82]. Solarz et al. [27] have determined the first ionization potential of uranium by observing Rydberg progressions of atomic uranium within $1,000\text{ cm}^{-1}$ below the first ionization limit using three dye lasers and an appropriately delayed pulsed carbon dioxide laser. Miron et al. [17] have investigated odd-parity high lying levels in the energy region $32,260\text{-}34,900\text{ cm}^{-1}$ and $49,500\text{--}49,900\text{ cm}^{-1}$ using stepwise excitation and fluorescence detection. They have reported large number of new energy levels along with their J-values and radiative lifetimes. Coste et al.[28] have measured both the first and the second ionization limit accurately by observing bound and autoionizing Rydberg series. Donohue et al. [63] have investigated high-lying energy levels of various actinide elements including uranium using single-color three-photon photoionization spectroscopy. Mago et al. [64] have identified some of the high-lying levels of uranium using single-color three-photon photoionization spectroscopy. Using two-color three-photon photoionization spectroscopy, many new odd-parity high-lying levels of atomic uranium were identified [83-89]. Mago et al.[84,87] have investigated odd-parity high-lying levels of atomic uranium in the energy region $34,000\text{-}37,000\text{ cm}^{-1}$ and $39,900\text{-}41,600\text{ cm}^{-1}$

and identified more than 300 odd levels and assigned unique J-value to many of the levels. Suri et al. [85] have studied in the energy region $34,290\text{--}35,120\text{ cm}^{-1}$ and reduced the ambiguity in the assignment of J-value to many of the levels. Bajaj et al.[86] have reported more than hundred new energy levels in the energy region $37,540\text{--}38,420\text{ cm}^{-1}$. Smyth et al. [90] have investigated odd-parity high lying levels in the energy region $38,500\text{--}41,200\text{ cm}^{-1}$ using stepwise excitation in conjunction with fluorescence detection. Shi et al.[88] have focused their study in the energy region $35,678\text{--}36,696\text{ cm}^{-1}$ and identified 112 new odd levels. Miyabe et al.[83] have studied systematically in the energy region $31,300\text{--}36,400\text{ cm}^{-1}$ using two-color and three-color three-step photoionization spectroscopy and observed more than 450 odd-parity levels including about 150 new levels. They have also assigned J-values to a large number of levels based on J-momentum selection rule. Isotope shifts of a large number of odd-parity high-lying levels have been reported using resonance ionization spectroscopy [91]. Levesque et al. [92] have predicted large number of high-lying levels of atomic uranium using single-color photoionization optogalvanic (PIOG) spectroscopy. Vas Dev et al. [93] have studied high-lying odd parity levels of atomic uranium in the energy region $34,500 - 34,813\text{ cm}^{-1}$ in U-Ne hollow cathode discharge using two-color three-photon PLOG spectroscopy and confirmed all the levels previously observed in this energy region. Using three-color three-step photoionization spectroscopy, Raeder et al. [89] have reported 86 odd-parity levels in the energy region $37,200 - 38,650\text{ cm}^{-1}$. Thus the information of energy levels in the energy region $32,000 - 38,000$ is mostly available in the literature. However the data on the radiative lifetimes and isotope shifts are still lacking. Using three-step photoionization spectroscopy large numbers of odd-parity autoionizing levels were identified [71,94-99]. Despite this voluminous work, the information on autoionizing levels of uranium available in the literature is scanty. This has formed the basis of chapter 6 and 7. Similarly, information on the hyperfine structure of high-lying levels is rarely available [100-

102] in the literature. Using multi-mode pulsed laser, hyperfine structure of the energy levels cannot be resolved and hence has not been studied in the present work. With the exception of a few [45,52,80,103,104], transition probabilities/cross sections of the second and third step transitions are not available in the literature. Thus, the primary interest of this dissertation work on uranium has been to measure various atomic parameters, which may prove to be useful in constructing efficient photoionization schemes and, in turn, the quantification of the photoionization yield.

This thesis focuses on the measurements of various spectroscopic parameters such as radiative lifetimes, branching ratios, transition probabilities, photoexcitation/photoionization cross sections, energy values, total angular momenta, isotope shifts of atomic uranium by resonance ionization spectroscopy. The measurements of atomic parameters have been carried out in an uranium atomic beam coupled with a time-of-flight mass spectrometer (TOF-MS) using Q-switched Nd:YAG pumped dye lasers. As an alternate to the elaborate experimental setup consisting of an atomic beam source and a TOF-MS, the photoionization spectroscopy of uranium has also been carried out in a U-Ne hollow cathode discharge tube (HCDT), a simpler device, where HCDT is used as a source of spectroscopic grade atomic vapors as well as photoion/photoelectron detector. In this case, since the photoionization is detected as a variation in the discharge current, the technique is known as photoionization optogalvanic (PIOG) spectroscopy. PLOG is basically a resonance ionization spectroscopy which is carried out in the cathode dark space of the HCD where electric field gradient assists to collect photoions.

1.5 Organization of the thesis

The present thesis is organized into eight chapters including the introductory chapter denoted as chapter 1. Chapter 2 describes the experimental set-up in details. Chapter 3 is

devoted to numerical study of excitation dynamics in a three-step photoionization of atomic uranium. These numerical studies are prerequisite to analyze the experimental data presented in chapters 5 and 6.

Chapter 4 deals with the measurement of radiative lifetimes, branching ratios, and absolute transition probabilities of atomic uranium using delayed photoionization method. Using this method, radiative lifetimes of ten even-parity energy levels of atomic uranium in the 15,500-19,000 cm^{-1} region and branching ratios of six transitions, starting either from ground state ($^5L^o_6$) or from metastable state ($^5K^o_5$) at 620.32 cm^{-1} are measured. By combining the measured values of radiative lifetimes (τ) and branching ratios (β), the absolute transition probabilities (A) of six transitions have been determined using the expression $A=\beta/\tau$.

Chapter 5 presents the measurements of excited-level-to-excited-level transition probabilities and photoionization cross sections of atomic uranium using saturation method. Using this method photoionization cross sections of eleven strong autoionizing resonances from different excited levels have been measured. Photoexcitation dynamics in a three-step photoionization of atomic uranium is investigated using time-resolved two-color three-photon and delayed three-color three-photon photoionization signals. Dependence of both the signals on the second-step laser photon fluence is studied. The effect of photoionization cross-section (σ_{2i}) from second excited level at second step wavelength on the saturation curve of the second step transition is discussed. Excited-level-to-excited-level photoexcitation and photoionization cross-section from the second-excited level are simultaneously determined by analyzing the two-color three-photon and three-color three-photon photoionization signals using population rate equation model. Using this methodology, photoexcitation and photoionization cross-sections at seven values of second-step laser wavelength have been measured. From the measured values of the photoexcitation cross-sections, the excited-level-

to-excited-level transition probabilities are obtained and compared these with the values reported in the literature. Details of these investigations together with numerical calculations of photoexcitation dynamics are presented in this chapter.

In chapter 6, an exhaustive study of autoionizing levels of atomic uranium in the energy region up to $1,550\text{ cm}^{-1}$ above the ionization limit from 11 different second excited levels is presented. A detailed analysis of the photoionization spectra has revealed a large number of even-parity autoionizing levels including 199 new levels and a Rydberg series converging to the second lowest ionic level (${}^6\text{L}_{11/2}^{\circ}$) of uranium. By using both angular momentum selection rules and the polarization combination methods, the J-values of large number of autoionizing levels have been assigned unambiguously.

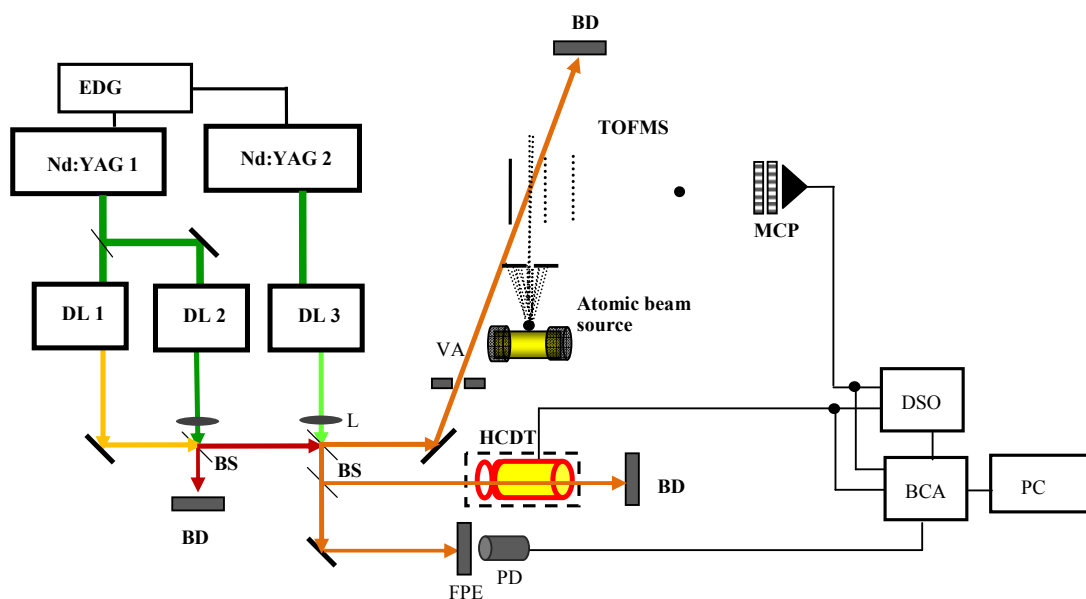
Chapter 7 presents three-color photoionization optogalvanic (PIOG) spectroscopy of uranium in a U-Ne hollow cathode discharge tube. Using PLOG technique, photoionization spectra of uranium have been investigated systematically in the energy region $52,150\text{--}52,590\text{ cm}^{-1}$ i.e. $2,200\text{ cm}^{-1}$ above the first ionization potential, through three different excitation pathways, originating from its ground state, $0\text{ cm}^{-1}({}^5\text{L}_6^{\circ})$. Analysis of the photoionization spectra have resulted in the identification of large number of even-parity autoionizing levels. J-value of a few such levels is assigned unambiguously. Further, the potential of this technique has been explored to measure the isotope shifts of second excited levels and photoexcitation/photoionization cross sections.

Finally, the important conclusions from the present studies and the scope for future work are summarized in Chapter 8.

Chapter 2 - Experimental set-up

2.1 Introduction

In this thesis work, both numerical calculations and experiments were carried out to measure various atomic parameters. The measurements of atomic parameters were performed using resonance ionization mass spectrometry (RIMS) setup consisting of an atomic beam coupled with a time-of-flight mass spectrometer (TOF-MS) and Nd:YAG pumped dye lasers. As an alternate to the bulky and expensive RIMS setup consisting of vacuum chamber, high-temperature oven, detector etc. required for photoionization spectroscopy of refractory elements, the photoionization spectroscopy of uranium has also been carried out in a U-Ne



MO-Master Oscillator, EDG-Electronic delay generator, DL- Dye laser, BS- Beam splitter, L- Beam collimating lens, HCDDT-Hollow cathode discharge tube, BD- Beam dump, BCA- Boxcar averager, PC - Personal computer, TOFMS – Time-of-flight mass spectrometer, DSO- Digital storage oscilloscope, MCP- Micro channel plate detector, VA- variable aperture, FPE- Fabry Perot Etalon and PD- photo diode.

Fig. 2.1: Schematic of experimental set-up.

hollow cathode discharge tube (HCDDT). Schematic of the experimental set-up is shown in Fig.

2.1. The RIMS set up can be divided into four sub systems: a) laser systems consisting of

three pulsed dye lasers pumped by two Nd:YAG lasers at 532 nm, b) an in-house-built time-of-flight mass spectrometer (TOF-MS) and an atomic vapor source consisting of a high temperature oven assembly, c) a U-Ne hollow cathode discharge tube (HCDDT), and d) Signal monitoring and processing devices. The details of the sub-systems and their working principles are discussed in the following sections.

2.2 Laser systems

Laser systems consisted of three pulsed dye lasers (Model No. TDL 90, make: Quantel, France) pumped by second harmonic (532 nm) of two Q-switched Nd:YAG lasers (Model No: YG 981, Quantel, France). The laser systems used in the present work are shown in Fig. 2.2.



Fig. 2.2: *Laser systems used in resonance ionization spectroscopy of atomic uranium.*

Repetition rate and temporal width of the dye lasers were 20 Hz and ~ 5 ns respectively. Spectral width of the dye lasers was about 0.08 cm^{-1} . Typical pulse energies of the pump lasers at 532 nm were in the range of 150 mJ to 350 mJ. Typical pulse energies of the dye lasers were in the range of few mJ to 30 mJ. The desired wavelengths were realized using various dyes (Rhodamine 6G, Rhodamine 610, Rhodamine 640, DCM etc.) dissolved in ethanol solvent. Output of the dye lasers were linearly polarized in the vertical direction (purity >98%). The required temporal delay between the first and the second laser was achieved optically and delay between the second and the third laser was obtained by using an electronic delay generator.

The optical assembly of the Nd:YAG laser used for present work consisted of an oscillator, an amplifier and a second harmonic converter module. Oscillator cavity mainly consisted of a high-reflective mirror, output coupler, laser head (Nd:YAG rod, ellipsoidal pumping chamber and a flash lamp) and an electro optic Q-switch etc. The fundamental wavelength of the Nd:YAG at 1064 nm was amplified and frequency doubled using deuterated potassium dihydrogen phosphate (DKDP) non-linear crystals. The second harmonic of Nd:YAG at 532 nm was used for pumping the dye lasers.

Dye lasers (TDL -90) used in this present work was transversely pumped by second harmonic of Nd:YAG laser in the grazing incidence grating (GIG) geometry. Narrow line width was selected using combination of a grating and a tuning mirror. A fraction of the dispersed light by the grating was reflected back into the cavity by the tuning mirror. Full illumination of the grating was realized by using prism beam expander. Output from the oscillator was amplified by using two-stage amplification (pre-amplifier and amplifier). In these dye lasers, wavelength tuning was performed by means of a rotating mirror placed in front of the grating. A precision sine-bar was used to produce linear relationship between

stepper motor angular motion and selected wavelength. Minimum step size during scanning of the wavelength was 0.25 pm over the entire tuning range.

2.3 Time-of-flight mass spectrometer (TOF-MS)

A TOF-MS is a simple device to observe the entire mass spectrum of a mixture of ions having different mass to charge ratio in a single time frame [105, 106]. The TOF-MS used in the present study is indigenously developed and it can be operated both in linear and reflectron time-of-flight mode. For all the experiments related to this thesis the TOF-MS was operated in linear mode having mass resolution $\left(\frac{\Delta m}{m}\right)$ of about 800 at FWHM with collimated atomic beam. It consisted of an atomic vapor source, ion extraction and acceleration assembly, electric field free drift tube of length 1.3 m and a chevron type micro channel plate (MCP) detector. Turbo molecular pump backed by rotary pump was used to evacuate the entire TOF-MS. The pressure inside the TOF-MS was maintained at 2×10^{-7} mbar during the experiments.

A resistively heated effusive source was coupled with the TOF-MS to generate atomic vapor of uranium. It was made of cylindrical tantalum crucible (diameter 8 mm) with an orifice of diameter 1.5 mm at the middle. This crucible was made of rolled tantalum sheets of thickness 25 micron. Two molybdenum end caps were used to hold the crucible and to flow the high electric current for heating. The sample consisted of about few hundred mg of solid turnings of natural uranium. Typical oven current and operating temperature were about 140 A and 1850 K, respectively. To get a well collimated atomic beam, the atoms effusing out of the vapor source were further apertured (diameter 2 mm) at a distance of 20 mm from the orifice. Reduced Doppler width was estimated to be about 50 MHz. The size of the atomic beam in the interaction region was about 4 mm. Typical atomic number density in the interaction region was estimated to be $\sim 10^7 \text{ cm}^{-3}$. The ion extraction and acceleration

assembly consisted of end plate (repeller plate), extraction and acceleration grids. The TOF-MS used in the present work is shown in Fig. 2.3.



Fig. 2.3: Time-of-flight mass spectrometer used in resonance ionization spectroscopy of atomic uranium.

2.3.1 Working principle

The working principle of linear TOF-MS is described in detail by Wiley-McLaren [107]. Briefly, ions produced through laser atom interaction are extracted, accelerated and introduced into the electric field free drift tube using DC/pulsed electric fields and finally detected by a micro channel plate detector which is placed at the space focused point (Fig.2.4). Ions with same charge state, acquire same kinetic energy ($1/2mv^2$) from the applied potential (V) which is independent of their mass (m). So, the velocity (v) of ions is inversely proportional to the square root of its mass. Thus the ions having smaller mass will reach the detector at an earlier time compared to the heavier ions. The total time (t) taken by the ions to reach the detector can be expressed as

$$t = t_1 + t_2 + t_D$$

where t_1 , t_2 and t_D are the time required by the ions to reach the extraction grid, time spent in the acceleration region and in the drift region, respectively. Since $t_D \gg (t_1 + t_2)$, the above expression can be approximately written as $t \approx t_D$. Since $t \propto \frac{1}{v}$ and $v \propto \frac{1}{\sqrt{m}}$, so the

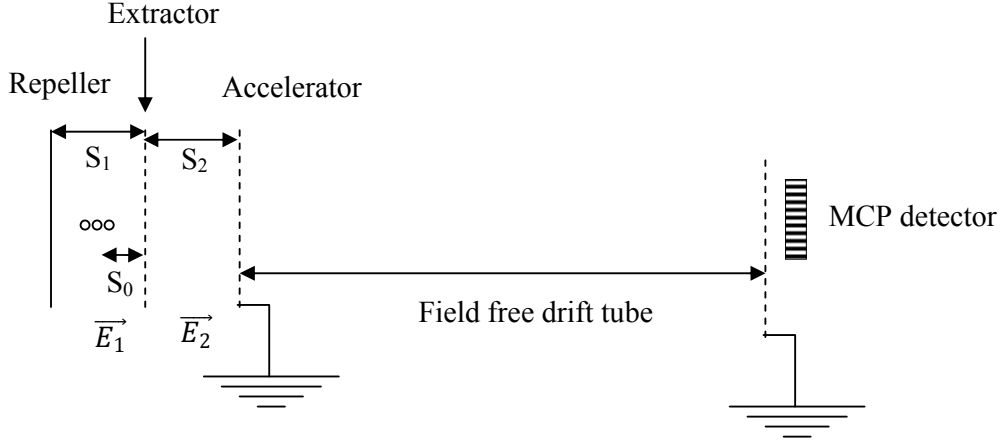


Fig. 2.4: Schematic of the time-of-flight mass spectrometer (TOF-MS).

flight time is proportional to the square of the ion mass i.e. $t \propto \sqrt{m}$.

And hence, mass resolution can be expressed as

$$\frac{m}{\Delta m} = \frac{t}{2\Delta t}.$$

In our experimental conditions $t \sim 32 \mu\text{s}$ and $\Delta t \sim 20 \text{ ns}$. So the mass resolution is about 800. For normal operation of TOF-MS, DC extraction and acceleration field was used. Pulsed electric field was used to study autoionization spectra. Two pulsed high voltage sources for extraction and acceleration were developed using DC high voltage power supply modules (Applied Kilovolts, UK) and fast transistor switches (HTS 61-05, Behlke, Germany).

2.3.2 Temporal width of the ion signal

The temporal width, Δt , of an ion signal (FWHM) decides the mass resolution and sensitivity of a TOF-MS. It depends on the duration of the laser-atom interaction time,

longitudinal velocity distribution and spatial distribution of ions. Typical photoionization signal of atomic uranium obtain from TOF-MS is shown in Fig. 2.5. Figure shows the temporal width of the ion signal is about 20 ns. Laser atom interaction time was about 5 ns (FWHM). So the major factors contributing to the temporal width were longitudinal velocity distribution of ions and spatial distribution of ions.

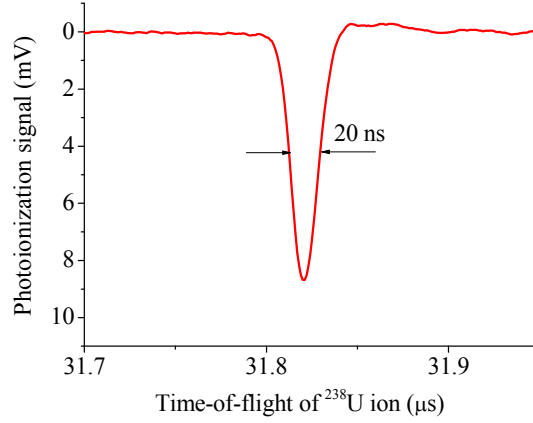


Fig. 2.5: Typical photoionization signal of $^{238}\text{U}^+$ in TOF-MS.

2.3.2.a) Effect of initial velocity distribution of ions on the temporal width

Due to thermal velocity distribution, there is a spread in the initial velocity of ions along the direction of the electric field. The ions which are moving towards the direction of the electric field will reach the detector at an earlier time compared to the ions with zero velocity. Similarly, the ions which are moving opposite to the direction of the electric field, have to be decelerated to zero velocity and then accelerated towards the detector, thus it will reach the detector at later time compared to the zero velocity group. Temporal profile of the TOF depends on the projection of the velocity distribution which is Gaussian along the electric field direction. FWHM of Gaussian TOF profile can be expressed as [52,107]

$$\Delta t_v = \frac{2\sqrt{(\ln 2)2mkT}}{eE_1}$$

For $m = 238$, $T = 1850$ K and $E_1 = 120$ V/cm, the temporal width due to the initial velocity spread is $\Delta t_v = 140$ ns. Contribution from the velocity distribution is expected to be more than 7 ns for collimated atomic beams used in the present work.

2.3.2.b) Effect of spatial distribution of ions on the temporal width

The flight time of ions depends on the initial spatial position. The ions which are created near the extraction grid will reach the extraction grid at a lesser time compared to the ions created far from the extraction grid. Just after the extraction grid, they will have different velocities due to difference in the kinetic energy acquired in the extraction region. So, after passing through the extraction grid both the ions will meet at some point in the space which is called the space focus point. In absence of accelerating grid, space focus points will be closer to the extraction grid. In the Wiley-McLaren geometry, space focus point is shifted at the end of the drift tube by using combination of two (extraction and acceleration) electric fields. Ratio of the electric fields between the acceleration and extraction region decides the location of space focus point. According to the detailed analysis on time-of-flight [107], the length of the drift tube (D) (i.e. approximately the distance between ion source and the detector) can be expressed as

$$D = 2s_0k_0^{3/2} \left(1 - \frac{1}{\left(k_0 + k_0^{1/2}\right) \frac{s_2}{s_0}} \right) \quad (2.1)$$

$$\text{Where, } k_0 = 1 + \frac{s_2 E_2}{s_0 E_1}$$

Where E_1 and E_2 are the electric field in the extraction and acceleration region, S_0 is the position of the ion from the extraction grid; S_2 is the separation between extractor and accelerator grids (Fig. 2.4). At space focal point mass resolution can be expressed as [52]

$$\frac{m}{\Delta m} = \frac{t}{2\Delta t} \approx 16k_0 \left(\frac{s_0}{\Delta s} \right)^2 \quad (2.2)$$

where ΔS is the length of the ionization region in the direction of the electric field. The detector is placed at the space focus point to minimize the temporal width of the signal due to initial spatial distribution. For $s_0 = 0.8$ cm, $\Delta s = 0.4$ cm, $s_2 = 1.6$ cm, $E_1 = 120$ V/cm and $E_2 = 1,600$ V/cm equation (2.2) yields a resolving power of 1770. For the drift time of $32 \mu\text{s}$, the contribution due to spatial distribution of atoms to Δt is about 8 ns. Thus, under the present conditions the observed temporal width of 20 ns of the photoionization signal is the sum of all these factors as expected.

2.4 U-Ne Hollow cathode discharge tube

It consisted of a hollow cylindrical cathode (inner diameter 8 mm, length 30 mm) made of natural uranium and annular anode made of tantalum encapsulated in a glass tube (Fig. 2.6).



Fig. 2.6: U-Ne HCDT used for photoionization optogalvanic spectroscopy of uranium.

Ne was used as buffer gas at a pressure of ~ 2 mbar. Hollow cathode discharge tube was operated in the normal glow discharge regime i.e. with increasing current, voltage across the discharge remains constant. Due to its electrical properties, HCDs are excellent source of

sputtering of their cathode material and, consequently, generator of spectroscopic quality atomic vapor as well as an efficient detector of the absorbed photons, laser produced photo ions and photo electrons. The buffer gas ions present inside the discharge tube acquire energy from the high electric field present in the cathode dark space and generate atomic vapor of cathode material on impinging on the cathode surface via sputtering. In the sputtering process small fraction of ions of the cathode material and electrons were also generated. These secondary electrons are responsible for sustaining the discharge. In the present thesis work, HCDDT has been used for two purposes: a) recording of optogalvanic spectra for absolute wavelength calibration in the measured photoionization spectra and b) photoionization spectroscopy of atomic uranium to measure atomic parameters.

2.5 Signal monitoring and processing devices

Various signal monitoring devices like photodiode, Fabry-Perot (FP) etalon, digital storage oscilloscope, laser power meter etc. and signal processing devices like fast pre-amplifier, box car averager etc. have been used for measuring atomic parameters of uranium.

2.5.1 Photodiode

A photodiode is a reversed biased semiconductor p-n junction that converts light into an electrical current. The current is generated when photons are absorbed in the p-n junction. Photodiodes are similar to normal semiconductor diodes with optically transparent window to allow light to reach the depletion region. Fast photodiodes use a PIN junction rather than a p-n junction, to increase the speed of response. In PIN junction, intrinsic semiconductor layer is introduced to increase the

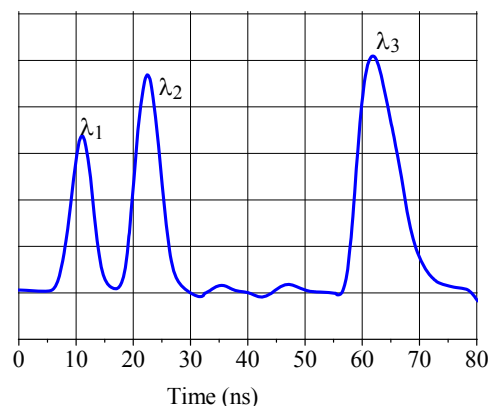


Fig. 2.7: Temporal profile of the laser pulses

width of the depletion region which results in a lower capacitance and hence a smaller rise time. PIN type photodiode was used for checking the temporal delays between the laser pulses and to monitor the output of the transmission signal of the Fabry-Perot etalon which was used as a fine frequency marker for calibration of photoionization spectra. Fig. 2.7 shows the temporal profile and typical time sequence of the laser pulses used for photoexcitation and photoionization cross section measurements.

2.5.2 Fabry-Perot etalon (FPE)

In the present work, FPE was used for wavelength calibration and for estimating the laser line widths. The free spectral range (FSR) of the FPE was 0.5 cm^{-1} . It consisted of two highly reflecting surface separated by an air gap. A part of the laser beam was passed through the

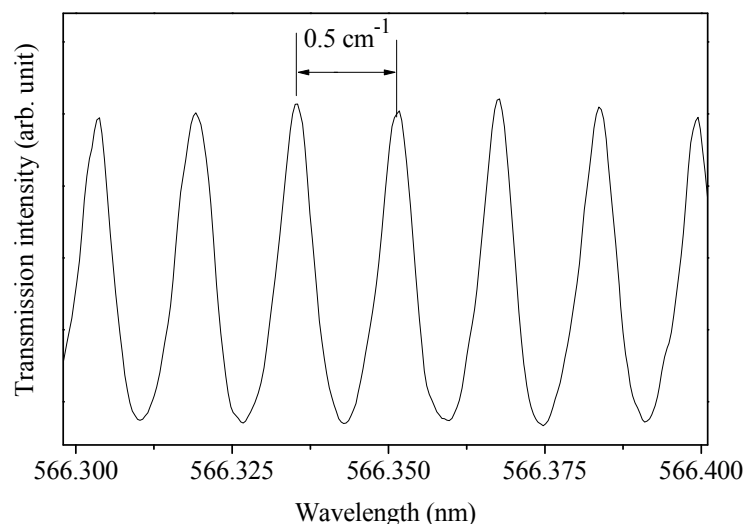


Fig. 2.8: Transmission intensity of the Fabry-Perot etalon ($\text{FSR} = 0.5 \text{ cm}^{-1}$) as a function of laser wavelength

Fabry-Perot etalon (FPE) for relative frequency and line width measurements. It works on the principle of multiple beam-interference. Transmitted intensity of the FPE depends on the type of interference (constructive or destructive) among the successive transmitted beams. For constructive interference path difference has to be integral multiple of wavelength i.e. $2d \cos$

$(\theta) = n \lambda$, where d is the separation between the reflecting surfaces, θ is the angle of incidence, n is the interference order number. For FP etalon d is fixed, thus condition for constructive or destructive interference is satisfied either due to the change of λ or θ . When wavelength of the laser is scanned, transmission peaks separated by free spectral range (FSR) are produced. These transmission fringes are used as a relative frequency marker, as shown in Fig. 2.8.

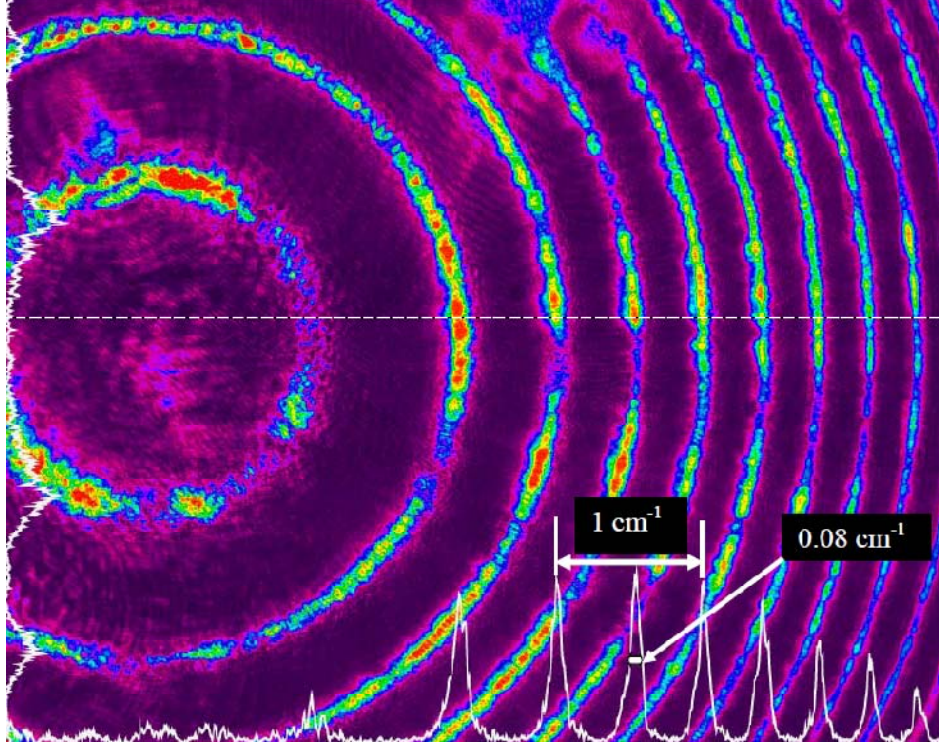


Fig. 2.9: Part of the circular fringe formed by the diverging laser beam. Separation between two bright fringes is 0.5 cm^{-1} .

For line width measurements diverging laser beam (different θ) was produced using a concave lens and it was made to pass through the FPE. Output of the FPE was focused by converging lens and captured by a CCD camera based beam profiler. Here depending on the angle of incidence, bright and dark circular fringes are formed. A part of the circular fringes along with the intensity profile is shown in the Fig. 2.9.

2.5.3 Digital storage oscilloscope

A digital storage oscilloscope (No. of channel:4 Nos, bandwidth : 500 MHz, Model No. DSO 7054A, Agilent technologies) was used for monitoring and storing of photoionization signal, photodiode signal, trigger signal and box car averager gate etc. during the experiments. For some of the experiments Rigol make 4-channel, 200 MHz digital storage oscilloscope was also used.

2.5.4 Laser power meter

It consists of a power sensor and a display meter (VEGA). Different thermal type sensors were used for measuring Nd:YAG and dye laser power. The sensor with model No. 30A-BB-18, Ophir Optronics, Israel was used for measurement of Nd:YAG laser power. It can measure laser power (pulsed energy) from 10 mW to 30W (6mJ to 30J) in the wavelength region of 190 to 20000 nm. The sensor with model No. 3A -P (Ophir Optronics, Israel) was used for measurement of dye laser power. It can measure laser power (pulsed energy) from 15 μ W to 3W (20 μ J to 2J) in the wavelength region of 150 to 8000 nm. In these sensors, laser power was measured by measuring the temperature rise due to absorption of incident radiation. Inside the sensor there are series of bimetallic junctions (thermopile) which converts the radial or axial heat flow into electrical voltage which is proportional to the change of temperature. Since, only the temperature difference is measured, the power measurement is independent of ambient temperature.

2.5.5 Wavelength meter

Fizeau interferometer based wavelength meter (WS 06, High Finesse, Germany) was used to measure the laser wavelength during the experiments. The accuracy of the measured wavelength was ± 600 MHz throughout the visible wavelength region.

2.5.6 Fast pre-amplifier

A fast pre-amplifier was used to amplify the tiny output of the micro channel plate detector. The gain and bandwidth of the amplifier was 70 and 300 MHz. In most of the experiments, after amplification, the magnitude of the photoionization signal observed was in the range of 5 to 200 mV.

2.5.7 Box-car averager

Box-car averager (Model No. BA5509, ECIL, Bangalore) was used to improve the signal to noise ratio by averaging and integrating repetitive pulsed signal. This is basically a RC integrator. The width of the gate and its temporal position in relative to the trigger was adjusted to optimize the DC output. Trigger signal was obtained either from the Q-switched output of the Nd:YAG laser or from the delay generator. The DC output was used for recording the photoionization spectra.

Chapter 3 - Numerical study of photoexcitation dynamics using population rate equations

3.1 Introduction

Numerical study of the photoexcitation dynamics in a multi-step photoionization process is essential to understand the role of various atomic parameters such as radiative lifetimes, branching ratios, transition probabilities, photoexcitation/photoionization cross sections and various laser parameters like laser linewidths, laser energy densities, temporal delays among laser pulses etc. on the photoionization yield. Based on the phase relationship between the electric field of the laser and atomic medium, laser atom interactions are described as coherent or incoherent. In coherent laser atom interaction, there exists a definite phase relationship between atom and electromagnetic field. In such cases, the excitation dynamics is best described by density matrix equations. In case of incoherent interaction, population rate equations can be used instead of complicated density matrix equations. In this chapter, photoionization yield in a multistep photoionization process have been studied for different laser pulse widths, temporal delays, energy densities, and laser polarizations etc. using population rate equations.

In laser atom interaction, the coherence preserving processes are stimulated absorption and stimulated emission. Coherence destroying processes are loss of excited state population by means of collisional decay, radiative decay and photoexcitation/photoionization etc. The interactions can definitely be said incoherent if either of the following conditions prevails [95,108,109]:

- Stimulated absorption rates are smaller compared to spontaneous/collisional decay rates.

- Monotonic flow of population exist in the photoionization pathways i.e. in case of three-step photoionization process $R_3 > R_2 > R_1$. Where R_i denotes the photoexcitation or ionization rate in the i^{th} step. In this case, excited population is further excited or ionized before the population pulsation can occur between two levels.
- Coherence time (τ_c) which is equal to the inverse of the laser bandwidth i.e. $\tau_c = 1/\Delta\nu_L$, is much shorter compared to the laser-atom interaction time i.e. temporal width of the laser pulse ($\Delta\tau$). This is very true for broadband and multimode lasers.
- Rabi frequency of the transition is smaller compared to the laser linewidth.
- Laser output consists of many longitudinal modes and there is no definite phase relationship exists among the various modes.

3.2 Population rate equations

In case of incoherent excitation, photoexcitation dynamics can be described by the population rate equations [108]. In this population rate equation model, atoms are characterized by level population and laser light is characterized by intensity. As mentioned earlier, the ionization potential of atomic uranium is 6.1941 eV. The photon energy in the visible region of the electromagnetic spectrum is ~ 2 eV. Therefore, three visible photons are required to ionize the uranium atom. Thus, it is necessary to investigate the excitation dynamics in a three-step three-photon photoionization process. The starting point in understanding any photoionization scheme is single step photoexcitation i.e. absorption of one photon between two bound atomic levels.

3.2.1 Single step photoexcitation in a closed two-level system

A representative closed two-level atomic system is depicted in Fig. 3.1. Here, the lower level is considered as ground or metastable level.

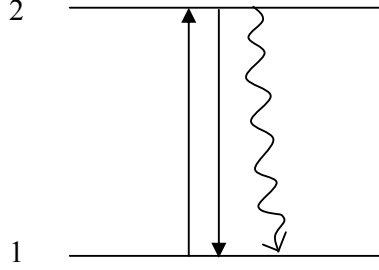


Fig. 3.1: Single photon absorption and emission in a closed two level system.

The population rate equations for unpolarized and spatially uniform light can be expressed as

$$\frac{dn_1}{dt} = -W \left(n_1 - \frac{g_1}{g_2} n_2 \right) + A_{21} n_2 \quad (3.1a)$$

$$\frac{dn_2}{dt} = W \left(n_1 - \frac{g_1}{g_2} n_2 \right) - \frac{n_2}{\tau_2} \quad (3.1b)$$

Where n_1 and n_2 denotes time dependent population of atoms in level 1 and 2, respectively, g_i [$g_i = (2J_i + 1)$] is the degeneracy, J_i is the total angular momentum of i^{th} level. W is the excitation rate which is expressed as $W = \frac{I\sigma_{12}}{\hbar\omega}$. Here, I is the intensity of the laser and σ_{12} is the photoexcitation cross section of the transition for a chosen laser and atomic absorption linewidth. Here laser linewidth is assumed to be very large compared to the atomic absorption linewidth and the laser frequency is exactly tuned to the resonance. In the case of photoexcitation where the atomic absorption linewidth is much lesser than the laser linewidth ($\Delta\omega_L$), σ_{12} is related to the transition probability (A_{21}) by the following expression [52,110],

$$\sigma_{12} = \frac{g_2}{g_1} \frac{\lambda^2}{4} \frac{A_{21}}{\Delta\omega_L} \quad (3.1c)$$

The transition probability (A_{21}) is related to the branching ratio (β_{21}) and the radiative lifetime (τ_2) of the upper level by the following relation

$$A_{21} = \frac{\beta_{21}}{\tau_2} \quad (3.1d).$$

Let the initial conditions at $t = 0$ are $n_1(0) = N$ and $n_2(0) = 0$. Substituting $n_1(t) = N - n_2(t)$ in equation 3.1b and integrating, we get

$$n_2(t) = \frac{WN}{x} (1 - e^{-xt}) \quad (3.1e)$$

$$n_1(t) = N - n_2(t) \quad (3.1f)$$

where $x = \left(\left[\frac{g_1 + g_2}{g_2} \right] W + \frac{1}{\tau_2} \right)$.

Time dependent populations of level 1 and 2 for two different excitation rates for continuous wave (CW) excitation are shown in Fig. 3.2. At $t \rightarrow \infty$ (in reality $t = 5\tau_2$ can be considered

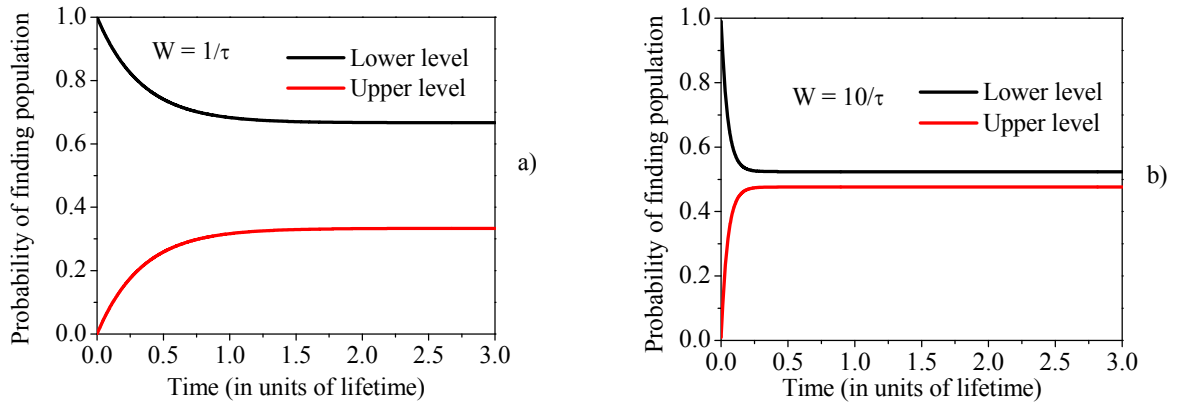


Fig. 3.2: Time evolution of the atomic populations in a closed two-level systems under continuous laser excitation for different excitation rates a) $W=1/\tau$, b) $W=10/\tau$.

as infinite time) population in the upper level reaches a steady value equal to $n_2(t) =$

$\frac{WN}{\left(\left[\frac{g_1 + g_2}{g_2} \right] W + \frac{1}{\tau_2} \right)}$. When excitation rate is equal to spontaneous decay rate (saturation parameter

$=1$) [3], equilibrium population in the upper level becomes 33.3% of the total population for

$g_1=g_2$ (Fig. 3.2a). At this excitation rate, the absorption coefficient $[\alpha = (n_1 - n_2)\sigma_{12}]$ becomes

half of its maximum value. When excitation rate is very high compared to the radiative decay

rate, populations in both the levels tend to become equal, as shown in Fig. 3.2b. For $W \gg \frac{1}{\tau_2}$,

$n_2(t) = \frac{g_2}{(g_1+g_2)} N$. So, maximum population in the upper level will be equal to 50% of the total population for equal level degeneracy i.e. $g_1 = g_2$. In case of $J_1 = 0$ to $J_2 = 1$ transition i.e. respective level degeneracies are $g_1 = 1$ and $g_2 = 3$ and thus 75% of the ground state population can be raised to the upper level.

3.2.1.1 Excitation by pulsed laser

In case of the pulsed laser, the total population at the end of the laser pulse is observed for any spectroscopic measurements. The upper level population at the end of the laser pulse (i.e. $t = \Delta\tau$) can be expressed from equation 3.1e as

$$n_2 = \frac{g_2}{(g_1+g_2)} N \left(1 - e^{-\left[\frac{g_1+g_2}{g_2}\right] W \Delta\tau + \frac{\Delta\tau}{\tau_2}} \right) \quad (3.1g).$$

Here, the laser pulse profile is assumed to be rectangular in time. For equal degeneracy ($g_1 = g_2$) the above equation can be written as

$$n_2 = \frac{N}{2} \left(1 - e^{-\left(2\phi\sigma + \frac{\Delta\tau}{\tau_2}\right)} \right) \quad (3.1h).$$

Here $W\Delta\tau = \left(\frac{I\Delta\tau}{\hbar\omega}\right)\sigma$ and the quantity inside the parenthesis represents the photon fluence ϕ i.e. number of photons per pulse per unit area.

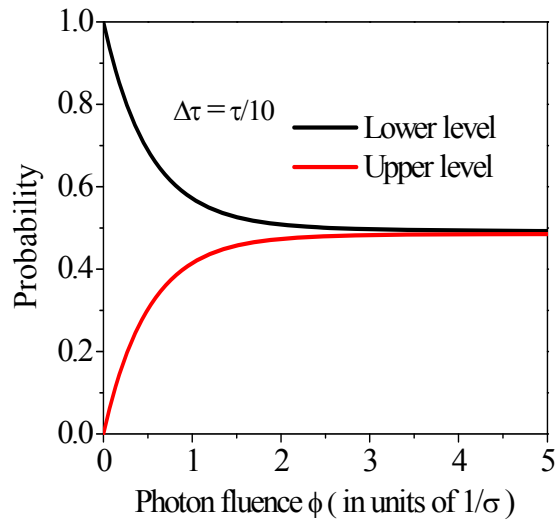


Fig. 3.3: Probability of atoms in a closed two level system as a function of the photon fluence at the end of a laser pulse. Laser pulse width ($\Delta\tau$) have been taken as one tenth of the upper level lifetime (τ).

If $\Delta\tau \ll \tau_2$ and $W \gg \frac{1}{\tau_2}$ then the equation (3.1g) simplifies to

$$n_2 = \frac{N}{2} (1 - e^{-2\phi\sigma}) \quad (3.1i)$$

So for the pulsed laser, photon fluence/ energy density is more meaningful than the intensity as it decides the upper level population at the end of the laser pulse. Fig. 3.3 shows the upper level population as a function of the product of cross section and laser photon fluence. From the figure, it is observed that for $\sigma\phi \ll 1$, upper level population is very small. Initially, upper level population increases linearly with increasing laser photon fluence but for $\sigma\phi > 1$ it tends to saturate. The variation of upper level population with photon fluence or energy is called saturation curve.

To quantify the saturation of a transition for a given pulsed energy/photon fluence, a quantity called saturation energy/photon fluence is frequently used. From the equation (3.1i) saturation photon fluence can be derived by making the exponent equal to one i.e. $2\phi_{sat}\sigma = 1$ or $\phi_{sat} = \frac{1}{2\sigma}$. Thus, saturation energy is $E_{sat} = \hbar\omega\phi_{sat} = \frac{\hbar\omega}{2\sigma}$. The population in both the levels becomes almost equal when the laser energy is equal to five times of the saturation energy (i.e. $\phi_{sat}\sigma = 2.5$ in Fig. 3.3) and further increase of laser energy does not change the level population.

3.2.1.2 Effects of branching ratios and radiative lifetimes

In the previous discussion branching ratio has been assumed equal to one. But in reality, it can have any values in between 0 to 1. Fig. 3.4 shows the saturation curves for various combinations of branching ratios and radiative lifetimes. It should be noted here that for all the combinations, cross sections are same as the ratios between the branching ratios and the radiative lifetimes are considered equal. It is observed from the figure that curvature of the saturation curve is similar for all the plots but absolute values of the upper level population decreases with decreasing radiative lifetimes and branching ratios.

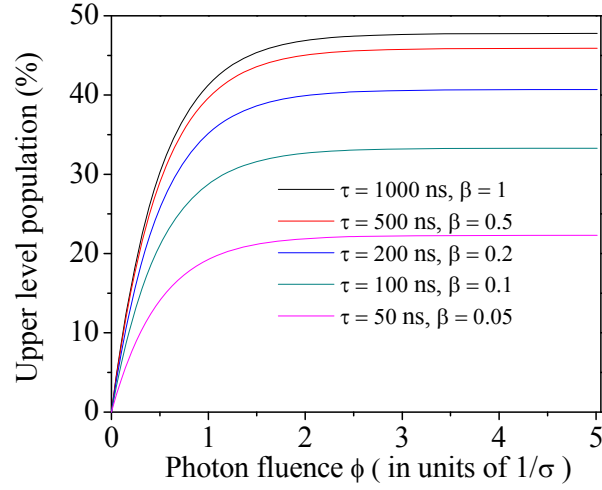


Fig. 3.4: Saturation curves for different transitions with same cross section values but different branching ratios and radiative lifetimes in a two level system.

3.2.1.3 Saturation of transitions for different cross sections

Fig. 3.5 shows the variation of upper level population with laser fluence for different cross section values. It is observed that for same photon fluence curvature of the saturation curves is different for different cross section values. Initially all the populations are in the

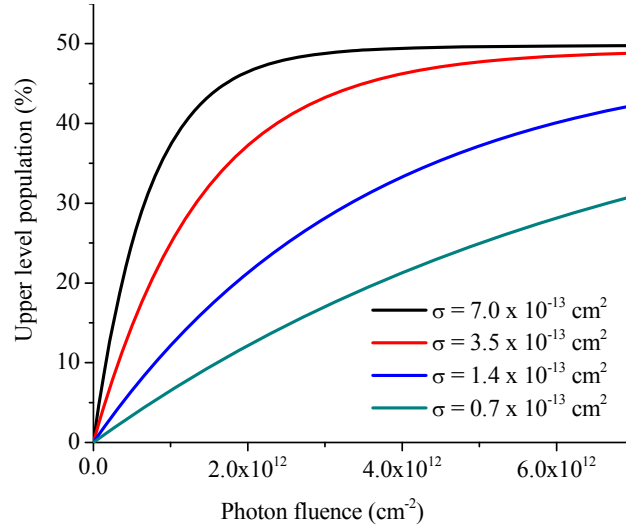


Fig. 3.5: Saturation curves of different transitions with different cross section values in a two-level system

lower (ground) level, so upward transition due to stimulated absorption will increase the upper (excited) level population. When there is a population in the excited level, there will be

a down ward transition too. So, within the laser pulse both upward and downward transitions will take place and at the end of the laser pulse there will be significant fraction of the ground level population in the excited level depending on the laser fluence/energy. Excited level population increases initially linearly but finally saturates with increasing laser pulse energy.

It is important to know the saturation energy of a transition for a particular laser and atomic absorption line widths. This helps in proper utilization of laser power to optimize the photoionization yield. As an example, let us consider a transition with $J_1 = J_2$, $\tau_2=200$ ns, $\beta_{21}=1$, $\lambda = 600$ nm and $\Delta\omega_L = 2$ GHz. So, the transition probability (A_{21}) of the transition according to the relation (3.1d) is $5 \times 10^6 \text{ s}^{-1}$, the average photo excitation cross section according to the equation (3.1c) is $3.57 \times 10^{-13} \text{ cm}^2$. So, saturation photon fluence and energy are 1.4×10^{12} photons per cm^2 per pulse and $0.46 \text{ }\mu\text{J}/\text{cm}^2$, respectively. For a particular laser and atomic absorption linewidths, the cross sections of various transitions differ mainly due to different values of the transition probabilities.

3.2.2 Single step photoionization in an open two-level system

When photon energy is greater than the ionization potential of the element, photoionization of ground level is possible through absorption of a single photon. In a multistep photoionization process, when laser pulses are separated in time, the final step transition can be considered as single step photoionization from the excited level. In case of photoionization, there is no downward radiative transition from the autoionizing level/continuum to the lower level. Assuming the laser is unpolarized, spatial intensity profile is uniform and the temporal profile is rectangular, the population rate equations for single step photoionization from the excited level, as shown in Fig. 3.6, can be written as

$$\frac{dn_{ex}}{dt} = -W_i n_{ex} - \frac{n_{ex}}{\tau_{ex}} \quad (3.2a)$$

$$\frac{dn_i}{dt} = W_i n_{ex} \quad (3.2b)$$

Where n_{ex} and n_i represents the excited level population and ion population, respectively.

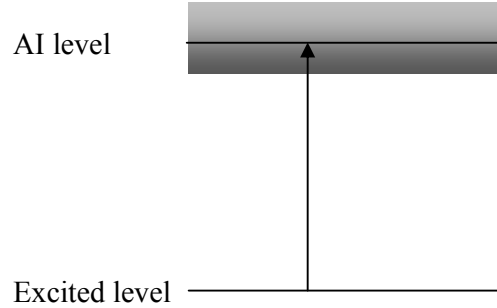


Fig. 3.6 Single step photoionization of excited atom via autoionizing (AI) level. Atom excited to an autoionizing level spontaneously decays to a free electron and an ion.

Using similar approximation for pulsed laser excitation as discussed in section 3.2.1.1 solution of the above equations can be written as

$$n_i = n_{ex}(1 - e^{-\phi_i \sigma_i}) \quad (3.2c)$$

Where ϕ_i is the photon fluence of the ionizing laser and σ_i is the ionization cross section.

3.2.3 Three-step photoionization

Three-step photoionization of the uranium atom through autoionizing level can be considered as a four level atomic system (Fig. 3.7). Atom excited into an autoionizing level spontaneously decays into a free electron and an ion.

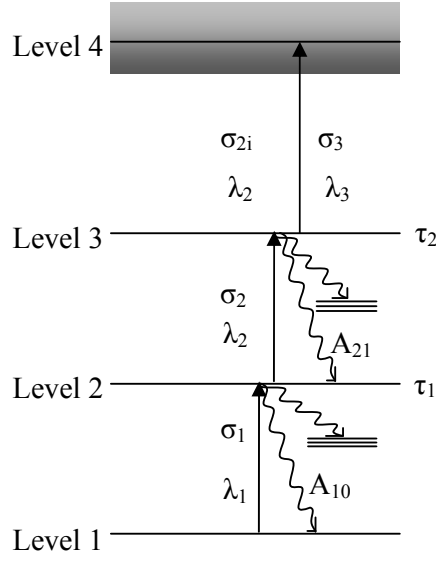


Fig. 3.7: Typical three step photoionization pathways.

3.2.3.1 Population rate equations for three-step photoionization pathways

The population rate equations for the three-step photoionization pathways as depicted in Fig. 3.7, can be written as

$$\frac{dn_1}{dt} = -\left(n_1 - \frac{g_0}{g_2} n_2\right) W_1(t) + A_{21} n_2 \quad (3.3a)$$

$$\frac{dn_2}{dt} = \left(n_1 - \frac{g_1}{g_2} n_2\right) W_1(t) - \left(n_2 - \frac{g_2}{g_3} n_3\right) W_2(t) + A_{32} n_3 - \frac{n_2}{\tau_2} \quad (3.3b)$$

$$\frac{dn_3}{dt} = \left(n_2 - \frac{g_2}{g_3} n_3\right) W_2(t) - \frac{n_3}{\tau_3} - W_3(t) n_3 \quad (3.3c)$$

$$\frac{dn_i}{dt} = W_3(t) n_3 \quad (3.3d)$$

where, n_j is the atomic population, g_j is the level degeneracy, τ_j is the radiative lifetime of j^{th} level and $A_{j(j-1)}$ is the transition probability between j^{th} and $j-1^{\text{th}}$ levels. $W_j(t)$ represents photoexcitation or photoionization rate of the j^{th} step transition which is written as

$$W_j(t) = \frac{\sigma_j \phi_j}{\Delta t_{jL}} f_{jL}(t) \quad (3.3e)$$

where σ_j is the average cross-section of the j^{th} step transition, ϕ_j is the photon fluence i.e. number of photons per unit area per pulse. The photon fluence is related to the pulse energy density (E_d) and photon flux (Φ_j) by the expressions: $\phi_j = E_d / \text{photon energy}$ and $\phi_j = \Phi_j \Delta t_{jL}$ respectively, Δt_{jL} is the temporal width (FWHM) of the j^{th} step laser and $f_{jL}(t)$ is the Gaussian temporal profile of the j^{th} step laser, which can be expressed as

$$\begin{aligned} f_{1L}(t) &= \frac{2(\ln(2))^{1/2}}{\pi^{1/2}} \exp \left\{ - \left(\frac{t-t_0}{\Delta t_{1L}} \right)^2 \right\} \\ f_{2L}(t) &= \frac{2(\ln(2))^{1/2}}{\pi^{1/2}} \exp \left\{ - \left(\frac{t-(t_0 + D_{12})}{\Delta t_{2L}} \right)^2 \right\} \\ f_{3L}(t) &= \frac{2(\ln(2))^{1/2}}{\pi^{1/2}} \exp \left\{ - \left(\frac{t-(t_0 + D_{12} + D_{23})}{\Delta t_{3L}} \right)^2 \right\} \end{aligned}$$

Here t_0 is the time corresponding to the peak intensity of the first laser pulse. D_{12} and D_{23} are the temporal delays between first & second and second & third lasers respectively. For a known laser linewidth ($\Delta\omega_L$) and transition probability, the average cross section σ_j can be determined using equation 3.1c.

In case of synchronous three-step photoionization process, saturation energy of a transition changes significantly in comparison to single step excitation or ionization due to simultaneous participation of all the levels. Under the conditions, when the laser pulses are rectangular in time, spontaneous emission from excited levels is negligible and excitation rates of the k^{th} step transition is more compared to $(k-1)^{\text{th}}$ step, then saturation photon fluence/energy of k^{th} step transition of a three-step photoionization process can be expressed as [26,52]

$$\phi_{sat}^k = \frac{k}{\sigma_k} \quad \text{or} \quad E_{sat}^k = \frac{k\hbar\omega}{\sigma_k} \quad (3.3f)$$

k is equal to 1, 2, 3 for first, second and third step transitions respectively. Also, $\hbar\omega$ represents energy of the photon.

To understand the dependence of photoionization yield on various atomic parameters, a three-step photoionization scheme is considered with the following parameters: $J_1=J_2=J_3=J_{AI}=6$, $\beta_{21}=0.5$, $\tau_2=200$ ns, $\beta_{32}=0.05$, $\tau_3=200$ ns, σ_i (ionization cross section) = 10^{-16} cm², $\Delta t_{jL} = 5$ ns, $\Delta\omega_L = 2.4$ GHz. For the purpose of photoionization yield calculation, the maximum photon fluence of the first, second and third step lasers were taken as $\phi_1 = 15/\sigma_1$ cm², $\phi_2 = 15/\sigma_2$ cm², $\phi_3 = 15/\sigma_3$ cm² and the initial populations as $n_1 = 100$, $n_2=0$, $n_3 = 0$ and $n_i = 0$. In order to calculate the photoionization yield, the coupled differential equations (3.3a) to (3.3d) have been solved using fourth order Runge-Kutta method.

3.2.3.2 Temporal evolution of atomic populations among various levels

It is important to study the time evolution of the atomic populations among various levels to optimize the photoionization yield. Fig. 3.8a and b shows the temporal sequence of the synchronous and delayed laser pulses. Fig. 3.9a and b shows the temporal evolution of the atomic population among the various levels for synchronous and delayed laser pulses. In case of delayed laser pulses, the lower level population gets distributed between the two levels of the respective transitions (Fig. 3.8a). However, after initial rise, the population of the excited levels decrease with time due to spontaneous decay which results in a small increase in the ground level population with time. In case of synchronous laser pulses (Fig. 3.9b) the ion population continuously increases (blue line) and ground level population continuously decreases with interaction time, as shown in 3.9a. Intermediate population initially increases and reaches to a maximum at certain time and then finally decreases.

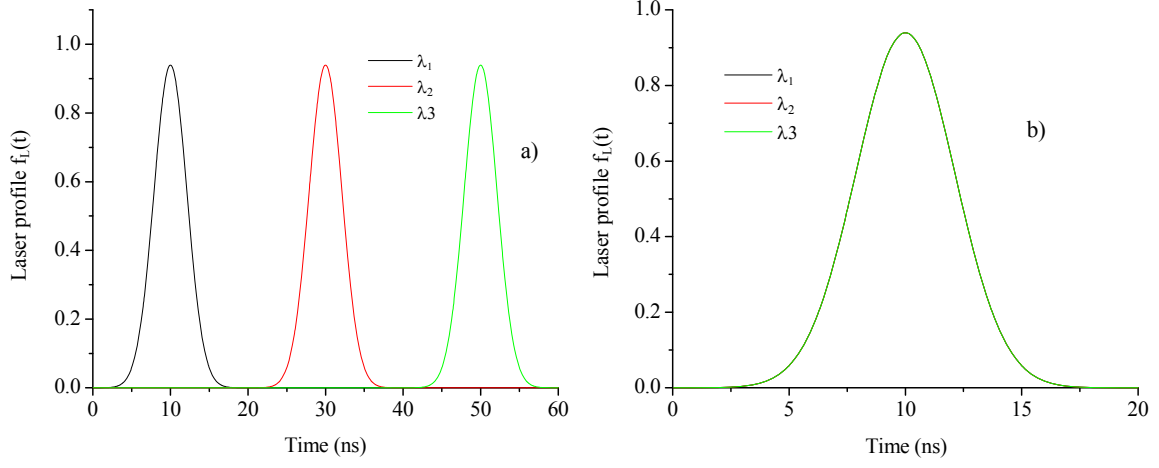


Fig. 3.8: Temporal profile of the laser pulses under a) delayed and b) synchronous condition.

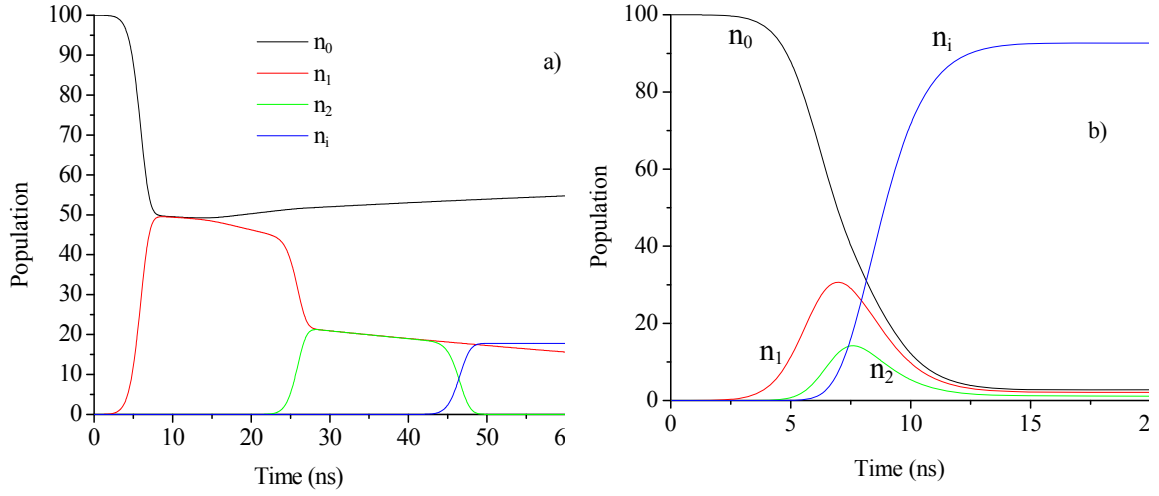


Fig. 3.9: Time evolution of atomic population in various levels for a) temporally separated laser pulses and b) temporally synchronous laser pulses.

3.2.3.3 Dependence of photoionization yield on laser fluence/pulse energy

The dependence of photoionization yield on laser fluence in each step is investigated for two different cases i.e. when all the three lasers are totally disconnected in time (delayed system) and secondly when they are completely synchronized. The variations in photoionization efficiencies on the 1st, 2nd and 3rd step laser fluence respectively for temporally separated laser pulses are shown in figure 3.10 a, b & c. Similarly for the synchronize case it is shown in figure 3.11 a, b & c. In these calculations, laser fluence in one of the step is changed while keeping the other two are constant. The importance of these studies is realized when the excitation/photoionization cross-sections are determined by saturation method. As is evident from the figures the behavior of photoionization yield/efficiency is distinctly different in these two cases. In case of delayed system the atom can be considered as a two level system and the experimental curves can be fitted to a simpler solution of the population rate equations of the two-level system. But in synchronized case there is a continued upward flow of atomic population during the excitation, therefore all the levels involved in excitation are coupled to each other. In such cases the experimental curves cannot be fitted to the simple solution of the population rate equations of the two-level system otherwise it may lead to erroneous results. Another important result is that in case of delayed system the maximum yield one can achieve in three-step process is close to 25% of the atomic population available in the ground level. However in synchronized case the yield can be as high as close 100%.

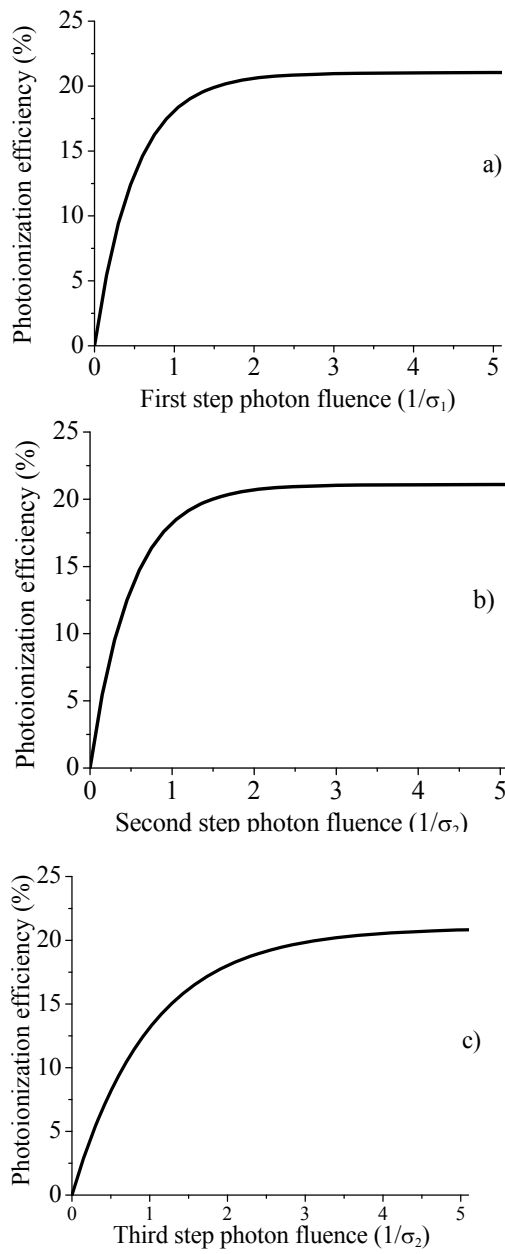


Fig. 3.10: Photoionization efficiency as a function of a) first, b) second and c) third laser photon fluences for temporally separated laser pulses.

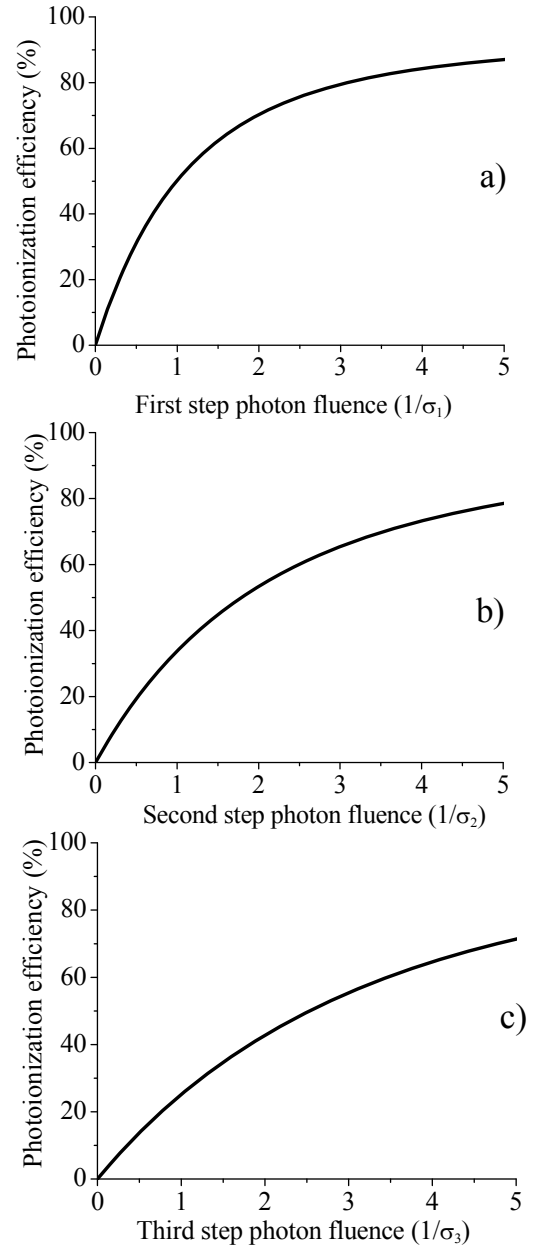


Fig. 3.11: Photoionization efficiency as a function of a) first, b) second and c) third laser photon fluences for synchronous laser pulses.

3.2.4 Effects of laser polarization on the saturation curve/photoionization efficiency.

So far we have not considered the effects of laser polarization in the calculations of photoionization yield i.e. the transition strength among the various magnetic sublevels have been considered equal. In a real situation lasers can be polarized (in the present case, dye lasers are polarized due to use of grating and Brewster window in the oscillator and amplifier) and hence individual transition between the magnetic sublevels may need to be considered to understand the population dynamics. In case of multi-step photoionization with unpolarized light, the populations of all the magnetic sublevels are excited and ionized uniformly and hence individual magnetic sublevels pathways need not to be considered. But in case of the excitation with polarized laser, transition strength (cross section) among the magnetic sublevels depends on the m_j values i.e. Z component of the total angular momentum quantum number (J) and hence transition among the magnetic sublevels need to be considered, individually for photoionization yield calculation. There are $(2J+1)$ magnetic sublevels corresponding to the total angular momentum J of a level and hence there are $2J+1$ independent photoexcitation pathways for $J \rightarrow J$ transition. As an example, for a photoionization scheme with J sequences $6 \rightarrow 6 \rightarrow 6 \rightarrow 6$, there are 13 independent magnetic sublevel pathways. To calculate the total photoionization yield (N_i), ionization yield (n_i) through each sublevel pathway, as shown in Fig. 3.12a, need to be calculated individually and summed over all the magnetic sublevels i.e. $N_i = \sum_{m=1}^{(2J+1)} n_i(m)$.

PI yield of different magnetic sublevel pathways can be calculated using equations (3.3a to 3.3d) by substituting the polarization dependent cross sections and assuming uniform distribution of ground level population among the magnetic sublevels. The polarization-

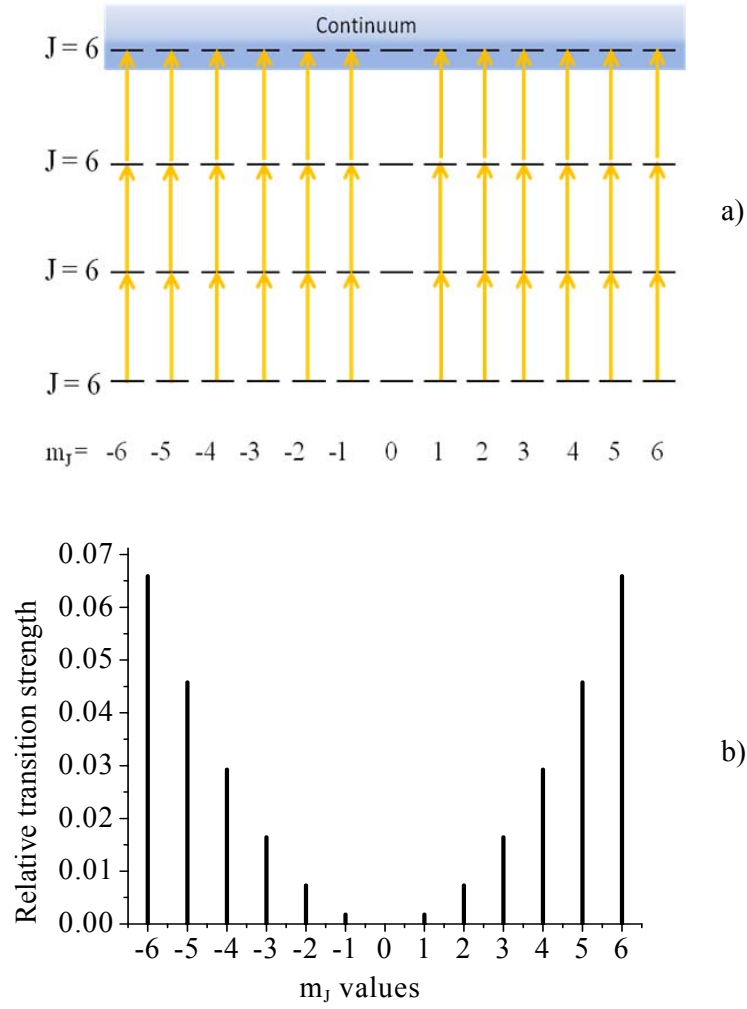


Fig. 3.12: a) Magnetic sublevel photoionization pathways for linearly polarized light. b) Relative transition strength between magnetic sublevels for linearly polarized light.

dependent cross section is related to isotropic cross section σ_{J_u, J_l}^i (for unpolarized laser) by the following relation [95]

$$\sigma_{J_u m_u, J_l m_l}^{q_i} = 3(2J_l + 1) \begin{pmatrix} J_u & 1 & J_l \\ -m_u & q_i & m_l \end{pmatrix}^2 \sigma_{J_u, J_l}^i$$

where J_u and J_l are the total angular momentum values of the upper and lower levels of a transition, q_i represents the change in the magnetic quantum number ($m_u - m_l$) which is equal to 0 for linear polarization. The relative variation of the transition strength between $J = 6 \rightarrow J = 6$

with linearly polarized laser is shown in Fig. 3.12b. Due to this variation in the transition strength, the saturation behavior of different magnetic sublevel transitions will be different, some sublevel transitions will be highly saturated and some sublevel transitions will be less saturated in comparison to the unpolarized one. But in the actual experiment total photoionization yield is observed instead of the contribution from the individual pathways.

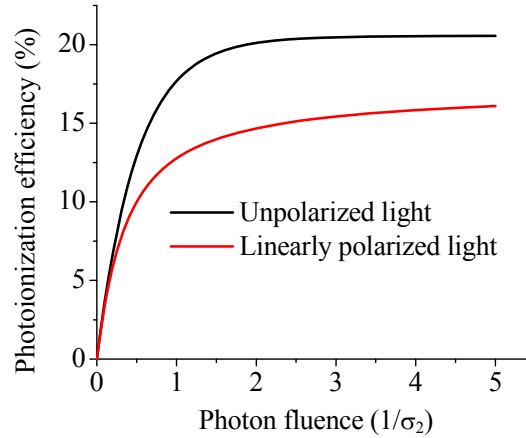


Fig. 3.13: Photoionization yield as a function of second step laser photon fluence for unpolarized and linearly polarized lasers when laser pulses are temporally separated.

As a test case, the photoionization yield as a function of second-step laser photon fluence has been studied for polarized and unpolarized lasers. Fig. 3.13 shows the saturation curve for both polarized and unpolarized excitation. It is clear from the figure that the laser polarization plays a very significant role in the absolute magnitude of the photoionization signal but curvature of the saturation curve does not change vary significantly. Since, only the curvature is important for determination of cross section rather than absolute magnitude, the photoexcitation/ionization by the temporally separated linearly polarized laser pulses can be considered as a two-level system. Measurement error due to this assumption is expected to be insignificant in comparison to other experimental errors which will be discussed in detail in chapter 5.

3.2.5 Calculation of photoionization efficiency in units of saturation fluence/energy

Knowledge of photoionization efficiency as a function of saturation energy/fluence is useful in applications based on multistep photoionization process. Fig. 3.14a and b shows the dependence of photoionization yield on the simultaneous variation of all the laser fluences/energy densities in units of saturation factor 's' for temporally synchronized laser pulses for two different photoionization schemes with J-sequences $6 \rightarrow 6 \rightarrow 6 \rightarrow 6$ and $6 \rightarrow 7 \rightarrow 8 \rightarrow 9$ for both polarized and unpolarized lasers. The photon fluence of the k^{th} step transition is defined as $\phi^k = s \phi_{sat}^k$, where ϕ_{sat}^k is the saturation photon fluence which is discussed in the previous section 3.2.3.1. We can see from the Fig. 3.14a that initially photoionization yield with polarized laser is more compared to unpolarized light due to large contribution from some of the magnetic sublevel pathways but for higher photon fluence, photoionization yield for unpolarized light is more due to uniform excitation and participation of all the magnetic sublevels. It is observed that the PI yields for photoionization pathways with increasing J-values are similar for both polarized and unpolarized lasers (Fig. 3.14b). In case of photoionization schemes with increasing J-values, the variation in the transition strengths among the magnetic sublevels are small and all the magnetic sublevels contribute in the ionization process.

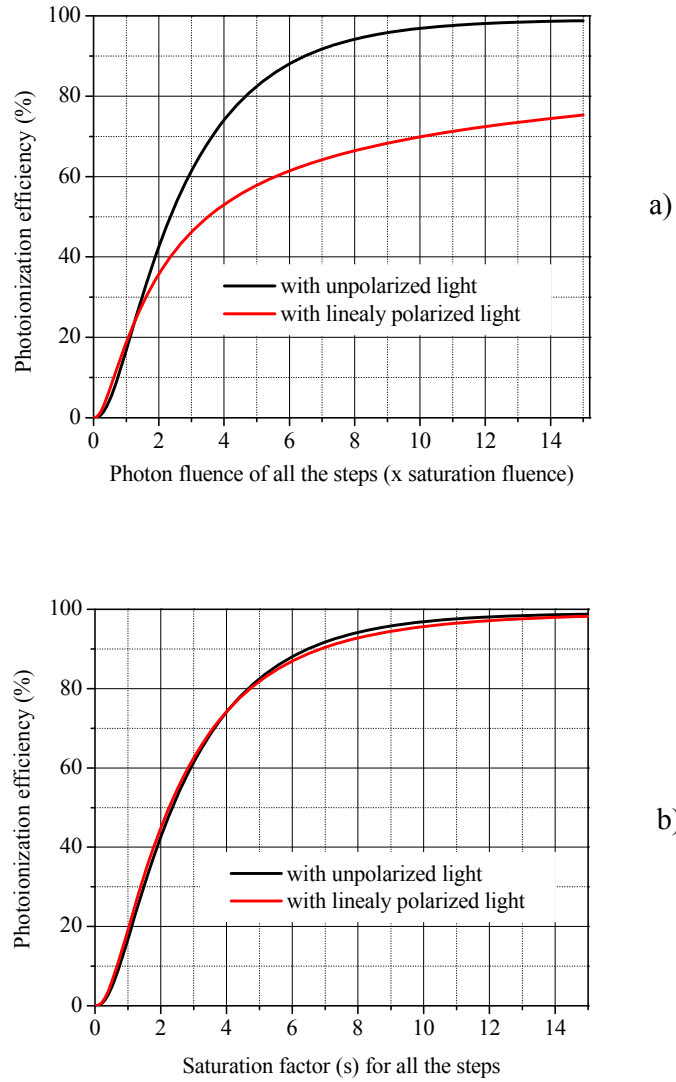


Fig. 3.14: Dependence of photoionization yield as a function of laser photon fluences in units of saturation photon fluence for J -sequences of a) $6 \rightarrow 6 \rightarrow 6 \rightarrow 6$ and b) $6 \rightarrow 7 \rightarrow 8 \rightarrow 9$. Here, photon fluences of all the lasers are varied simultaneously.

Chapter 4 - Determination of transition probabilities of atomic uranium by measuring radiative lifetimes and branching ratios using delayed photoionization method

4.1 Introduction

Radiative lifetime (τ), branching ratio (β) and transition probability (A) are important parameters of an atomic system. The details about these parameters are discussed in appendix 1-4. The accurate knowledge of these parameters in general, and transition probability or equivalently oscillator strength in particular is important in many areas of basic as well as applied sciences. In atomic physics, experimentally measured transition probability is used to test the theoretical model. Transition probability plays a key role in many areas of science such as, laser physics - to identify new laser materials, in astrophysics - to determine the abundance of elements in the solar system and in laser based applications like trace analysis of radioactive elements/isotopes and in laser isotope separation etc. Radiative lifetime in combination with branching ratio yields the information about transition probability.

In the three-step photoionization of uranium (Fig. 4.1), the atom in the ground level ($^5L_6^o$) or in the lowest metastable level ($^5K_5^o$) at 620.32 cm^{-1} is excited up in the ladder sequentially by first- and second-step lasers to one of the even-parity energy levels in the $15,000\text{--}19,000 \text{ cm}^{-1}$ region and the odd-parity energy levels in the $30,000\text{--}36,000 \text{ cm}^{-1}$ region, respectively, before it is finally photo-ionized by another laser. Therefore, the information on the spectroscopic parameters in these energy regions is prerequisite to identify an efficient three-step photoionization wavelength scheme for isotope selective photoionization process of uranium and its quantification. In a photoionization process, to achieve higher photoionization yield, transitions with higher transition probabilities or cross sections are

chosen. As already discussed, the ratio of the branching ratio and the radiative lifetime yield transition probability, so to achieve higher transition probability branching ratio of the

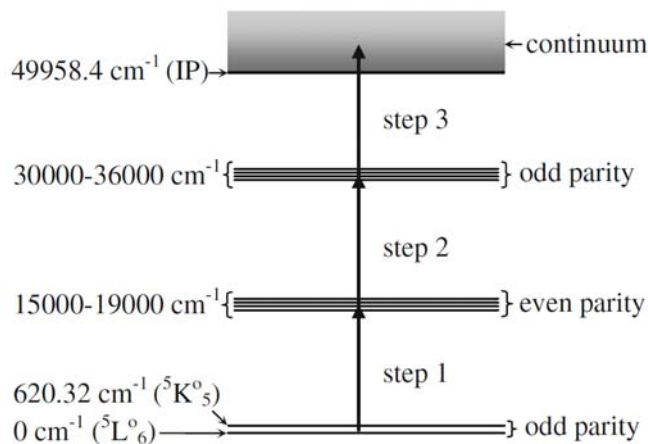


Fig. 4.1: Typical three-step photoionization pathway for atomic uranium using visible lasers

transition should be large and radiative lifetime of the upper level of the transition should be small. However, the excited atomic levels whose radiative lifetimes are small compared to the laser pulse width are not suitable because it will result in significant loss of excited atoms during the laser pulse due to spontaneous decay to different lower levels.

Conventionally, transition probabilities of atomic uranium are obtained either from the measurement of line strengths in the emission spectra acquired from arcs, sparks or discharge lamps or from the measurement of absolute absorption [6,111-116].

Corliss [6,111] have derived transition probabilities and oscillator strengths (f values) of 549 lines of atomic uranium by measuring relative emission intensities in an arc between copper electrodes to which uranium was added in the ratio of 1 atom to 1,000 atoms of copper. To derive the absolute oscillator strengths and transition probabilities from the relative emission intensities, they have equated the inverse of lifetime value of the atomic level at $27,887 \text{ cm}^{-1}$ measured by Klose et al. [117] to the sum of the oscillator strengths of two principal transitions at 358.488 and 462.023 nm originating from $27,887 \text{ cm}^{-1}$ level.

Voigt et al. [112] have measured relative gf values of 49 strong uranium ion (U II) lines and 21 strong atomic uranium (U I) lines in arc emission. The gf values of U I lines were placed on an absolute scale by employing radiative lifetime of $27,887 \text{ cm}^{-1}$ level of U I. This absolute scale was extended to the U II lifetime values by measuring the relative intensity of a U I and a U II line.

Palmer et al. [5] have proposed a method to calculate oscillator strength from the observed relative intensities (I) of 92,000 emission lines from the U-Ne hollow cathode discharge lamp using the following formula

$$gf = \frac{3.15 \cdot 10^{-14}}{e^{-3.5 \cdot 10^{-4} E_u}} I \lambda^2. \quad (4.1)$$

Where E_u is the energy of the upper level and λ is the transition wavelength in Angstroms. Also g is the degeneracy of the upper level. The expression for the line intensity

$$I = K \frac{gf}{\lambda^2} e^{-E_u/kT} \quad (4.2)$$

was used to derive the relation in equation (4.1). The proportionality constant K and temperature T of the discharge were measured using gf values of known transitions which were earlier reported by Corliss [111] and Klose et al.[118] Using similar methodology, Henrion et al. [113] have measured gf values of more than 370 lines of U I and U II.

Bieniewski et al. [114] have used furnace absorption method to determine oscillator strength of 497 transitions of U I by observing relative optical opacities of all the transitions in comparison to the strongest transition at 358.487 nm. Kapoor et al. [116] have measured relative transition probabilities of more than 20 U I transitions in the wavelength region 400 to 700 nm involving ground state and lowest metastable state using line absorption method in a U-Ne hollow cathode discharge lamp. These measurements were performed in a single hollow cathode discharge tube, which was used as a light source as well as absorption cell.

These relative measurements were placed on an absolute scale by using the previously measured

absolute gA values of $0 - 15,631.85 \text{ cm}^{-1}$ transition [119].

All these above mentioned classical methods yield the product of Nfl , where N , f , l represents the absolute number density of the emitting or absorbing atoms, the extent of the emitting or absorbing layer and oscillator strength of the transition. Since the absolute number density is often very difficult to determine accurately, the accurate measurement of the absolute transition probability or oscillator strength is rather difficult.

With the invention of the tunable lasers, the most commonly used method to determine the transition probabilities is based on the measurements of branching ratio and radiative lifetime (β - τ method) where β is obtained using either Fourier Transform Spectroscopy (FTS) or laser induced fluorescence (LIF) [120,121,122] and τ is measured independently either by delayed photoionization (pump-probe) or LIF technique [120,122]. The absolute transition probability is related to these two atomic parameters by a well known relation $A = \beta/\tau$, where β is the branching ratio of the desired transition and τ is the lifetime of the upper level. In FTS method complete understanding of the emission spectra is necessary for accurate measurement of absolute transition probability. In case of β measurement using LIF, one disadvantage is that large number of undetected infrared transitions, particularly in case of uranium may result in over estimation of transition probabilities[103,104]. The other laser based methods such as laser saturation of transition, Rabi frequency measurement and Autler Towns splitting etc. [103,123] are not significantly affected by these uncertainties, but put stringent requirements on the laser parameters such as spectral width and temporal profile of the laser pulse etc.

Carlson et al. [82] have developed an alternative method of measuring absolute transition probability based on the delayed photoionization technique which is not subjected

to these difficulties. Using this technique, they have measured branching ratios of uranium transitions at 436.21 and 439.36 nm wavelengths in the blue region of uranium spectrum and radiative lifetimes of the upper (excited) atomic levels of the transitions independently. Hackel et al. [119] have refined this method to accurately measure the transition probability of a uranium transition at 639.542 nm in the red region of uranium spectrum. Miyabe et al. [124], have exploited the same technique to measure the absolute transition probabilities of gadolinium. Bisson et al. [125] have extended this method further to measure excited level to excited level transition probability of cerium.

Measurements of radiative lifetimes of excited atomic levels of atomic uranium reported in the literature were mostly performed by observing exponential decay of the level population as a function of time. The resultant decay curve was fitted with exponential decay formula to extract the lifetime values. The basic measurement procedure can be divided into two steps: excitation of atoms by absorption of light photon (laser frequencies are tuned to the center frequency of the absorbing transitions) or collision with energetic electrons/ions and observation of fluorescence/light emission or delayed photoionization.

Klose et al.[117,118] have measured the lifetimes of 27,887 and 16,900 cm^{-1} levels of U I using electronic excitation and a method of delayed coincidence. The measured lifetimes of these two levels were 10.9 ± 0.8 ns and 205 ± 20 ns respectively. They have used pulsed beam of electrons (energy 100 eV) to excite the uranium atoms in an effusive atomic beam. Excitation of atoms by electron is a non selective process, thus it simultaneously populates large number of levels and hence there is a possibility of cascade of transitions. To avoid the cascade of transitions they have selected the desired emitted light using a monochromator. Using similar method Ramanujan et al.[126] have measured lifetimes of 16,900 and 19,885 cm^{-1} levels of atomic uranium. They have used energetic heavy ions to generate atomic vapor via sputtering and to excite the neutral atoms.

Using the lifetime of uranium atomic level at $27,887\text{ cm}^{-1}$ measured by Klose et al. [117], Corliss [111] have derived the oscillator strength from the observed relative emission intensities in arc formed between two copper electrodes. From the sum of the derived oscillator strengths, they have estimated the upper limits of the lifetimes of 65 levels.

Poulsen et al. [127] have measured lifetimes of 25 excited levels of U II in a collinear fast-beam of U II using modulated CW dye laser and delayed coincidence method.

Miron et al. [17] have measured lifetimes of 135 levels of U I (even-parity levels in the energy region $16,000\text{--}26,000\text{ cm}^{-1}$ and $49,600\text{--}49,900\text{ cm}^{-1}$, odd-parity levels in the energy region $32,000\text{--}34,850\text{ cm}^{-1}$) using stepwise excitation and fluorescence detection. They have used induction heated oven for generating atomic vapour. Argon buffer gas was used to confine the uranium vapors inside the oven. Monochromator was used to reduce the background noise and was set on a strong fluorescence transition from the upper level whose lifetime to be measured. Fluorescence signal was detected using fast PMT and the output of the PMT was digitized by a transient recorder. They have measured the radiative lifetime as a function of the argon pressure to extrapolate the measured data at zero argon pressure.

A large number of lifetime measurements were performed using delayed photoionization method. Janes et al. [80] have measured lifetimes of 6 even-parity levels in the energy region $22,000\text{--}24,000\text{ cm}^{-1}$ using N_2 laser pumped dye lasers in a two-step two-color photoionization process. Carlson et al. [81] have measured lifetimes of 12 odd-parity levels in the energy region $32,000\text{--}33,200\text{ cm}^{-1}$ using N_2 laser pumped dye lasers in a three-step three-color photoionization process. Carlson et al. [82] have measured radiative lifetimes of $22,918.55\text{ cm}^{-1}$ and $22,754.06\text{ cm}^{-1}$ levels. Hackel et al. [119] have measured lifetime of $15,631.85\text{ cm}^{-1}$ level. Das et al. [128] have measured lifetimes of 9 odd-parity levels in the energy region $34,000\text{--}35,000\text{ cm}^{-1}$. Despite these large numbers of studies the information on the radiative lifetimes of atomic uranium is scanty.

4.2 Present work on the measurement of radiative lifetimes and branching ratios

The measurements of radiative lifetimes and branching ratios of atomic uranium in the energy region $15,500\text{--}19,000\text{ cm}^{-1}$ are presented in this chapter. These measurements were carried out using three-step delayed photoionization technique. By combining these measurements, absolute transition probabilities of six transitions of uranium starting either from ground level ($^5L_6^o$) or from metastable level ($^5K_5^o$) at 620.32 cm^{-1} have been determined.

4.2.1 Experimental details

Fig. 4.2 shows the schematic diagram of the experimental set-up used in these studies. The details of the experimental set-up have been discussed in chapter 2. One of these three dye lasers was used as a pump laser and the other two were used as probe lasers. Temporal

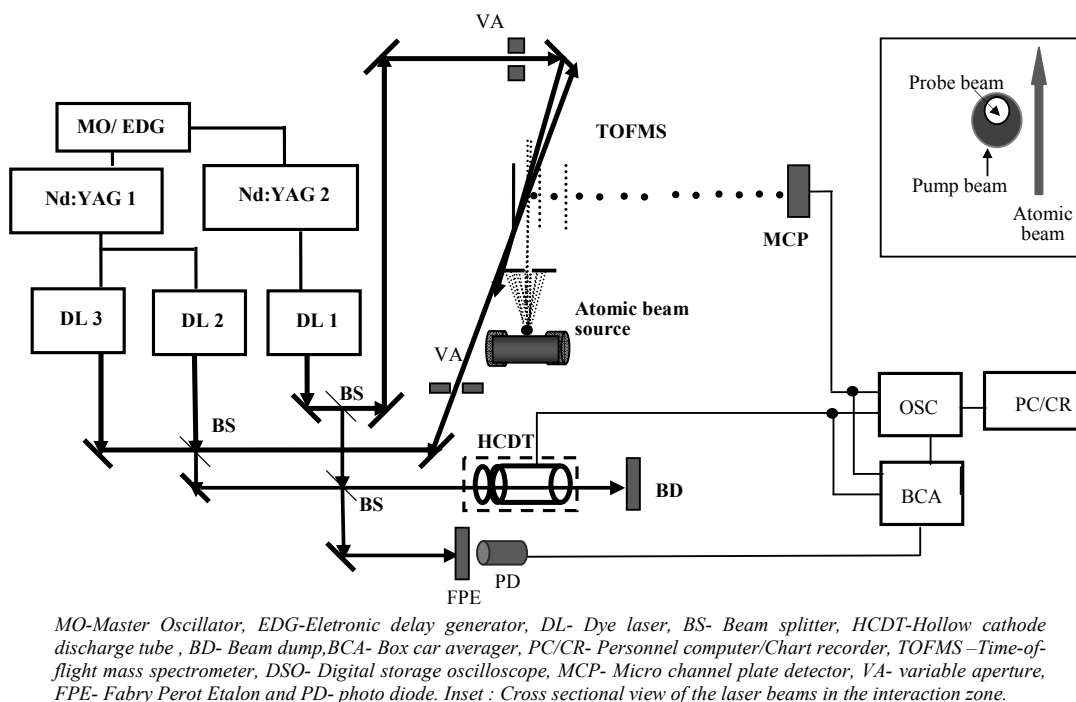


Fig. 4.2: Schematic of experimental set up.

sequencing of laser pulses from different lasers was achieved by using an electronic delay generator. The pump and probe lasers were apertured individually and spatially overlapped in the interaction zone by using beam steering optics. The spatially overlapped laser beams interact with the atomic beam in a cross configuration and the resultant photo-ions produced were extracted and introduced into the TOMF-MS by a dc electric field of ~ 120 V/cm, and finally detected by a micro channel plate (MCP) detector.

4.2.2 Results and discussions

4.2.2.1 Lifetime Measurement

Schematic of the photoionization pathway and time sequence of laser pulses are shown in as inset in Fig. 4.3. Radiative lifetime measurements were carried out using two pulsed dye laser systems whose pulse timing can be finely controlled to an accuracy of ± 1 ns. The first laser is used as a pump laser to excite the uranium atoms from ground or metastable levels to a level of interest in the energy region $15,500$ - $19,000$ cm^{-1} . The population in the excited level was monitored by ionizing the excited atoms by stepwise two-photon photoionization process, using the second dye laser (probe laser) at various time delays between the pump and probe lasers. For each lifetime measurement, about 12 data points were taken and each data point was obtained after taking an average of 64 laser pulses. To avoid the effects of excited atoms drifting out of the interaction volume due to atomic beam flow velocity, we have deliberately kept pump laser beam diameter (4 mm) more compared to probe laser diameter (2 mm). Further, the probe laser beam spot was kept down-stream of atomic beam as shown in Fig.4.2 to minimize the effect of excited atoms drifting out of interaction volume at large time delays. A typical population decay curve of uranium level at $15,631.85$ cm^{-1} is shown in Fig. 4.3. These measurements have yielded the radiative lifetime of 630 ± 30 ns for this level which is close to the value 607 ± 20 ns reported in the

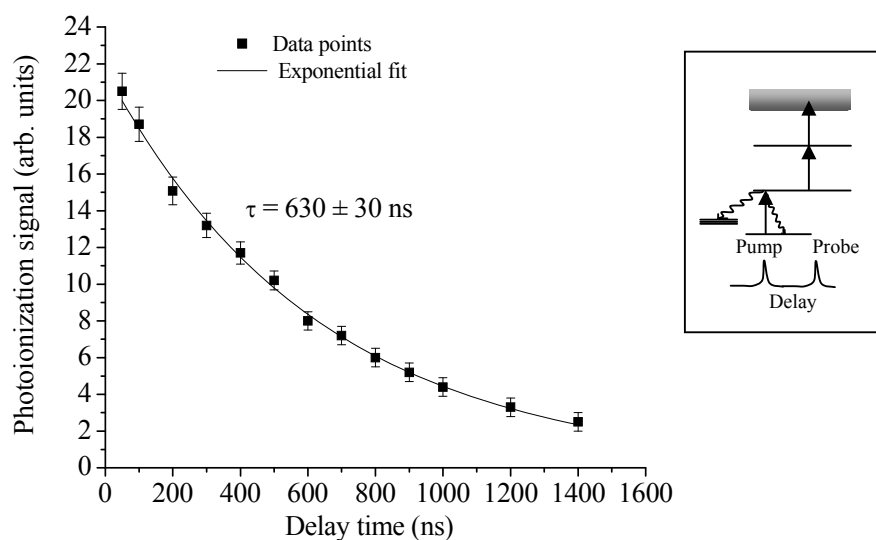


Fig. 4.3: Population decay curve of uranium atomic level at $15,631.85 \text{ cm}^{-1}$. The solid line is an exponential fit of the data. Inset: Schematic of excitation pathways for lifetime measurements.

literature [119]. The high resolution obtained in our TOFMS combined with that of delay generator has enabled us to make these measurements accurately. Employing the same technique, we have measured the radiative lifetimes of nine more even-parity levels of uranium in the energy region $15,500\text{--}19,000 \text{ cm}^{-1}$. The measured lifetime values along with reported ones are listed in Table 4.1. Most of the values are matching reasonably well with those reported in the literature with the exceptions of a few. Miron et al. [17] is one of the first groups who have done the most extensive work on lifetime measurements of uranium atomic levels. They have carried out the measurements in an argon buffer gas cell using LIF. Their values of lifetimes, particularly, of long lived levels are relatively on lower side as compared to our values. The atomic collisions in buffer gas cell could be the reason for shortening the radiative lifetime even though the values have been corrected by extrapolating to zero pressure. In this work, the lifetimes of five even-parity energy levels of atomic uranium have been measured for the first time.

Table 4.1: Measured values of radiative lifetime of even-parity excited levels of uranium

Energy level (cm ⁻¹)	Angular momentum (J)	Measured Lifetime τ (ns)	
		This work	From literature
15631.85 ^a	7 ^a	630 \pm 30	607 \pm 20 ^b , 594 ^f
15638.37 ^a	6 ^a	640 \pm 40	452 ^f
16121.93 ^a	4 ^a	275 \pm 12	
16505.77 ^a	6 ^a	585 \pm 30	451 ^f , 400 ^c , 330 \pm 10 ^e
16900.38 ^a	7 ^a	200 \pm 14	205 ^c , 200 ^d , 255 \pm 25 ^e , 270 ^f
17361.89 ^a	6 ^a	456 \pm 30	410 ^c , 390 \pm 50 ^e , 116 ^f
18185.99 ^a	4 ^a	1905 \pm 130	
18253.87 ^a	6 ^a	725 \pm 50	
18406.52 ^a	5 ^a	206 \pm 10	
18607.79 ^a	4 ^a	1260 \pm 80	

^a Blaise et al., 1976 [74].^b Hackel et al., 1978 [119].^c Miron et al., 1979 [17].^d Klose et al., 1977 [118].^e Carlson et al., 1976 [81].^f Arisawa et al., 1983 [61].

4.2.2.2 Branching Ratio measurement

Six transitions of uranium whose branching ratios are measured in the present studies are as shown in Fig. 4.4. The measurement of branching ratio was performed using three pulsed dye lasers. One dye laser was used as a pump, and the other two were used as a probe. Level schematic of excitation pathways for the pump and probe lasers to measure branching ratios by delayed photoionization method is shown in Fig. 4.5a. The uranium atoms from level 1 (0 or 620.32 cm⁻¹) were excited to level 2 by the pump laser which was in resonance to the transition between levels 1 and 2. The population in level 1 was probed via two-color three-photon photoionization process using two synchronized probe lasers. The resultant photoionization signal was recorded as a function of delay between the pump and the probe

lasers. Due to finite radiative lifetime of atoms in excited level (2), the excited atoms decay back to various lower levels including level 1. The population dynamics of level 1 and level 2 just after the laser pulse can be written as

$$\frac{dN_1}{dt} = \beta \frac{N_2}{\tau} \quad (4.3)$$

$$\frac{dN_2}{dt} = -\frac{N_2}{\tau} \quad (4.4)$$

The solution of equations 4.3 is

$$N_1(t) = N_1(0) + \beta N_2(0) \left[1 - \exp\left(-\frac{t}{\tau}\right) \right]. \quad (4.5)$$

where $N_1(0)$ and $N_2(0)$ are the populations in level 1 and level 2 respectively just after the pump laser pulse at $t = 0$. In the case of complete saturation and equal level degeneracies, $N_1(0) = N_2(0) = N_{10}/2$, where N_{10} is the population of level 1 just before the pump laser pulse.

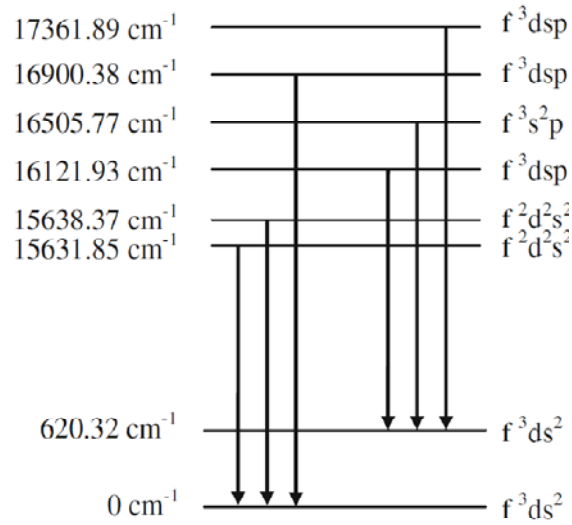


Fig. 4.4: Energy level diagram of the transitions whose branching ratios have been measured.

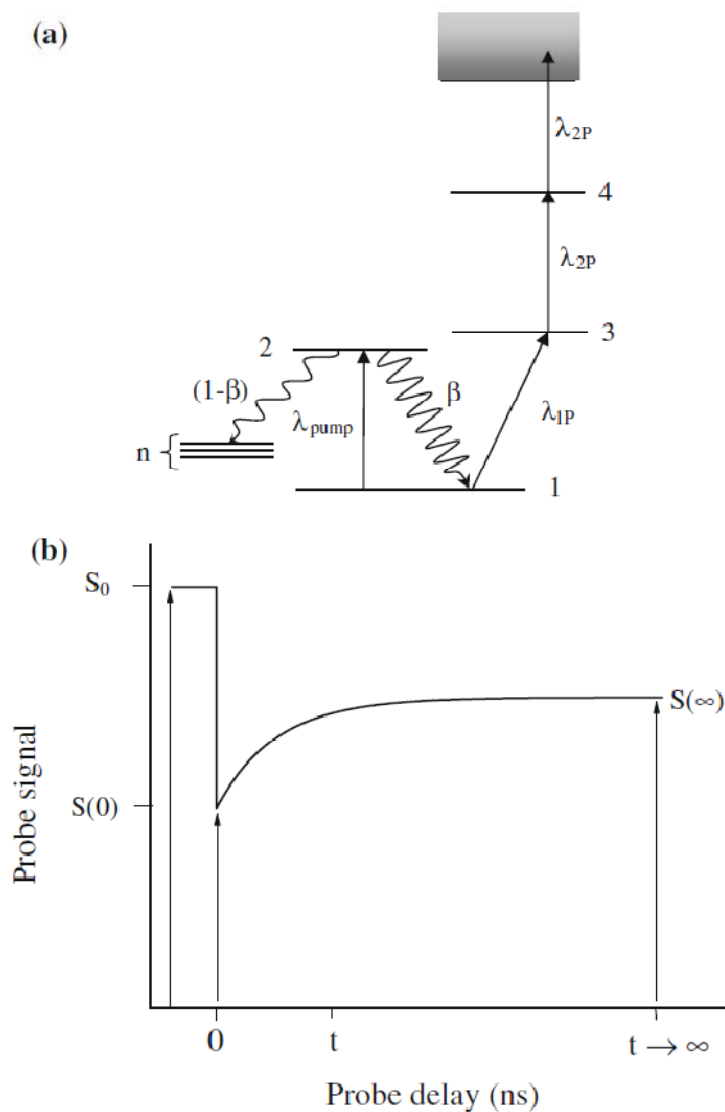


Fig. 4.5: a) Schematic of excitation pathways for the pump and probe lasers to measure the branching ratios. The pump laser λ_{pump} pulse excites the population from level 1 to level 2 of the transition whose branching ratio is to be determined and the laser pulses λ_{1P} plus $2 \lambda_{2P}$ generate probe signal. b) Representative probe signal versus time delay between the pump and the probe laser pulses.

The photoionization signal produced by probe lasers is directly proportional to population of level 1. Due to repopulation of the level 1 by spontaneous decay of the level 2, probe signal increases with time delay between the pump and the probe lasers. The delayed photoionization signal of the probe from level 1 is depicted in Fig. 4.5b, where S_0 represents the PI signal of probe laser in the absence of pump laser, $S(0)$ is the signal of the probe laser when both the pump and probe lasers are synchronous, i.e., at time $t = 0$ and $S(\infty)$ is the probe signal at infinite time delay between the pump and the probe lasers i.e. at $t \rightarrow \infty$. The branching ratio can then be written as $\beta = [S(\infty)-S(0)]/[S_0-S(0)]$, where $[S_0-S(0)]$ represents the depopulation of level 1 at time $t = 0$ and $[S(\infty)-S(0)]$ is the repopulation of the level 1 at time $t \rightarrow \infty$. Repopulation of level 1 due to radiative decay from level 2 is about 99.3 % at $t = 5\tau$, which is a good approximation for $t \rightarrow \infty$.

The experimental points on the repopulation curve for the branching ratio measurement of different uranium transitions are shown in Fig. 4.6. In these measurements, the pump laser wavelengths (λ_{pump}) tuned to the uranium transitions at 639.542 nm, 597.150 nm, 644.915 nm, 639.276 nm to excite the atomic population to the upper level at 15631.85 cm^{-1} , 17361.89 cm^{-1} , 16121.93 cm^{-1} , 15638.37 cm^{-1} respectively from the ground or metastable level. Due to finite lifetime of the excited level, its population decays back to various levels, including the starting ground or metastable level. From the figure it is clear that depending on the branching ratio repopulations are different. The population of the lower level was monitored via two-color three-photon photoionization technique using other two lasers. As an example, for 15,631.85 cm^{-1} transition, the first step probe laser wavelength (λ_{IP}) tuned in resonance to uranium transition 0-16,900.38 cm^{-1} at 591.54 nm excites the uranium atom from ground level to atomic level at 16900.38 cm^{-1} and second step probe laser tuned to the uranium transition 16,900.38 -34,523.36 cm^{-1} at 567.28 nm excites it further up in the ladder before it was ionized by another photon from the same laser.

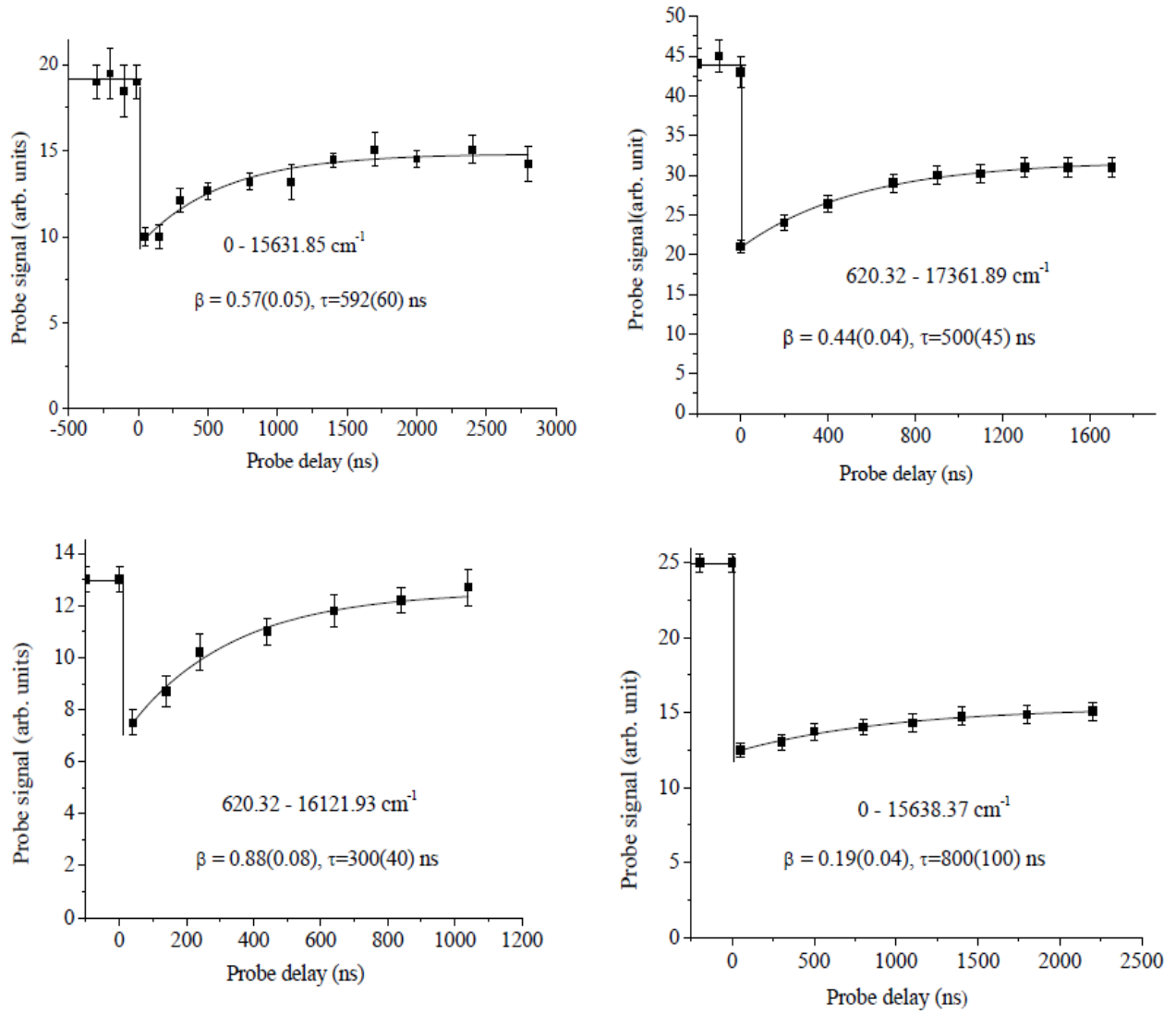


Fig. 4.6: Repopulation curves of ground level or metastable level at 620.3 cm^{-1} from the excited levels of the respective first step transitions of uranium. Solid line is a fit of the data using equation (4.5) for simultaneous measurement of β and τ .

Initially when pump and probe lasers are simultaneous, maximum depopulation of the ground level was observed. Thereafter repopulation of the lower level was monitored as function of the delay between the pump and probe lasers. The value of the branching ratio for the uranium transition at 639.542 nm was obtained by fitting the repopulation data using equation

(4.5), as shown in Fig. 4.6. The β value 0.57 (0.05) is matching very well with the measurement made by Hackel et al. [119]. Table 4.2 lists the branching ratios of various transitions measured in the present studies and the values reported in the literature. Branching ratios of five transitions are measured for the first time to our knowledge. Also listed in table 4.2 are the gA values of transitions obtained by combining the radiative lifetime and branching ratio, where g is the level degeneracy. Our values of transition probabilities are on slightly higher side as compared to those of Corliss [111]. They have made the measurements in an arc, where high density of vapour could result in lower values due to self absorption. This is further corroborated by the fact that our values are matching exceedingly well with those of Kapoor et al. [116] who have taken care of self absorption at the source in their measurements. In view of this, the gA values of the remaining three transitions as measured by Corliss [111] need to be corrected.

In these measurements following steps are taken to minimize the error:

- a) Error due to transit time effect (drift out of excited atoms from interaction volume) was minimized by using a larger pump laser beam compared to probe laser beam as shown in Fig 4.2. In our experimental conditions, the estimated drift out time was $\sim 5\mu\text{s}$ where as we have limited our measurements upto $3\mu\text{s}$.
- b) Error due to variation in laser intensity (spatial) was minimized by selecting the central part of the laser beams with uniform intensity.
- c) Probe laser wavelengths are chosen carefully so that it does not produce any two-color three-photon PI from the upper level of pump laser transition.
- d) Another potential source of error in the lifetime measurements could be due to the excitation of high-lying atomic levels via two-photon excitation for the laser intensities and line width used in these experiments. These can influence the lifetimes due to cascading effect. Since the lifetime values obtained through two independent

measurements (radiative decay and repopulation of lower level) had matched within our experimental errors, this possibility was ruled out.

Table 4.2: Measured values of branching ratio and gA values of uranium

Energy levels (cm^{-1})		Present work		Reported	
Lower	upper	β	gA value ($\times 10^6 \text{ sec}^{-1}$)	β	gA value ($\times 10^6 \text{ sec}^{-1}$)
0	15631.85	0.57 ± 0.05	13.6 ± 1.35	0.586 ± 0.05^a	$14.5 \pm 1.25^a, 11^b$
0	15638.37	0.19 ± 0.04	3.9 ± 0.86		3.5^b
620.32	16121.93	0.88 ± 0.08	28.8 ± 2.90		$16^b, 32^c$
620.32	16505.77	0.15 ± 0.04	3.3 ± 0.90		3^b
0	16900.38	0.63 ± 0.06	47.3 ± 5.59		$53.8^c, 35^b, 68^d$
620.32	17361.89	0.44 ± 0.04	12.5 ± 1.40		9.8^b

^a Hackel et al., 1978 [119].

^b Corliss, 1976 [111].

^c Kapoor et al., 1989 [116].

^d Klose et al., 1977 [118].

- e) Effect of pulse to pulse variation in laser intensity was minimized by taking average of 64 laser pulses at each data point.
- f) Due to polarization of laser beams, pumping process and subsequent spontaneous decay will preferentially populate the specific magnetic sub level (m_j). This could be another cause of error in the measurement of branching ratios, particularly in the case of elements with low J-values such as zirconium, samarium etc . However, in the case of uranium atom, J-values are generally high; hence this was not expected to affect the measurements significantly [125]. Moreover, we have chosen the photoionization scheme for the probe where J-values of the atomic levels involved in the scheme are either equal or in increasing order as we move up in the ladder, thus minimizing any error due to this effect.

However, there is a statistical error of 4-7% in the lifetime measurements whereas in case of branching ratio measurements, the error is in the range of 5-10% for high β values which could be upto 30% for weak transitions. Poor signal-to-noise (S/N) ratio, particularly in the case of weak transitions, could be the reason for large error in the branching ratio and also the limiting factor in these measurements. In addition to the reasons discussed above, drift in oven temperature and subsequent change in atoms number density during measurements could be another cause of error.

Chapter 5 - Measurement of excited-level to excited-level transition probabilities and photoionization cross sections of excited levels of atomic uranium by saturation method

5.1 Introduction

In the previous chapter, absolute transition probabilities of many first step transitions of uranium have been determined by measuring branching ratios and radiative lifetimes using delayed photoionization method. Although ($\beta - \tau$) method gives accurate values of transition probability, using delayed photoionization technique, but it is difficult to implement this method for transitions with small branching ratios ($\beta < 0.1$) and for second step (excited-level to excited-level) transitions due to the finite lifetime of the lower level which results in poor signal to noise ratio. As an alternate to $\beta - \tau$ method, transition saturation method has been used to measure the photoexcitation cross sections of various excited-level to excited-level transitions of photoionization schemes using multimode broadband lasers. In this method photoionization yield is studied as a function of laser energy density/photon fluence of the particular transition and the resultant saturation curve is fitted with the solution of the population rate equations to extract the cross section values. Moreover, the saturation method is the most suitable method to measure the photoionization cross section of the excited levels. Measurement of photoionization cross section of excited levels using saturation of transition method was pioneered by Ambartsumian et al. [34]. Using this method, they have determined the photoionization cross sections for $6^2P_{1/2}$ and $6^2P_{3/2}$ levels of atomic Rubidium. Subsequently, this method has been extensively applied to measure photoionization cross sections of many elements [39,42,43,46,52].

Solartz et al. [129] have first reported the measurement of the photoexcitation cross sections of three first step transitions of atomic uranium by performing laser absorption

studies using single mode laser. The initial work on photoionization cross section of uranium was carried out by Janes et al. [80]. They have measured the photoionization cross section of $23,432.79 \text{ cm}^{-1}$ level of atomic uranium at 360.9 nm of ionizing laser wavelength (line width $\sim 0.06 \text{ nm}$) by comparing the photoionization yield with the ion yield produced by a 1.4 keV electron beam of known flux. The measured value of the photoionization cross section was $2 \times 10^{-17} \text{ cm}^2$ for laser line width equal to the line width of the autoionizing resonances. Greenland et al. [130] have measured the photoionization cross section of $2.2 \times 10^{-15} \text{ cm}^2$ of an autoionizing transition $34,659 \rightarrow 50,422 \text{ cm}^{-1}$ by comparing experimental and theoretical photoionization efficiencies. Experimentally, the ionization efficiency was determined by measuring ion collection current and number density of the neutral uranium atom in ground state using absorption spectroscopy. They have also measured the transition probability of uranium transition $17,361.89 \rightarrow 34,659.21 \text{ cm}^{-1}$ using Autler Townes splitting method.

Carlson et al. [81] have measured the excited level to excited level (second step transition) photoexcitation cross section of 10 transitions of atomic uranium starting from $16,505 \text{ cm}^{-1}$ level using transition saturation method. In these measurements, the wavelengths of the chosen second step transitions were such that there was no two-color three-photon photoionization. Therefore, the four-level system could be simplified into a two level system by temporally separated the laser pulses. They have measured the photon fluence by saturating the first step transition $0 \rightarrow 16,505 \text{ cm}^{-1}$ whose cross section value was previously measured by laser absorption studies [129]. Cross sections of all the other transitions were normalized with respect to this first step transition. Ruster et al. [52] have reported the photoexcitation and photoionization cross section of a three-step three-color photoionization scheme $0 \rightarrow 16,900.38 \rightarrow 34,599.66 \rightarrow 50,411.8 \text{ cm}^{-1}$. The measured cross section values are $9.0 \times 10^{-14} \text{ cm}^2$, $2.9 \times 10^{-14} \text{ cm}^2$, $3.5 \times 10^{-15} \text{ cm}^2$ for the first, second and the third step transitions respectively. The line widths of the dye lasers were 3.5 GHz , 3.7 GHz and 1.2 GHz for the

first, second and the third step lasers respectively. Avril et al. [104] and Petit et al. [103] have discussed different laser based methods for measurement of photoexcitation and photoionization cross sections. They have measured transition probability of $16,900.38 \rightarrow 34,659.21 \text{ cm}^{-1}$ transition using both transition saturation and β - τ method. The measured gA value of this transition is $1.12 \times 10^8 \text{ s}^{-1}$. This is one of the strongest second step transitions of atomic uranium in the visible wavelength region. Shah et al. [45] have measured the photoionization cross section of $33801.05 \rightarrow 50701.6 \text{ cm}^{-1}$ transition using single-color three-photon photoionization and simultaneous fluorescence detection from the first excited level. Apart from these few studies, the information on the photoexcitation/photoionization cross sections of atomic uranium is scanty, thus generation of new data is required.

5.2 Present work on photoexcitation and photoionization cross section measurements using saturation method

Measurement of cross sections of the first- and the third-step transitions of atomic uranium using saturation method in a three-step photoionization process is straight forward, since these transitions can be considered as a two-level system by temporally separating the laser pulses. However, in the case of second-step transitions, two types of situations such as $(\lambda_1 + 2\lambda_2 < \text{I.P.})$ and $(\lambda_1 + 2\lambda_2 > \text{I.P.})$ may occur (Fig. 5.1a and b), where λ_1 and λ_2 are the first and second step laser wavelength in energy units and IP is the first ionization potential. In the former case measurement is also straight forward due to absence of two-color photoionization pathways. In the latter case, second excited level population is ionized by both the second and delayed third laser. Saturation of the second step transition may be modified in presence of direct two-color three-photon photoionization process. In such cases, detailed investigation of photoexcitation dynamics is necessary to obtain second step cross sections/transition

probabilities. From the measured photoexcitation cross sections transition probabilities have been determined and compared with the values reported in the literature.

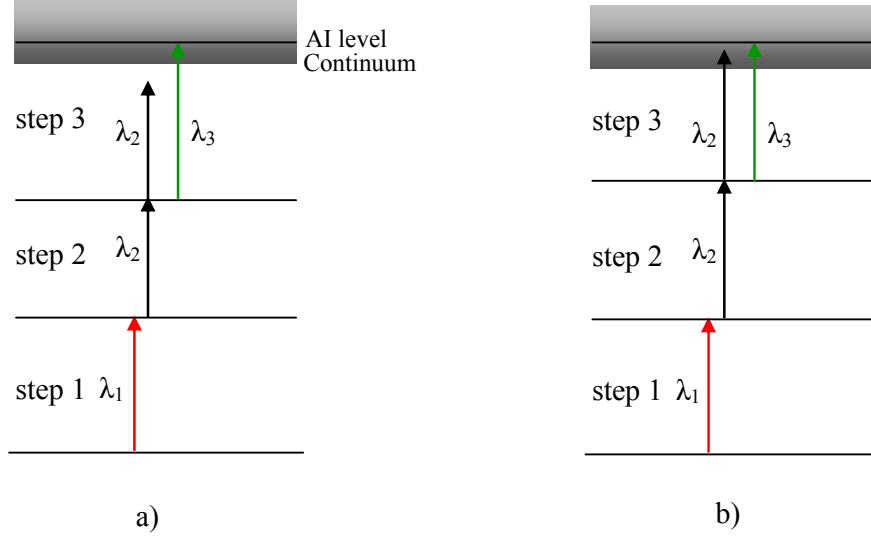


Fig. 5.1: Three-color three-step photoionization pathways: a) without two-color three-photon photoionization, b) with two-color three-photon photoionization. AI level: autoionizing level.

5.2.1 Experimental details

The experimental set-up used in these measurements has been discussed in detail in chapter 2. To ensure stepwise excitation and to simplify the excitation dynamics, a temporal delay of about 12 ns between the first and the second dye lasers was introduced optically, and a delay of about 40 ns between the second and the third lasers was introduced by using an electronic delay generator. A PIN type fast photo diode was used to monitor the delay among the laser pulses. Spatial overlap among the laser beams was realized using beam splitter and beam steering optics. A part of the combined laser beams was made to pass through the U-Ne HCDT and coupled with wavelength meter for the purpose of laser wavelength measurement. The uniform part of the combined laser beams was selected using a fixed aperture of diameter 4 mm (for some measurements long focal length lens of focal length 4 m and 6 m was used to

increase the laser energy density and fixed aperture of 2 mm diameter was used to select the central part of the combined laser beam) and made to interact with the atomic beam perpendicularly and the resultant photoions produced were extracted, accelerated and introduced in the TOF-MS using DC electric fields of 120 V/cm. The fixed aperture which was placed just in front of the window of the TOF-MS was used for calculation of laser photon fluence in the laser atom interaction region.

In these measurements, the first-step dye laser (DL₁) wavelength (λ_1) is acquired by tuning its wavelength across the transition of interest and observing the optogalvanic signal in HCDT. The second-step dye laser (DL₂) wavelength (λ_2) was tuned to the respective second-step transition by observing the two-color three-photon ($\lambda_1+2\lambda_2$) photoionization signal in the TOF-MS. The third-step dye laser (DL₃) wavelength (λ_3) was tuned to the respective third-step transition by observing the delayed three-color three-photon ($\lambda_1+\lambda_2+\lambda_3$) photoionization signal in the TOF-MS. Energy density of the desired laser, corresponding to the transition whose cross section to be measured, was varied by inserting different neutral density filters (Thorlabs) in the path of the laser beam, perpendicularly while keeping the energy densities of the remaining two lasers fixed. Laser energies corresponding to other two transitions were kept above saturation to minimize the effect of pulse to pulse energy fluctuation. All the measurements were carried out on the major isotopes (²³⁸U) only. Transmission of the neutral density filter was verified before each measurement. Wavelengths of all the steps were simultaneously verified using wavelength meter. The spectral width (FWHM) of the lasers used in these studies was measured by observing the Fabry Perot Etalon transmission fringes using diverging laser beam at a fixed wavelength.

5.2.2 Results and discussion

5.2.2.1 Measurement of photoexcitation cross section of the first step transition

As a test case photoexcitation cross section of $0 - 16,900.38 \text{ cm}^{-1}$ transition has been measured by saturation method, whose cross-section value is known in the literature. The purpose of this measurement is to standardize the technique which has been used for the measurement of photoexcitation/photoionization cross section of second- and third-step transitions. Schematic of the photoionization scheme and lasers pulse time sequence is shown in Fig. 5.2. First laser (pump) at 591.538 nm wavelength was used to excite the uranium atoms from ground levels to $16,900.38 \text{ cm}^{-1}$ level. Population in the excited level was monitored by ionizing the excited atoms via two-color three-photon photoionization process, using the second dye laser (probe) at 567.284 nm . During the measurement, all other experimental parameters like second laser power, oven temperature, extraction and acceleration voltages, and detector voltage were kept constant. Thus, the two-color three-photon photoionization signal was linearly proportional to the 1st excited level population.

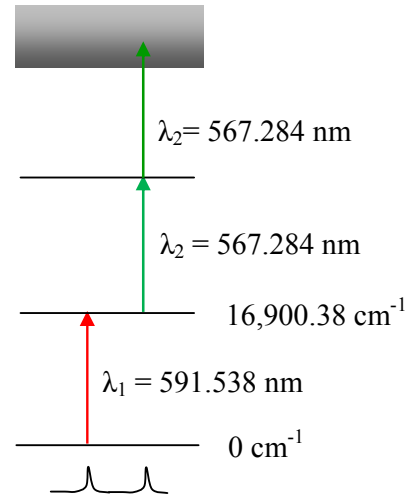


Fig. 5.2: Photoionization pathways for measurement of cross section of $0 \rightarrow 16,900.38 \text{ cm}^{-1}$ transition of atomic uranium

Fig. 5.3 shows the variation of PI signal as a function of first step laser photon fluence (number of photons per unit area per pulse) for $0 \rightarrow 16,900.38 \text{ cm}^{-1}$ transition. The laser photon fluence (ϕ) was determined using the following relation

$$\phi = \frac{P}{f(\pi D^2)(\hbar\omega)} \quad (5.1)$$

Where P is the laser power, f is the pulse repetition rate; D is the beam diameter and $\hbar\omega$ is the photon energy. The resultant saturation curve was fitted with the solution of a two-level population rate equations i.e.

$$S = S_0(1 - e^{-2\phi\sigma}) \quad (5.2)$$

to obtain the cross section values. Here, S represents experimentally measured photoionization signal intensity at any photon fluence and S_0 represents maximum photoionization signal intensity. S and S_0 are proportional to the total number of atoms available in the first excited level. The details of the population rate equation model are discussed in chapter 3. The details about the photoexcitation cross section are discussed in appendix 5. The measured cross section of this transition is $(1.6 \pm 0.4) \times 10^{-13} \text{ cm}^2$. From the

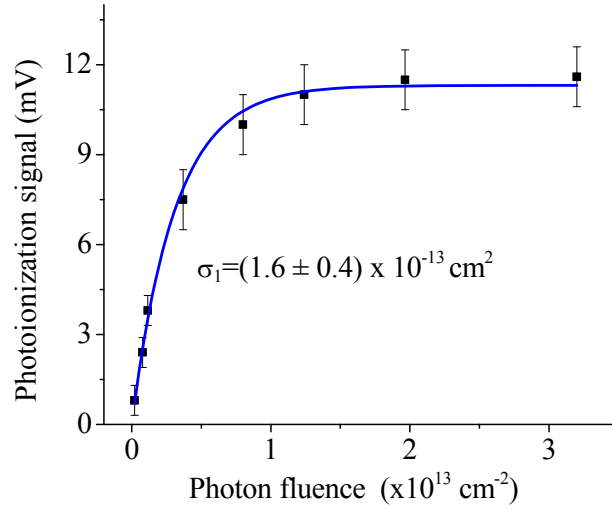


Fig. 5.3: Photoionization yield as a function of the first step laser photon fluence for $0 - 16,900.38 \text{ cm}^{-1}$ transition of atomic uranium.

measured cross section value transition probability was determined using equation (3.1c) and compared with the value obtained from β - τ method along with literature values and listed in Table 5.1. It is found that the value obtained from saturation method is slightly lower compared to the value obtained from the β - τ method, however it matches very well with

Ruster et al.[52] who has also measured using saturation method. Slight lower value could be due to difficulty in realizing uniform laser beam, uncertainties in the measurement of cross sectional area of the laser beam, laser energy, laser linewidth and non-consideration of the effects of laser polarization.

Table 5.1: Photoexcitation cross sections (σ_1) and transition probability (A) of $0 \rightarrow 16,900.38 \text{ cm}^{-1}$ transition of atomic uranium for 2.4 GHz laser line width.

Present work			Reported
Saturation method		β - τ method	$A(\times 10^6 \text{ sec}^{-1})$
$\sigma_1 (\times 10^{-13} \text{ cm}^2)$	$gA(\times 10^6 \text{ sec}^{-1})$	$A(\times 10^6 \text{ sec}^{-1})$	
1.6 ± 0.4	35.9 ± 9	47.3 ± 5.6	$53.8^a, 35^b, 68^c, 34.5^d$

^a Kapoor et al.[116],

^b Corliss [111],

^c Klose et al.[118],

^d Ruster et al. [52]

In ideal case, realizing two level systems is extremely difficult for a complex atom like uranium. But when (i) laser pulses are separated in time, (ii) negligible spontaneous decay during the laser atom interaction time, then it can be considered as two level systems for excitation by unpolarized light. As discussed previously in chapter 3, when polarized light (e.g. linear) is used transition between magnetic sublevels may need to be considered. There are $2J+1$ magnetic sublevels ($m_j = -J$ to J) corresponding to a level with total angular momentum J . So, there will be $2J+1$ number of independent two-level systems corresponding to a transition. In chapter 3, effects of laser polarization on the saturation curve have already been discussed. Even though there was a significant difference in the photoionization yield for polarized and unpolarized light but curvature of the saturation curves were observed similar that means state of laser polarization does not affect the measurement of photoexcitation/photoionization cross section significantly. However, there could be some

error due to laser polarization effects which are smaller compared to other sources of errors. Statistical uncertainties of about $\pm 25\%$ were observed over repeated measurement. The major contributions to these variations were from the measurement of laser power, laser beam diameter in the interaction region, spatial overlap among the laser beams and change in the atomic number density due to drift in the oven temperature ($\pm 2^{\circ}\text{C}$) etc. during these measurements. Since the measured value matches well with the literature values, the systematic uncertainties are expected to be much lesser compared to these statistical uncertainties. For measurement purpose we have not considered the polarization effects as J-values of all the final levels of various photoionization pathways were not known. While determining the transition probability from the measured cross section value, level degeneracies were not considered, since total number of magnetic sublevels participating in the transition is same for both the levels with photoexcitation by linearly polarized laser.

5.2.2.2 Measurement of Photoionization cross sections of excited levels (third step transitions) of uranium

Schematic of the photoionization pathway and lasers pulse time sequence for measurement of photoionization cross sections of various third step transitions is shown in Fig. 5.4. First and second laser (pump) was used to excite the uranium atoms from ground levels to a second excited level. Population in the second excited level was monitored by ionizing it through a delayed third step laser. The details of the study of autoionizing levels will be presented in chapter 6 and chapter 7.

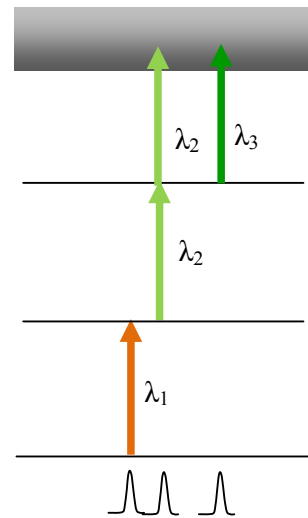


Fig. 5.4: Photoionization pathways for measurement of photoionization cross sections of excited levels

Fig. 5.5 shows the variation of PI signal as a function of third-step laser photon fluence (ϕ_i) for $34,675.91 - 52,371.6 \text{ cm}^{-1}$ transition. The resultant saturation curve was fitted with the solution of an open two-level population rate equations i.e.

$$S = S_0(1 - e^{-\phi_i \sigma_i}) \quad (5.3)$$

to obtain the photoionization cross section values (σ_i). Here S represents experimentally measured photoionization signal intensity at any photon fluence and S_0 represents maximum photoionization signal intensity. S and S_0 are proportional to the total number of atoms available in the second excited level. The details of the population rate equation model are discussed in chapter 3. Here it is assumed that atoms excited into an autoionizing level

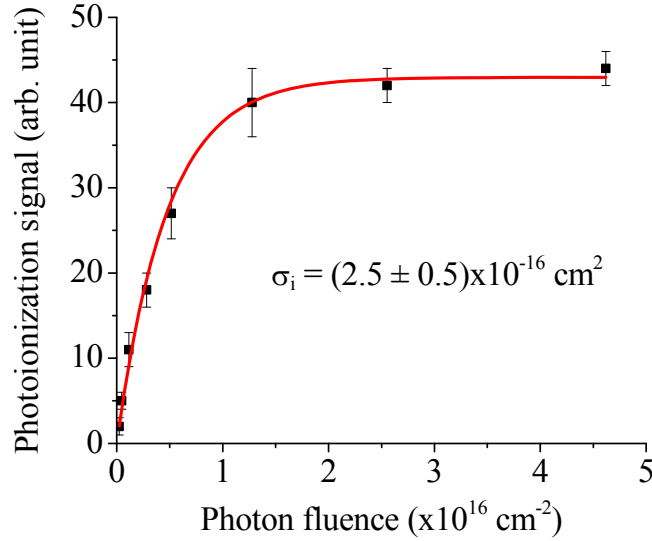


Fig. 5.5: Dependence of delayed three-color photoionization signal intensity on the third-step laser photon fluence for $34,675.91 - 52,371.6 \text{ cm}^{-1}$ transition at $\lambda_3=564.95 \text{ nm}$. The third-step laser energy at the maximum of photon fluence $4.5 \times 10^{16} \text{ photon/cm}^2$, is 16 mJ/cm^2 . The solid line represents the least square fit of the equation 5.3.

spontaneously decays to a free electron and an ion. The measured values of the photoionization cross sections from five different second excited levels are listed in Table 5.2. These cross section values can be used for estimation of photoionization cross section of other autoionizing transitions originating from the same second excited level.

Table 5.2: Photoionization cross-sections (σ_i) of odd-parity high-lying levels of atomic uranium.

Wavelength λ_3 (nm)	Autoionizing transition		Photoionization cross section $\sigma_i (\times 10^{-16} \text{cm}^2)$
	Lower level (cm^{-1})	Upper level (cm^{-1})	
640.27	34,659.21 ^a	50,273.2 ^c	3.4 ± 0.6
641.25	34,659.21 ^a	50,249.4 ^c	3.3 ± 0.7
640.69	34,578.25 ^b	50,182.2 ^c	12.0 ± 3.0
563.76	33,801.03 ^b	51,534.2 ^d	3.5 ± 0.7
568.40	34,578.25 ^b	52,166.5 ^e	7.5 ± 2.0
567.98	34,578.25 ^b	52,179.6 ^e	3.1 ± 0.7
567.06	34,578.25 ^b	52,208.1 ^e	3.0 ± 0.6
567.48	34,599.54 ^b	52,216.4 ^e	2.3 ± 0.4
561.92	34,599.54 ^b	52,390.7 ^e	1.4 ± 0.3
564.95	34,675.91 ^b	52,371.6 ^e	2.5 ± 0.4
560.91	34,675.91 ^b	52,499.2 ^e	1.7 ± 0.4

^a Blaise and Radziemski[74].^b Miyabe et al.[83]^c Mandal et al.[131]^d Manohar et al.[94]^e Mandal et al. [132]

5.2.2.3 Measurement of excited-level-to-excited-level transition probabilities and photoionization cross sections

In a three-step photoionization (PI) process, as shown in Fig.5.1b, where two-color as well as three-color photoionization is possible, both two-color and delayed three-color three-photon PI signals are present together. The magnitude of the delayed three-color PI signal represents the atomic population remaining in the second-excited level after the two-color photoionization. Assuming that the first-step transition is completely saturated, the magnitude of the two-color photoionization signal depends on the second-step excitation rate ($\sigma_2 \Phi_2$) and third-step ionization rate ($\sigma_{2i} \Phi_2$), where σ_2 is the photoexcitation cross-section of the second step transition, σ_{2i} is the photoionization cross-section from the second-excited level at λ_2 , and

Φ_2 is the photon flux of the second step laser. Depending on the strength of σ_{2i} and Φ_2 , there will be loss of atoms from the second excited level due to two-color photoionization. Thus, the population in the second-excited level will be different as compared to the case when there is no connection to the continuum as shown in Fig.5.1a. Therefore, the apparent saturation observed in this case is not the real one and the second-step cross-section values obtained by fitting the data with the solutions of the two-level rate equations may not be accurate. Moreover, a two-color three-photon photoionization process in which the last-step transition coincidentally terminates into an autoionizing level is generally stronger than that in which the last transition ends in continuum. Hence, in such cases this effect may manifest even more strongly. In a multi-electron system like uranium, which has six optically active electrons in its outermost shell, this possibility is definitely very high. This may result in the depletion of the second-excited level population at higher laser fluence which, in turn, affects the measurement of σ_2 significantly. In this section, investigations of photoexcitation dynamics in a three-step photoionization process in an atomic beam of uranium coupled to a high resolution time-of-flight mass spectrometer using two-color three-photon and delayed three-color three-photon PI signals are presented. Both PI signals were analyzed using population rate equation model for the three-step PI process to determine the excited-level-to-excited-level cross-section (σ_2) and the photoionization cross-section (σ_{2i}) at second-step wavelength (λ_2) simultaneously.

5.2.2.3 a) Numerical analysis using population rate equations

The population rate equations for three-step photoionization process with unpolarized and spatially uniform laser light as depicted in Fig. 5.6, accounting for both two- and three-color photoexcitation and photoionization by lasers can be written as

$$\frac{dn_0}{dt} = - \left(n_0 - \frac{g_0}{g_1} n_1 \right) W_1(t) + A_{10} n_1 \quad (5.4a)$$

$$\frac{dn_1}{dt} = \left(n_0 - \frac{g_0}{g_1} n_1 \right) W_1(t) - \left(n_1 - \frac{g_1}{g_2} n_2 \right) W_2(t) + A_{21} n_2 - \frac{n_1}{\tau_1} \quad (5.4b)$$

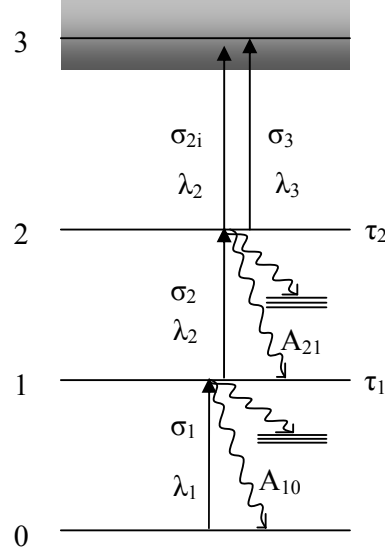


Fig. 5.6: Schematic diagram of a three-step photoionization with various excitation and decay processes.

$$\frac{dn_2}{dt} = \left(n_1 - \frac{g_1}{g_2} n_2 \right) W_2(t) - \frac{n_2}{\tau_2} - W_{2i}(t) n_2 - W_3(t) n_2 \quad (5.4c)$$

$$\frac{dn_i}{dt} = W_{2i}(t) n_2 + W_3(t) n_2 \quad (5.4d)$$

It should be noted that these population rate equations are similar to the equations discussed in chapter 3. Here one additional term is added to consider the two-color three-photon photoionization process. In these equations, n_m , g_m , τ_m represents the atomic population, statistical weight and radiative lifetime of m^{th} level. $A_{m,m-1}$ is the transition probability between m^{th} and $m-1^{\text{th}}$ levels. $W_m(t)$ represents photoexcitation or photoionization rate of the m^{th} step transition which is written as

$$W_m(t) = \frac{\sigma_m \phi_m}{\Delta t_{mL}} f_{mL}(t) \quad (5.5)$$

where σ_m is the average cross-section of the m^{th} step transition, ϕ_m is the photon fluence i.e. number of photons per unit area per pulse, Δt_{mL} is the temporal width (FWHM) of the m^{th} step laser and $f_{mL}(t)$ is the Gaussian temporal profile of the m^{th} step laser given by

$$f_{1L}(t) = \frac{2(\ln(2))^{1/2}}{\pi^{1/2}} \exp \left\{ - \left(\frac{t-t_0}{\Delta t_{1L}} \right)^2 2(\ln(2))^{1/2} \right\} \quad 5.6a$$

$$f_{2L}(t) = \frac{2(\ln(2))^{1/2}}{\pi^{1/2}} \exp \left\{ - \left(\frac{t-(t_0 + D_{12})}{\Delta t_{2L}} \right)^2 2(\ln(2))^{1/2} \right\} \quad 5.6b$$

$$f_{3L}(t) = \frac{2(\ln(2))^{1/2}}{\pi^{1/2}} \exp \left\{ - \left(\frac{t-(t_0 + D_{12} + D_{23})}{\Delta t_{3L}} \right)^2 2(\ln(2))^{1/2} \right\} \quad 5.6c$$

Here, t_0 is the time corresponding to the peak photon flux of the first laser pulse. D_{12} and D_{23} are the delays between lasers 1 & 2 and 2 & 3, respectively.

In order to study the effects of various σ_{2i} on the measurement of σ_2 , we have solved the coupled differential equations (5.4a) to (5.4d) numerically using fourth order Runge-Kutta method. In these calculations we have assumed $\sigma_1 = 1 \times 10^{-14} \text{ cm}^2$, $\sigma_2 = 1 \times 10^{-15} \text{ cm}^2$, $\sigma_3 = 1 \times 10^{-16} \text{ cm}^2$, $\tau_1 = 200 \text{ ns}$, $\tau_2 = 200 \text{ ns}$, $\Delta t_L = 5 \text{ ns}$, $D_{12} = 12 \text{ ns}$, $D_{23} = 42 \text{ ns}$, $g_0 = g_1 = g_2$. We have also assumed that the photon fluence of the first- and the third-step lasers are high enough to saturate the respective transitions thoroughly. The photoionization efficiencies for both two- and three-color photoionization pathways calculated as a function of the second-step laser fluence (ϕ_2), for the values of $\sigma_{2i} = 0, 0.01\sigma_2, 0.1\sigma_2, 0.2\sigma_2, 0.5\sigma_2$ and σ_2 , are shown in Fig. 5.7a & b. Fig. 5.7b shows the changes in the second level population as probed by delayed three-color photoionization after two-color photoionization has taken place. For $\sigma_{2i} \leq 0.01\sigma_2$, the change in the saturation of the transition is nominal, but for $\sigma_{2i} \sim \sigma_2$, the changes are significant.

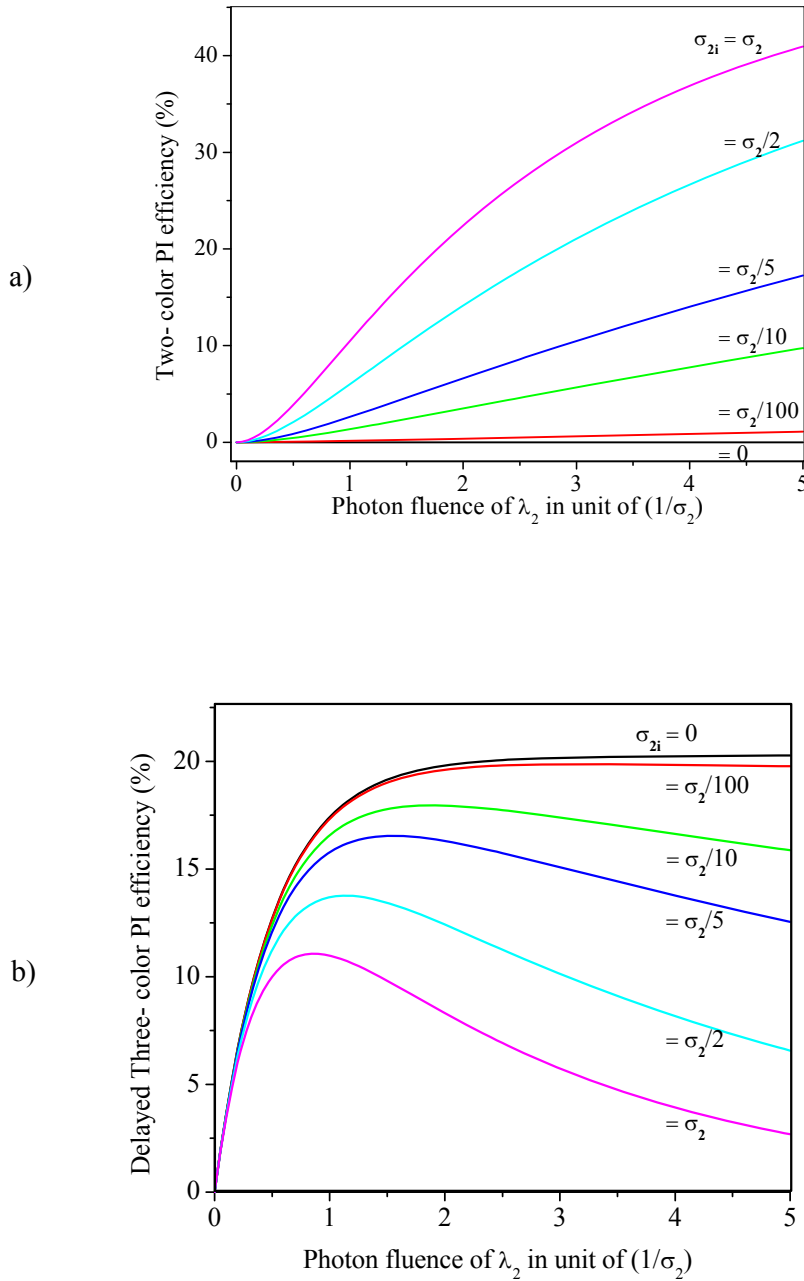


Fig. 5.7: Theoretical dependence of (a) two-color and (b) delayed three-color three-photon photoionization (PI) efficiency on the second-step laser photon fluence for different values of photoionization cross-section (σ_{2i}) at λ_2 , while keeping other parameters constant.

5.2.2.3 b) Simultaneous determination of second and third step cross section at λ_2

Seven two-color three-photon features based on two first-step transitions $0 \rightarrow 16,900.38 \text{ cm}^{-1}$ and $620.32 \rightarrow 17,361.89 \text{ cm}^{-1}$ at laser wavelengths 591.538 and 597.150 nm,

respectively have been chosen for investigations. To probe the second-excited level population, suitable third-step transition terminating into an autoionization level was identified by recording three-color spectra for each second-step transition. A TOF spectrum of U^+ produced by two-color and

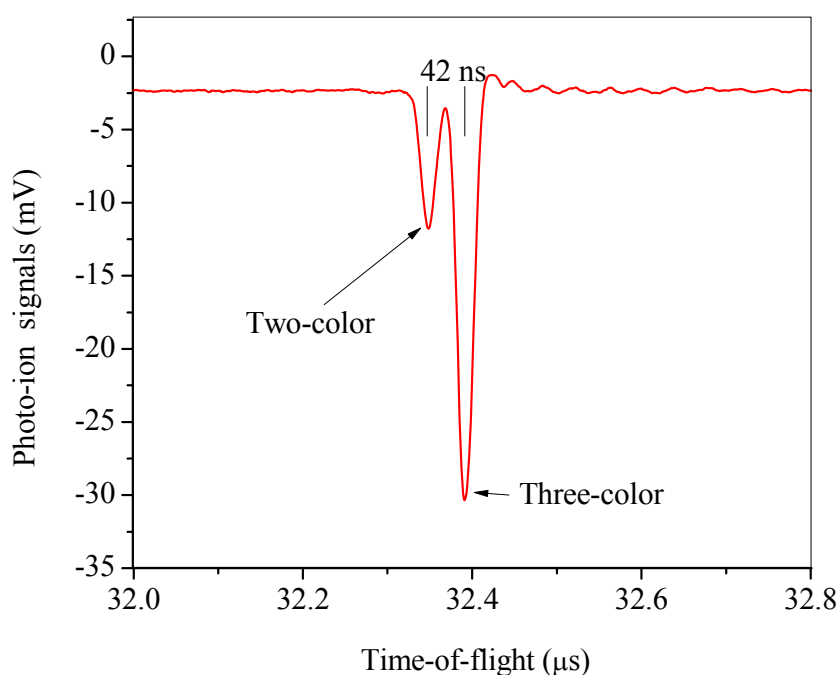


Fig. 5.8: Typical time-resolved time-of-flight spectrum of two-color and delayed three-color photoionization of uranium produced via three-step photoionization scheme $620.32 \text{ cm}^{-1} \rightarrow 17,361.89 \text{ cm}^{-1} \rightarrow 34,994.99 \text{ cm}^{-1} \rightarrow 52,558.9 \text{ cm}^{-1}$ by fixing the first-, second- and third-step laser wavelengths at 597.15 nm, 566.96 nm and 569.19 nm corresponding to the respective transitions.

delayed three-color three-photon photoionization processes via three-step photoionization scheme $620.32 \text{ cm}^{-1} \rightarrow 17,361.89 \text{ cm}^{-1} \rightarrow 34,994.99 \text{ cm}^{-1} \rightarrow 52,558.9 \text{ cm}^{-1}$ of uranium terminating into an autoionization level at $52,558.9 \text{ cm}^{-1}$, is shown in Fig. 5.8. Since all the lasers used in this experiment are tuned to the transitions of the major isotope, ^{238}U , combined with the low abundance (0.7%) of ^{235}U in natural uranium, no signature of ^{235}U is observed in the TOF spectrum. In this photoionization scheme, the first-, second- and third-

step laser wavelengths were tuned to 597.15 nm, 566.96 nm and 569.19 nm corresponding to respective transitions. We have studied the dependence of both two-color and delayed three-color photoionization signals simultaneously as a function of the second-step laser photon fluence while the photon fluence of other two lasers was kept constant. Observed dependence of these signals on the photon fluence is shown in Fig.5.9. The first- and third-step laser pulse energies densities $100 \mu\text{J}/\text{cm}^2$ and $15 \text{ mJ}/\text{cm}^2$ were high enough to saturate the respective transitions. In these measurements, each data point was obtained after averaging over 128 laser pulses. The figure shows a slight drooping in the delayed three-color signal. The drooping starts at the second-step laser fluence where the two-color signal appears. It is shown latter that depletion in the second-excited level population has become significant when the experiment was repeated at high photon fluence.

To incorporate the effect of temporal delays between the pulsed lasers in the photoionization yield calculations, the radiative lifetimes of the levels involved in the process need to be known. Radiative lifetimes of the first excited levels at $16,900.38 \text{ cm}^{-1}$ and $17,361.89 \text{ cm}^{-1}$, used in these studies are 200 ± 14 and 456 ± 30 ns respectively [110]. The lifetimes of the second-step excited levels are measured by employing the pump-probe technique [81]. To measure the lifetimes of the odd-parity high-lying levels, two-color photoexcitation followed by time-resolved delayed three-color photoionization was employed. The delayed third-step dye laser, DL₃, probes only the population of the second excited level which was ensured by the disappearance of the photoionization signal on blocking second step laser. The three-color photoionization signal observed at different delays was fitted using the exponential decay

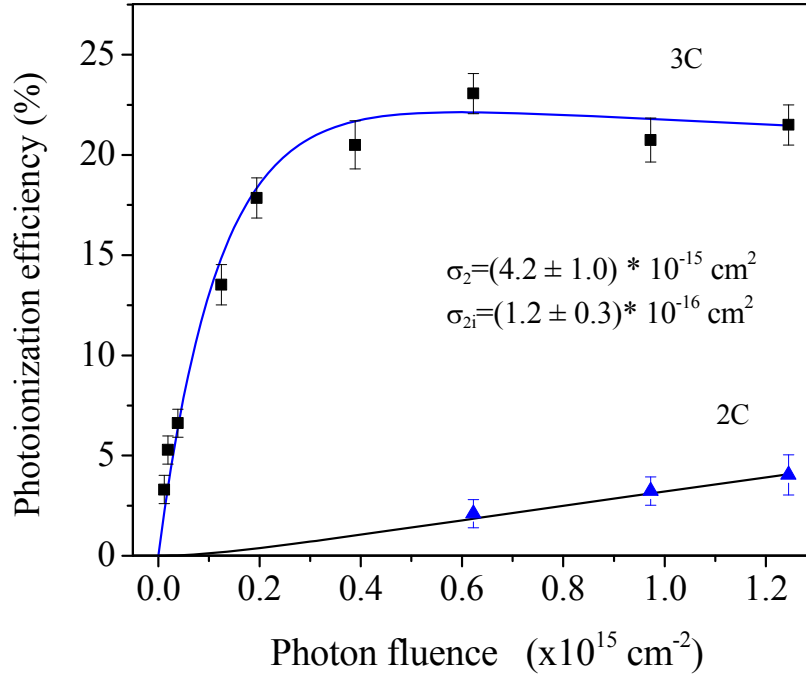


Fig. 5.9: Dependence of two-color and delayed three-color photoionization efficiency on the second-step laser photon fluence for a chosen transition $17,361.89 \text{ cm}^{-1} \rightarrow 34,994.99 \text{ cm}^{-1}$ at $\lambda_2 = 566.96 \text{ nm}$. The 2^{nd} step laser energy at the maximum of photon fluence $1.2 \times 10^{15} \text{ photon/cm}^2$, is 0.44 mJ/cm^2 . The solid line represents the calculated photoionization yields.

formula, $S(t) = S(0) \exp(-t/\tau)$, where $S(t)$ is the three-color delayed photoionization signal at delay time t , $S(0)$ is the three-color photoionization signal at zero delay and τ is the radiative lifetime of the level concerned. To avoid optical pumping effect during the laser pulse the lifetime data having time delay more than 12 ns was considered for fitting. The measured values of the lifetimes of these levels along with the reported values [17] are listed in Table 5.3.

The second-step photoexcitation cross-section (σ_2) and photoionization cross-section (σ_{2i}) were simultaneously determined by comparing the normalized experimental data points presented in Fig. 5.9 with the calculated photoionization yields of both the pathways with σ_2 and σ_{2i} as variable parameters. The normalization was done by equating maximum

Table 5.3: Radiative lifetimes of odd-parity excited levels of uranium.

Energy levels (cm^{-1})	Radiative lifetimes (ns)	
	Present work	Reported[17]
34599.54	50 ± 5	58
34659.18	25 ± 2	23
34994.99	740 ± 60	--
35004.97	233 ± 21	--
35018.01	555 ± 60	--
35036.91	188 ± 14	--
35046.07	286 ± 25	--

Table 5.4: Measured values of excited-level-to-excited-level photoexcitation (σ_2) and photoionization (σ_{2i}) cross-sections for a given laser line width of 2.4 GHz.

Wavelength λ_2 (nm)	Transition	σ_2 (10^{-14} cm^2)	Transition probability (10^5 sec^{-1})		σ_{2i} (10^{-17} cm^2)
			This work	Reported	
564.84	$16900.38 \text{ cm}^{-1} - 34599.54 \text{ cm}^{-1}$	5 ± 1.1	9.47 ± 2.1	8.5^a	1 ± 0.24
562.95	$16900.38 \text{ cm}^{-1} - 34659.18 \text{ cm}^{-1}$	26 ± 7	49.6 ± 13.4	$74.7^{b,c}$	0.85 ± 0.23
566.96	$17361.89 \text{ cm}^{-1} - 34994.99 \text{ cm}^{-1}$	0.42 ± 0.1	0.79 ± 0.19	--	12 ± 3
566.64	$17361.89 \text{ cm}^{-1} - 35004.97 \text{ cm}^{-1}$	0.5 ± 0.1	0.94 ± 0.19	--	0.95 ± 0.22
566.22	$17361.89 \text{ cm}^{-1} - 35018.01 \text{ cm}^{-1}$	0.1 ± 0.03	0.19 ± 0.06	--	1.8 ± 0.6
565.61	$17361.89 \text{ cm}^{-1} - 35036.91 \text{ cm}^{-1}$	0.28 ± 0.07	0.53 ± 0.13	--	2.7 ± 0.7
565.32	$17361.89 \text{ cm}^{-1} - 35046.07 \text{ cm}^{-1}$	0.23 ± 0.06	0.44 ± 0.11	--	1.6 ± 0.43

a Ruster et al. 1989 [52]

b Petit et al. 2002 [103]

c Uncertainty in the measurement $\geq \pm 30 \%$

photoionization signal to the maximum of the calculated photoionization yield. The values of σ_2 and σ_{2i} for which the nature of theoretical curves for both the signals resembles closely with the experimental curves are taken as the excited-level-to-excited-level photoexcitation and photoionization cross-sections, respectively for the given scheme. The cross-sections values thus obtained are listed in Table 5.4 along with the reported values. The transition probabilities listed in the table are obtained from the measured values of the photoexcitation

cross-sections using equation (3.1c). Our values of transition probabilities at 562.95 and 564.84 nm match reasonably well with the reported values in the literature. The uncertainties of about $\pm 25\%$ in the measured values are basically statistical variations occurred over repeated measurements. However, due to relatively weak two-color photoionization signals, the uncertainties in the measurements of σ_{2i} are on the higher side.

5.2.2.3 c) Investigation of two-color three-photon photoionization spectra

As mentioned before, the strength of a two-color feature in the spectra depends on the second-step excitation rate ($\sigma_2\Phi_2$) and third-step ionization rate ($\sigma_{2i}\Phi_2$). Since σ_2 is the

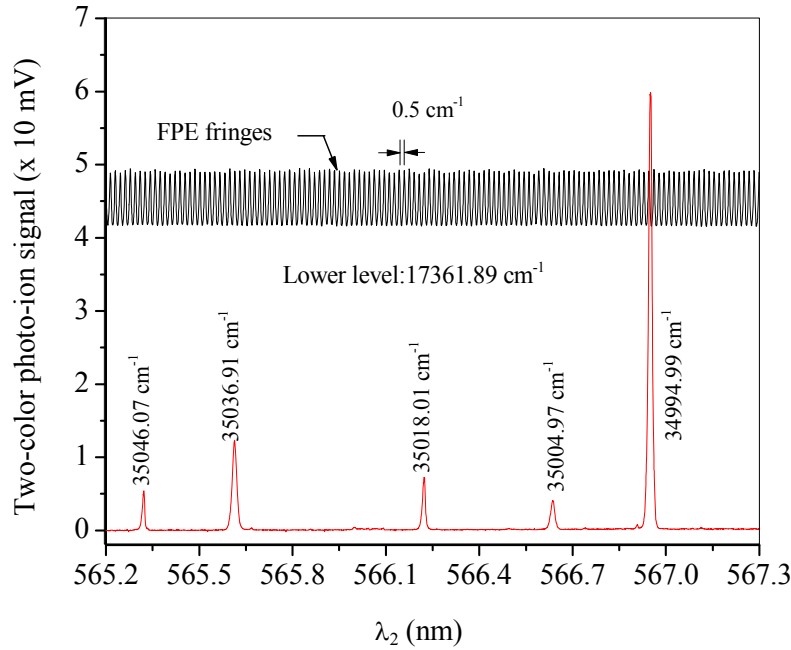


Fig. 5.10: Two-color three-photon photoionization spectrum of uranium recorded along with FP etalon fringes for first-step laser wavelength, λ_1 , fixed at 597.15 nm, corresponding to uranium transition $620.32 \rightarrow 17361.89 \text{ cm}^{-1}$ and second-step laser wavelength, λ_2 , scanned from 565.2 to 567.3 nm.

cross-section of a transition between the two bound levels, its value is generally larger than the third-step cross-section σ_{2i} . Therefore, in a two-color spectrum the second-step transition usually gets saturated at a moderate laser power and the magnitude of two-color

photoionization signal generally reflects the strength of σ_{2i} . A two-color three-photon photoionization spectrum based on the first-step transition $620.32 \rightarrow 17,361.89 \text{ cm}^{-1}$ has been recorded by scanning the second-step laser wavelength (λ_2) from 565.2 nm to 567.3 nm, as

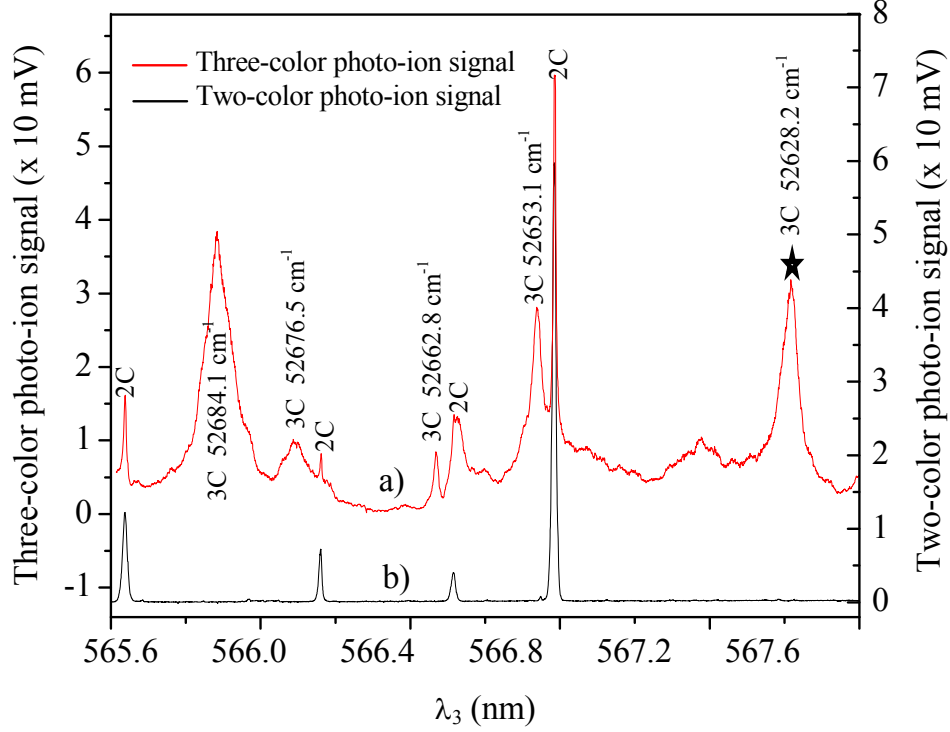


Fig. 5.11: a) Three-color photoionization spectrum of uranium obtained by fixing first- and second-step lasers wavelengths at 597.15 and 566.22 nm corresponding to the respective transitions $620.32 \rightarrow 17361.89 \text{ cm}^{-1}$ and $17361.89 \text{ cm}^{-1} \rightarrow 35018.01 \text{ cm}^{-1}$ and scanning the third laser wavelength, λ_3 , from 565.57 nm to 567.9 nm. b) repeat of (a) with second laser blocked.

shown in Fig. 5.10. Among the five known two-color features observed in the spectrum, the feature corresponding to the second-step transition $17,361.89 \text{ cm}^{-1} \rightarrow 34,994.99 \text{ cm}^{-1}$ at $\lambda_2 = 566.96 \text{ nm}$ is the strongest. The most probable reason could be that the third-step transition $34,994.99 \text{ cm}^{-1} \rightarrow \text{U}^+$ at the second-step laser wavelength is terminating into an autoionization level. The existence of the autoionization level at $52,628.2 \text{ cm}^{-1}$ was verified experimentally by recording three-color spectra from another nearby second-step excited level at $35,018.01 \text{ cm}^{-1}$ by scanning the wavelength of the third-step laser in the same energy region. The three-

color spectrum is shown in Fig. 5.11. Three-color feature at $\lambda_3 = 567.69$ nm, marked with asterisk, represents the autoionization level at $52,628.2$ cm^{-1} .

5.2.2.3 d) Observation of depletion of population in the second excited level due to two-color three-photon photoionization

It is expected from Fig. 5.7b that there is a possibility of the depletion of second excited level population due to two-color photoionization. In the present investigations of

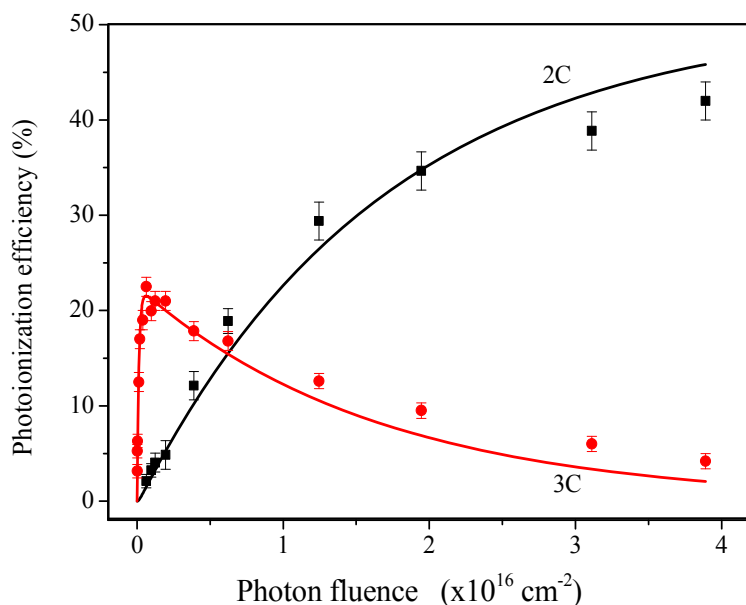


Fig. 5.12: Repeat of Fig. 5.9 at higher photon fluence to verify depletion of population of the second-excited level through two-color three-photon photoionization process as shown in Fig. 5.7b. The pulsed energy of the 2nd laser at the maximum of photon fluence is 13.64 mJ/cm^2 . The solid line represents the calculated photoionization yields.

two-color photoionization features, since most of the σ_{2i} 's measured are relatively very poor in comparison to σ_2 , thus it was necessary to perform experiments at much higher photon fluence of λ_2 to observe a significant depletion in the second-excited level population. A three-color three-step photoionization scheme from the seven schemes used in these studies was chosen and dependence of two-color and delayed three-color photoionization of uranium was studied simultaneously at higher photon fluence of λ_2 . As shown in Fig. 5.12, the expected depletion in the second-excited level population due to two-color photoionization is

observed and the experimental data is matching reasonably well with the photoionization yield calculated using the measured values of σ_2 and σ_{2i} at $\lambda_2 = 566.96$ nm, thus validating the model used in these studies.

Chapter 6 -Three-color photoionization spectroscopy of atomic uranium: Determination of energy values and total angular momenta of even-parity autoionizing levels

6.1 Introduction

Study of autoionizing levels and their total angular momenta is important to understand the complex atomic structure of multi-electron system, in basic research [28,32,68,133,134] and more importantly in applied research, to identify efficient ionization pathways for elemental and isotopic ultra-trace analysis [52,135] and isotope selective photoionization processes [26,70,104] using resonance ionization spectroscopy (RIS). Since bound-to-bound transitions are generally strong, the photoionization pathways involving a resonant final-step transition terminating into an autoionizing (AI) level are preferred over those terminating into continuum [67,68]. Thus, autoionization in the final step transition enhances the efficiency of multi-step ionization process. Multi-step RIS, employing narrow-band pulsed or CW tunable lasers, has played a pivotal role in unraveling wealth of information on autoionizing levels (levels above the ionization limit) which are not accessible by conventional spectroscopic techniques.

Apart from transitions strength, the total angular momentum (J) of a bound atomic level, in general and that of an AI level, in particular, is another important atomic parameter which dictates the photoionization (PI) yield in a multi-step photoionization process. Therefore, information of the J -value of AI level, particularly, when polarized laser light is used in the photoionization process, is a must as it decides the participation of number of magnetic sublevels in the process and the transition strength between the lower and upper magnetic sublevels.

6.1.1 Origin of autoionizing levels

Autoionizing levels are bound atomic levels whose energy lies above the first ionization potential. So these states are embedded in the continuum. Such levels usually arise when an inner electron of a multi-electron atom or minimum two valence electrons are simultaneously excited. Since the atom has continuum states above the first ionization limit, an atom excited to AI level spontaneously ionizes to an ion and a free electron. Ion goes to its lower ionic levels and excess energy is carried away by the free electron. The photoionization through autoionizing level may be viewed through the following steps



where the autoionizing state X^{**} of an element X corresponds to a temporally bound or quasi resonant state of the compound system ($e^- + X^+$). Autoionizing states may also manifest during collision of ion with the electron having right kinetic energy or through the electron bombardment of neutral atom. Thus, autoionizing states can be realized through the absorption of photon by a multi-electron atom or collision with energetic ion or electron.

Origin of autoionizing levels can be understood by comparing the excited states of hydrogen and helium atom [136]. In the case of hydrogen atom a single electron moves in the coulomb field of the nucleus, the discrete energy levels are classified in terms of various quantum numbers n (principal quantum number), l (orbital angular momentum quantum number) and m (magnetic quantum number) reaching to the ionization limit as n approaches infinity. Above the ionization limit there is only a smooth structure less continuum i.e. the electron can assume energies from a continuous range. However the picture becomes very different in case of multi-electron systems. In multi-electron atoms, atoms can have discrete bound states even above the ionization limit. This point can be understood with the simple example of helium. Helium atom has a ground state configuration of $1s^2$. The single electron excited state configurations of He can form the series $1sns, 1snp$ etc. converging to the first

ionization limit. At the first ionizing limit, He ionizes to form a He^+ ion with the ground state configuration $1s$ and free electron. Excited states of He can also form configuration series like $2sns$, $2snp$ etc. reaching to a series limit which lies above the first limit. These are doubly excited states and combined energy of two electrons lie above the first ionization limit. These states are known as autoionizing states. Due to the presence of these autoionizing states in multi-electron atom, one observes sharp resonances, superimposed on the smooth continuum absorption spectra.

6.1.2 Decay of autoionizing levels

Autoionizing states can decay either through radiation less transition to a continuum state of the same energy or through radiative decay to the lower level [137,138]. In case of radiation less transition, the final continuum state consists of a free electron and an atomic ion in either the ground or an excited level. The rapid autoionization process reduces the lifetime of the discrete level which restricts the observation of radiative decay from the autoionizing levels. The probability of decay increases with an increase in the coupling of the autoionization level and the continuum level. AI levels are generally very short lived and have lifetimes of $< \text{ps}$ [26]. Due to this short lifetime, linewidths of AI resonances are broad. When the difference of total angular momentum between the AI level and the lower ionic levels is more, the ejecting electron sees a centrifugal potential barrier which reduces the decay rate and thus increases the lifetime. Due to this centrifugal potential barrier effect, it is possible to observe autoionizing levels with ns lifetime. The increase in lifetime leads to narrow spectral width of the autoionizing resonances. AI resonances with linewidths $< 5 \text{ MHz}$ has been discovered in atomic gadolinium and uranium [32,68,97,139]. Lifetime of the autoionizing level can be determined from the observed linewidth of the AI resonance.

Spontaneous ionization of AI state occurs mainly due to Coulomb interaction between excited electrons. In the autoionization process total angular momenta and parity is conserved

i.e. continuum state must be of the same parity as that of AI state. Additional selection rules for the spontaneous decay via Coulomb interaction under L-S coupling scheme are $\Delta L = 0$ and $\Delta S = 0$ i.e. there should not be any change of total orbital and spin angular momentum [138]. In absence of continuum states with suitable spin angular momentum compared to the AI state, the atom cannot decay through Coulomb interaction. These states are metastable states against autoionization. These states can decay through either radiative processes or through slow autoionization via magnetic interaction. These states can also be metastable against radiation decay and can have lifetime of tens of microseconds [137,138].

6.1.3 Strength of autoionizing resonance

Due to discrete nature of the AI levels, excitation cross sections of autoionizing transitions are very high compared to the transition terminating into the continuum. Photoionization cross section of atoms terminating into continuum are generally in the range of 10^{-17} to 10^{-19} cm^2 [42,110,46,140]. Photoionization cross section better than 10^{-15} cm^2 has been reported by many researchers [52,141,142] using multimode pulsed lasers. The AI transitions with photoionization cross section $\sim 10^{-12} \text{ cm}^2$ has also been identified [68] in a highly collimated atomic beam using diode laser. Thus it is possible to enhance the photoionization yield by two to five orders of magnitude by using autoionizing transition. Photoionization of excited level through autoionizing level is a two step process i) photoexcitation to autoionizing level and ii) autoionization of AI level. Strong AI resonances with narrow linewidths are desired for efficient and isotope selective photoionization processes.

6.1.4 Shapes of the autoionizing resonances

The shapes of the autoionizing resonances is decided by the interference of the probability amplitudes of AI transitions with that of the continuum transitions and the

resultant shape become asymmetric, in general, which can be described according to Fano profile [143] as

$$\sigma(\epsilon) = \sigma_a \left[\frac{(q + \epsilon)}{(1 + \epsilon^2)} \right]^2 + \sigma_b \quad (6.1)$$

Here $\epsilon = 2(E - E_r)/\Gamma$ represents the departure of photon energy (E) from the resonance energy (E_r) in units of half-width ($\Gamma/2$) of the line. Also, $\sigma(\epsilon)$ represents the absorption cross section at photon energy E . The numerical index q decides the shape of the resonance. This parameter also infers the strength of the AI transition in comparison to continuum transition. Finally, σ_a and σ_b represent the two portion of the continuum cross sections that do and do not interact with the discrete AI state. When the cross section of the AI transition is very large compared to continuum transition, the shape becomes symmetric.

6.1.5 Valence and Rydberg autoionizing levels

Depending on the principal quantum number of the autoionizing levels, it can be divided into valence and Rydberg autoionizing levels. Valence autoionizing levels are characterized by low principal quantum number which arises due to simultaneous excitation of two-electrons. The interaction between the electrons is generally strong and the lifetimes of valence autoionization states are small. In case of Rydberg autoionizing levels one of the orbital electrons goes into a high n -state leaving behind the ionic core in an excited state. The wave function of such a high n -electron is concentrated outside the ionic core and there is minimum overlap with the core. Since the perturbation of the electron orbit by the core is very small, such states have relatively longer life-times of the order of a nanosecond. Correspondingly the widths of these states are also quite narrow.

Rydberg AI levels, owing to its high electric polarizability, are very sensitive to external electric fields. In presence of electric field, Rydberg level may split, shift and vanish completely [144]. Electric field can also induce transitions which are forbidden according to electric dipole selection rules [144].

6.2 Literature survey on the study of autoionizing levels and angular momenta of atomic uranium

6.2.1 Autoionizing levels

With the presence of six optically active electrons in the outer shell, the uranium atom is a prototype of a multi-electron system. Owing to its application in nuclear industry, AI levels of uranium have been a subject of many spectroscopic investigations over the last four decades. Janes et al.[80] have first studied the photoionization spectra of atomic uranium near the first ionization potential using two-color two-step photoionization process. Coste et al. [28] have studied both valence and Rydberg autoionizing levels within 600 cm^{-1} above the first ionization potential using three-color three-photon photoionization spectroscopy. Manohar et al. [94] have studied the photoionization spectra of atomic uranium in the energy range $50,590\text{--}51,560\text{ cm}^{-1}$ by two-color three-photon ionization technique, using two copper vapor laser pumped dye lasers and observed large number of even-parity autoionizing levels. Ray et al. [145] have studied odd-parity autoionizing levels of atomic uranium using two-color two-step photoionization technique. In the recent past, by employing three-step resonance ionization mass spectrometry (RIMS), Miyabe et al. [95] have studied the AI levels of uranium in the energy region $49,930\text{--}51,200\text{ cm}^{-1}$ and reported the observation of over 200 even-parity AI levels. Schumann et al. [97] and Bushaw et al. [71] have investigated the even-parity AI levels in atomic uranium near the ionization threshold by using CW RIMS. Using two-color three-step photoionization spectroscopy, Marathe et al. [98] have reported the observation of several even-parity AI levels of uranium in the energy region $51,425\text{--}51,760\text{ cm}^{-1}$. More recently, Shah et al. [99] have studied a large number of autoionizing levels of uranium lying more than $2,000\text{ cm}^{-1}$ above the ionization limit by employing three-color optogalvanic (OG) spectroscopy technique. Despite this voluminous

work, the information on AI levels is scanty due to existence of unexplored energy levels with different J-values.

6.2.2 Total angular momenta

The J-values of AI levels are generally determined by exciting the level of interest from three different lower levels having J-values, J-1, J and J+1, based on the total angular momentum selection rules, i.e. $\Delta J = 0, \pm 1$ (J = 0 to J = 0 being not allowed). The unique J-value of an atomic level is determined if it is excited through all the three transitions or from two different levels having J-values differing by two. In a complex atom like uranium, where density of AI levels is very high and spectra are overlapping, the determination of J-values using J-selection method is generally cumbersome.

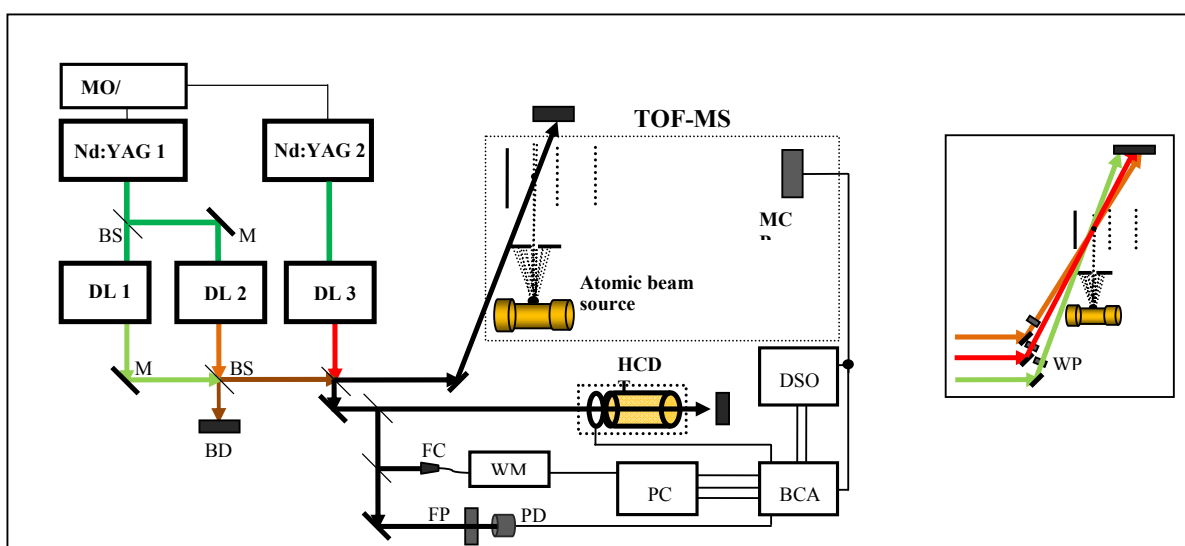
Greenland et al. [130,141] have developed an alternative technique to determine the J-values of AI levels of complex atoms using polarization combination method. In this method, laser polarization dependent PI yield for various combinations is measured and the resultant pattern is compared with the yield pattern obtained from the population excitation dynamics calculations for the possible J-values. Among the three PI yield patterns corresponding to probable three J-values of the excited level, the one which matches to the experimentally measured pattern defines the J-value of the AI level. Nittoh et al. [146] have further improved this method by considering linear polarization in addition to the circular polarization used earlier. Miyabe et al. [95] have exploited this method further and determined unique J-values of 80 AI levels of atomic uranium in the energy region 49,930-51,200 cm^{-1} . Despite the substantial efforts put in by various researchers worldwide, the information on the AI levels of uranium and their J-values is far from complete.

6.3 Present study of autoionizing levels and their angular momenta

In this section, we present the results of our investigations carried out on the photoionization spectra of atomic uranium in the energy region $49,959\text{--}51,504\text{ cm}^{-1}$ using three-color photoionization spectroscopy with pulsed dye laser systems in an atomic beam coupled to a time-of-flight mass spectrometer.

6.3.1 Experimental details

The experimental set-up used in these studies is shown in Fig. 6.1. The details of the experimental set-up have been discussed in chapter 2.



MO-Master Oscillator, EDG-Electronic delay generator, DL- Dye laser, M- mirror, BS- Beam splitter, BD- Beam dump, FPE- Fabry-Perot Etalon and PD- photo diode, WP-wave plate, TOF-MS –Time-of- flight mass spectrometer, MCP- Micro channel plate detector, HCDT-Hollow cathode discharge tube , DSO- Digital storage oscilloscope, WM-wavelength meter, FC-fiber coupler, PC- Personal computer, BCA- Box car averager.

Fig. 6.1: Schematics of the experimental set-up. Inset: arrangement for combining laser beams for polarization experiments.

During the measurements, typical laser pulse energy density in the interaction region were $\sim 20\text{--}100\text{ }\mu\text{J}/\text{cm}^2$, $50\text{--}200\text{ }\mu\text{J}/\text{cm}^2$, and $100\text{--}600\text{ }\mu\text{J}/\text{cm}^2$ for the first, second and third-step transitions, respectively. To ensure sequential (stepwise) excitation, a temporal delay of about 5 ns was introduced between the first and the second lasers optically and a similar delay

between the second and the third lasers was introduced using electronic delay generator. A PIN type photo diode was used to monitor the delay among the laser pulses. Spatial overlap among the laser beams was realized using beam splitter and beam steering optics. A part of the combined laser beams is made to pass through HCDT and FP etalon of 0.5 cm^{-1} free spectral range (FSR) for the purpose of laser wavelength calibration by simultaneously recording optogalvanic signal and FP etalon transmission fringes detected with a photodiode.

The combined laser beams were made to interact with the atomic beam perpendicularly and the resultant photoions produced were extracted, accelerated and introduced in the TOF-MS using delayed ($\sim 2 \text{ }\mu\text{sec}$) pulsed extraction and acceleration electric fields. In three-color photoionization studies of uranium, the first-step laser wavelength (λ_1) is acquired by tuning its wavelength across the transition of interest and observing the optogalvanic signal. The second-step dye laser was tuned to the respective second-step transition by observing the two-color three-photon ($\lambda_1+2\lambda_2$) photoionization signal in the TOF-MS. The three-color photoionization spectra of uranium were recorded by scanning the wavelength of the third dye laser while keeping the wavelengths of first and second-step lasers fixed. In the case where the total energy of ($\lambda_1+2\lambda_2$) is less than the ionization potential (IP) of uranium, the second-step dye laser wavelength was acquired by tuning its wavelength in the presence of the third-step dye laser kept at a fixed wavelength so that the energy of ($\lambda_1+\lambda_2+\lambda_3$) is more than the IP of uranium. During these experiments the laser wavelengths were monitored using a wavelength meter (High Finesse WS 06). The photoionization signals obtained from the TOF-MS along with the FP etalon transmission fringes and the pulsed OG signal derived from the HCDT were processed simultaneously using box-car averagers and, finally, recorded in a computer based data acquisition system. During these measurements, the third step laser wavelength was scanned at a rate of 0.002 nm/s .

For laser-polarization-based three-color photoionization experiments, the laser polarizations, which were vertically linear initially, were converted individually to generate various polarization combinations using various phase retarders. The circular polarization was generated using achromatic quarter wave plate and the plane of polarization was rotated by 90° using half wave plates. State of polarization at the output of the wave plate was verified using an analyzer or a combination of analyzer and a quarter wave plate. The desired state of polarization was obtained by introducing the wave plates in the path of individual beam and to maintain it in the interaction region a different method of laser beam combining, shown as inset in Fig.6.1, was adapted, where all the lasers were incident to the chamber with an angle of less than 1° between them instead of using beam splitters. In these studies we have used various polarization combinations such as $\pi\pi\pi$, $\Pi\pi\pi$, $\pi\pi\Pi$, RRR , $R\pi L$, $\pi L\pi$ where π , Π , R and L represent linear vertical, linear horizontal, right circular and left circular polarizations, respectively. In the PI yield measurements each data point was obtained after taking average of 64 laser pulses.

6.3.2 Theoretical: Calculations of photoionization yield for different combinations of laser polarizations

In a multi-step photoionization process, the polarization dependence of photoionization (PI) yield arises due to two reasons; firstly, the transition probability between magnetic sublevels is polarization dependent and secondly, the number of sublevels that participate in the excitation process is also affected by the state of laser polarization. The calculations of PI yield can be done either using density matrix equations or population rate equations depending upon the type of laser-atom interaction. In the present study it is justified to use population rate equations as the laser-atom interaction is incoherent [95, 109] due to (i) temporal width ($\Delta\tau$) of the laser being much greater than the coherence time (~ 0.4 ns) and (ii) the laser linewidth being much larger as compared to Rabi frequency of the transitions involved.

Assuming the state of laser polarization is perfect, each sublevel pathway is independent, spontaneous decays during the interaction are negligible, ground state population is uniformly distributed among the sublevels and the laser intensity profile is

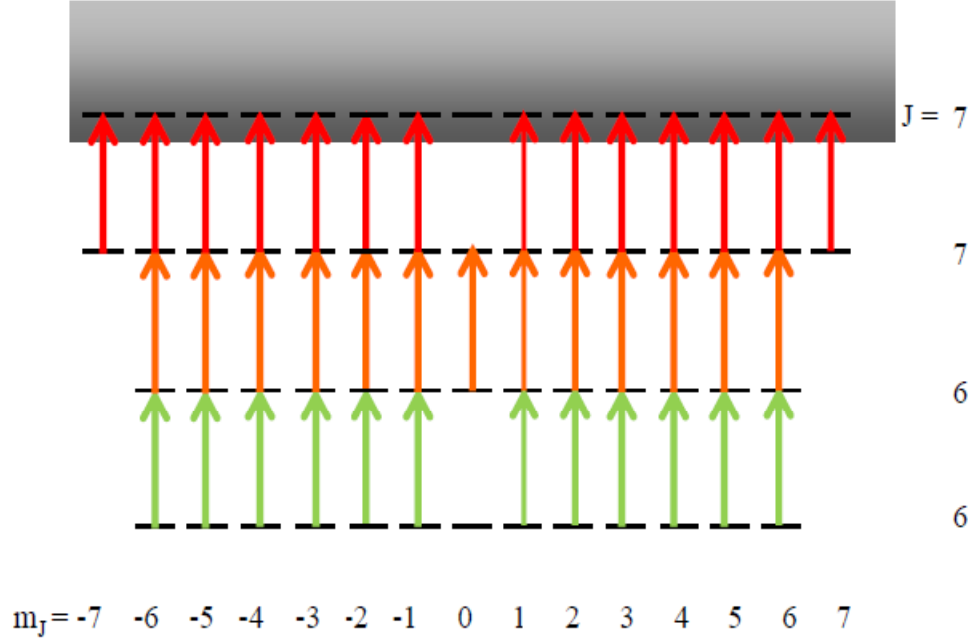


Fig. 6.2: Three-step three-color photoionization pathways of various magnetic sublevels of atomic uranium.

uniform in space, the population rate equations [95] for sublevels (Fig. 6.2) are as follows:

$$\frac{dn_{J_0 m_0}}{dt} = - \left(n_{J_0 m_0} - n_{J_1 m_1} \right) W_{J_1 m_1 \rightarrow J_0 m_0}^{q_1} \quad (6.2a)$$

$$\frac{dn_{J_1 m_1}}{dt} = \left(n_{J_0 m_0} - n_{J_1 m_1} \right) W_{J_1 m_1 \rightarrow J_0 m_0}^{q_1} - \left(n_{J_1 m_1} - n_{J_2 m_2} \right) W_{J_2 m_2 \rightarrow J_1 m_1}^{q_2} \quad (6.2b)$$

$$\frac{dn_{J_2 m_2}}{dt} = \left(n_{J_1 m_1} - n_{J_2 m_2} \right) W_{J_2 m_2 \rightarrow J_1 m_1}^{q_2} - W_{J_3 m_3 \rightarrow J_2 m_2}^{q_3} n_{J_2 m_2} \quad (6.2c)$$

$$\frac{dn_{J_3 m_3}}{dt} = W_{J_3 m_3 \rightarrow J_2 m_2}^{q_3} n_{J_2 m_2} \quad (6.2d)$$

where $W^{q_i}(J_u m_u, J_l m_l)$ represents the polarization (q_i) dependent photoexcitation rate for i^{th} step transition between the upper and the lower magnetic sublevels which can be expressed as

$$W_{J_u m_u, J_l m_l}^{q_i} = \frac{\sigma_{J_u m_u, J_l m_l}^{q_i} \varphi_i}{\Delta \tau} f_L(t) \quad (6.3),$$

here $\sigma_{J_u m_u, J_l m_l}^{q_i}$ is the polarization-dependent cross-section for a given laser linewidth, φ_i is the photon fluence i.e. number of photons per unit area per pulse, $\Delta \tau$ is the temporal width (FWHM) of the laser and $f_L(t)$ is the Gaussian temporal profile of the respective laser. Since we need to calculate relative PI yields for different polarization combinations, the absolute values of the cross-sections are not essential [95,130]. The polarization-dependent cross-section is related to isotropic cross-section σ_{J_u, J_l}^i by the following relation [16]

$$\sigma_{J_u m_u, J_l m_l}^{q_i} = 3(2J_l + 1) \begin{pmatrix} J_u & 1 & J_l \\ -m_u & q_i & m_l \end{pmatrix}^2 \sigma_{J_u, J_l}^i \quad (6.4)$$

where J_u and J_l are the total angular momentum values of the upper and lower levels of a transition, q_i represents the change in the magnetic quantum number $m_u - m_l$, taking the value of 0, +1 and -1 for the linear, the right circular and the left circular polarizations respectively. The sum of the populations in the AI sublevels determines the photoionization yield, i.e.

$$n_{ion} = \sum_{m_3=-J_3}^{J_3} n_{J_3 m_3} \quad (6.5)$$

For polarization combinations where orthogonal linear polarizations are used, i.e. $\Pi\pi\pi$ and $\pi\pi\Pi$, the quantization axis which is along the direction of laser polarization, rotates by 90° when laser the magnetic quantum number (m) changes to a new value m' . This leads to redistribution of atomic population among the magnetic sublevels. Population in the $|Jm\rangle$ sublevel is expressed as [147]

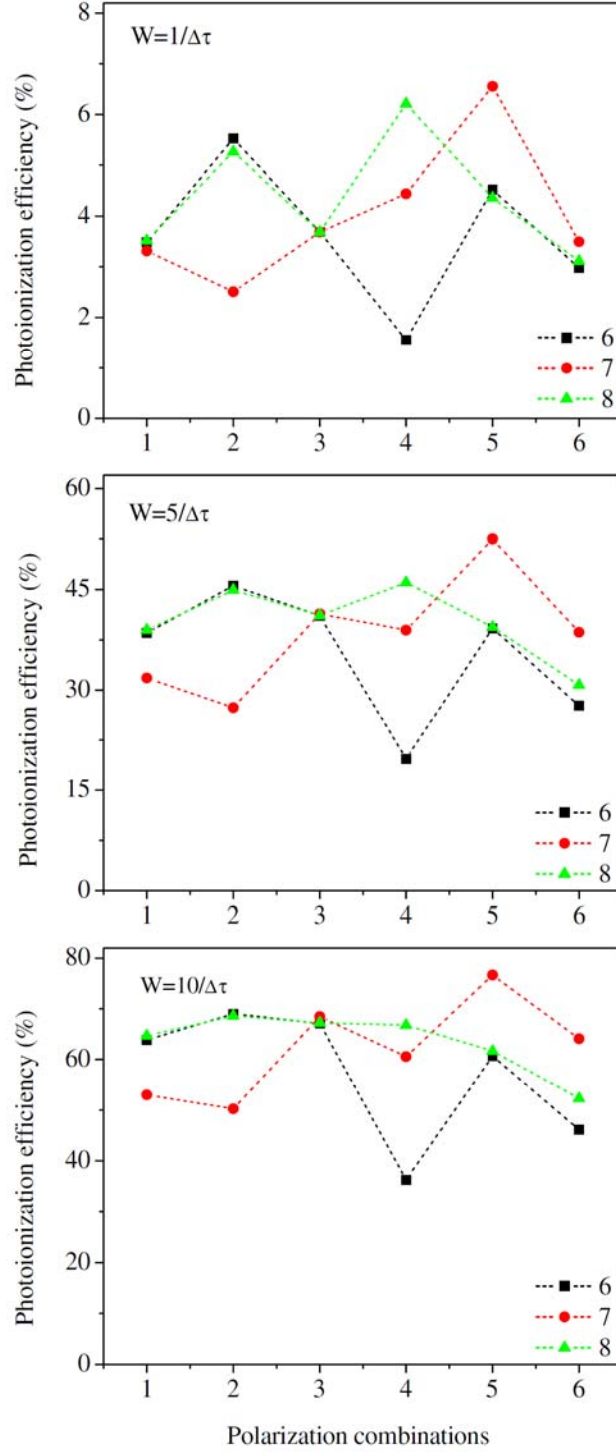


Fig. 6.3: Ionization yield pattern of photoionization schemes $6 \rightarrow 6 \rightarrow 7 \rightarrow (6, 7, 8)$ for different excitation rates (W). In these calculations, excitation rates for all the three-steps are considered equal, i.e. $W_1 = W_2 = W_3 = W$. $\Delta\tau$ is the temporal width of the laser pulse. Polarization combinations 1 to 6 denote $\pi\pi\pi$, $\Pi\pi\pi$, $\pi\pi\Pi$, RRR , $R\pi L$, $\pi\pi L$, respectively; where π , Π , R , L represents state of polarization such as vertical linear, horizontal linear, right circular and left circular, respectively.

$$n_{Jm'} = \sum_{m_3=-J_3}^{J_3} \left(d_{m'/m}^J(\theta) \right)^2 n_{Jm} \quad (6.6)$$

where $d_{m'/m}^J(\theta)$ is the Wigner rotation matrix element. For $\Pi\pi\pi$ and $\pi\pi\Pi$ combinations redistribution of population have been considered in the first and second excited level respectively, using equation 6.6.

To study the effect of excitation rates on the variation in the ionization yield pattern, calculations have also been carried out using $6 \rightarrow 6 \rightarrow 7 \rightarrow (6, 7, 8)$ photoionization schemes for various excitation rates as shown in Fig. 6.3. The gross ionization yield pattern remains very similar for excitation rates up to $5/\Delta\tau$ i.e. these patterns are insensitive to laser power or cross-sections as had already been reported by Greenland et al [130]. However, it is evident from Fig. 6.3 that with increase in the excitation rates, the PI yield, due to saturation of the transitions among the magnetic sublevels, does not show significant variations for different laser polarization combinations, thus, resulting in a PI pattern which is less distinguishable. Therefore, to obtain the PI pattern with large variations, it is advisable that the experiments should be performed with laser energy densities below the saturation energies of the transitions.

6.3.3 Results and discussion

6.3.3.1 Study of photoionization spectra

Photoionization spectra of uranium have been investigated employing eleven three-color three-step photoionization schemes. A schematic of various three-color three-step photoionization schemes used in the present work is shown in Fig. 6.4. The energy values of the second-excited levels used in these studies along with their J-values are listed in Table 6.1. A large number of photoionization spectra of uranium in the energy region 49,959–51,504 cm^{-1} have been measured using three-step photoionization schemes starting from the ground state ($^5L_6^0$). A part of the photoionization spectrum measured from the second excited level

$34,659.18 \text{ cm}^{-1}$ ($J = 7$) is shown in Fig. 6.5. More than 500 photoionization features of uranium are observed in these spectra. In addition, a dense level structure near $50,200 \text{ cm}^{-1}$ has also been observed, which is the signature of a Rydberg series converging to the second lowest ionic state (${}^6L^o_{11/2}$) and will be discussed later in detail. The true three-color AI features were identified by recording the spectra with λ_2 blocked, so that single- and two-color three-photon features are filtered out. The uncertainties in the measurements are minimized by repeating the measurements two to three times. The analysis of the spectra has resulted in the identification of over 199 new AI levels and confirmation of 147 levels reported earlier. The energy values of the AI levels and their linewidths (FWHM) along with the values reported in the literature are summarized in Table 6.2. The observed AI resonances whose linewidths are denoted by asterisk in Table 6.2 are either very broad or having

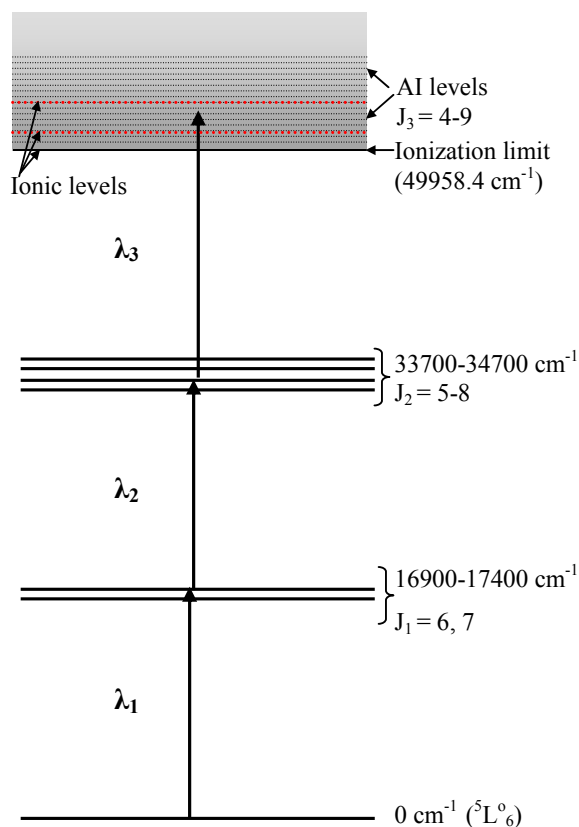


Fig. 6.4: Schematic of the three-step excitation schemes used for observing the autoionizing states of atomic uranium.

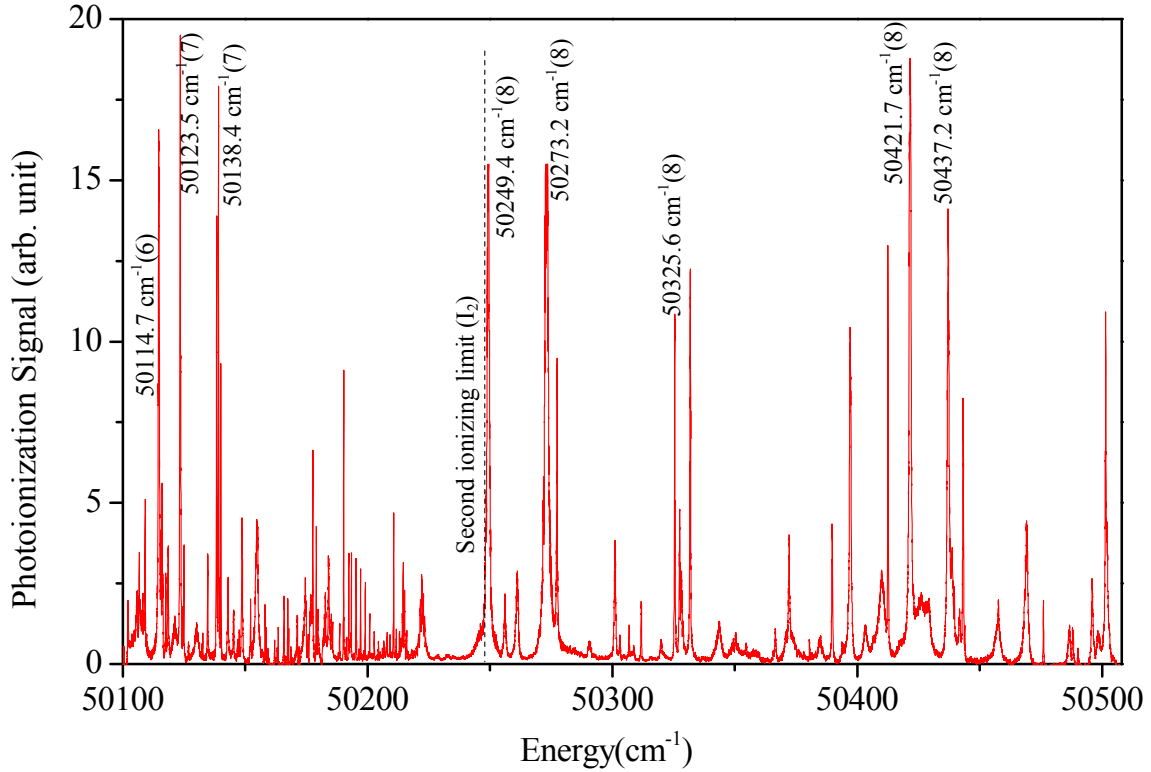


Fig. 6.5: Photoionization spectrum of uranium from $34,659.18 \text{ cm}^{-1}$ level. Dense levels structure near $50,200 \text{ cm}^{-1}$ is the Rydberg series converging to the second ionizing limit. To avoid complexity, the energy values and their J-values are shown only for few strong AI resonances.

asymmetric line shapes due to overlapping spectra. From the Fig. 6.5, it is evident that most of the AI resonances are symmetric in nature, which implies that interference between the transition probability amplitudes of the AI resonances and the continuum is insignificant or in other words the numerical index q (Fano-parameter) for these resonances is expected to be high. The energy values of the identified AI levels are determined from laser wavelength at the peak of resonance and the reported values of the intermediate levels [74,83]. The estimated uncertainties in the measurement of energy values of AI levels are in the range of ± 0.1 to 0.4 cm^{-1} . These uncertainties are statistical in nature and arise due to measurement in laser wavelength, asymmetry in the AI resonance, broad linewidth of AI resonances and also due to the uncertainties in the reported values of second excited levels. All those AI levels,

reported in the literature, whose energy values lie within the measurement uncertainties of the observed levels have been considered as the same level unless their J-values and linewidths are different. For example, from energy considerations, the AI level identified at $51,393.2 \text{ cm}^{-1}$ ($J = 6$) and the level $51,393.0 \text{ cm}^{-1}$ ($J = 7,8,9$) reported by Manohar et al. [94] would qualify as the same level but because of their different J-values such levels are labeled as new. On the contrary, a few AI levels, which are marked with dagger '†', whose linewidths are very large and shapes are asymmetric or where the linewidths of the corresponding reported levels are not mentioned in the literature [94], despite having energy difference slightly more than $\pm 0.4 \text{ cm}^{-1}$ in the measured and reported values have been assigned as the same level instead of claiming them new. It should be noted that the AI levels whose linewidths are below 0.15 cm^{-1} might be limited by the instrumental linewidth which is estimated to be about 0.12 cm^{-1} . The major contributors to the instrumental linewidth are the laser linewidths ($\sim 0.08 \text{ cm}^{-1}$), laser wavelength scanning speed and the signal integration time etc.

The most exhaustive study of the AI levels of uranium is by Miyabe et al. [95], where they have used more than 100 intermediate levels of $J = 4-8$. In comparison to that we have investigated the AI levels employing only eleven intermediate levels of $J = 5-8$. In spite of this, in the energy region common to both the studies, we could observe more than 91 AI levels from the expected 130 (allowed by electric dipole transition selection rules) reported by them. Moreover, for most of the levels, the energy difference between the measured and reported levels is found to be smaller than $\pm 0.2 \text{ cm}^{-1}$, which agrees with the estimated accuracy.

Table 6.1: Second excited levels used for the survey.

Energy (cm ⁻¹)		J-value	Symbol
a	B		
34,376.57	--	5	5A
33,853.28	33,853.279	5	5B
34,086.68	34,086.723	5	5C
34,372.87	34,372.982	6	6A
34,160.46	34,160.569	6	6B
34,028.11	--	6	6C
34,659.18	34,659.215	7	7A
33,737.49	--	7	7B
34,209.92	--	7	7C
34,048.40	--	7	7D
34,082.73	--	8	8A

^aMiyabe et al. [83], ^bBlaise et al. [74]

Table 6.2: Energies and J-values of autoionizing levels of uranium

Present work					Literature	
Energy (cm ⁻¹)	Observed in spectrum	Linewidth (cm ⁻¹)	J _{Set}	J _{Pol}	J	Energy (cm ⁻¹)
49,959.5	5A	0.4	4,5,6		6	49,959.447 ^a
49,964.1	5A	0.8	4,5,6		5,6	49,963.9 ^b
49,966.1	5A	0.8	4,5,6			
49,968.4	5A	0.6	4,5,6		6	49,968.194 ^a , 49,968.5 ^b
49,970.1	5A	0.1	4,5,6		6	49,970.1 ^b
49,972.6	5A	0.6	4,5,6	4	4	49,972.4 ^b
49,975.7	5A	0.2	4,5,6		5	49,975.651 ^a
49,977.8	5A	0.5	4,5,6		5	49,977.777 ^a , 49,977.9 ^b
49,979.8	5A	0.5	4,5,6		5	49,979.694 ^a , 49,979.8 ^b
49,983.8	5A	0.6	4,5,6		6	49,983.710 ^a , 49,983.7 ^b
49,985.0	5A	0.9	4,5,6	6	6	49,984.8 ^b
49,989.8	5A	0.3	4,5,6		6	49,989.5 ^b
49,992.2	5A	0.5	4,5,6			
49,994.5	5A	0.5	4,5,6		6	49,994.4 ^b
49,996.2	5A	0.2	4,5,6			
49,996.7	5A	0.6	4,5,6			
50,004.3	5A	0.7	4,5,6			
50,006.3	5A	0.4	4,5,6		6	50,006.1 ^b
50,008.2	5A	0.4	4,5,6			
50,020.6	5A	0.2	4,5,6		5,6	50,020.9 ^b
50,021.4	5A	0.2	4,5,6			
50,028.7	5A	0.5	4,5,6		4	50,028.5 ^b
50,032.7	5A	0.7	4,5,6		5,6	50,032.7 ^b
50,036.8	5A	0.25	4,5,6		5,6	50,036.8 ^b
50,039.8	5A	0.5	4,5,6			
50,042.1	5A	0.5	4,5,6		5,6	50,041.9 ^b
50,043.1	5A	0.2	4,5,6		5,6	50,043.3 ^b
50,043.6	5A	0.2	4,5,6		5,6	50,043.3 ^b
50,055.2	5A	0.3	4,5,6			
50,056.6	5A	0.3	4,5,6			
50,058.4	5A	1.2*	4,5,6			
50,060.1	5A	0.15	4,5,6			
50,061.0	5A	0.3*	4,5,6			
50,066.2	5A	0.8	4,5,6		6	50,066.1 ^b
50,068.7	5A	0.5	4,5,6		5,6,7	50,068.5 ^c
50,086.2	5A	0.4	4,5,6		6	50,086.3 ^b

Table 6.2 (Continued.)

Present work					Literature	
Energy (cm ⁻¹)	Observed in spectrum	Linewidth (cm ⁻¹)	J _{Sel}	J _{Pol}	J	Energy (cm ⁻¹)
50,087.0	5A	0.2	4,5,6			
50,088.5	5A	0.5	4,5,6			
50,091.0	5A	0.5	4,5,6		6	50,090.9 ^b
50,094.3	7A	0.5	6,7,8		7	50,094.3 ^b
50,094.9	5A	0.15	4,5,6			
50,095.9	5A	0.2	4,5,6			
50,097.4	5A	0.1	4,5,6		4,5,6	50,097.3 ^b
50,100.0	5A	0.3	4,5,6		6	50,099.9 ^b
50,100.5	7A	0.2	6,7,8		7,8	50,100.5 ^b
50,102.0	7A	0.2	6,7,8		6	50,102.1 ^b
50,102.4	5A	0.9	4,5,6		6	50,102.1 ^b
50,106.3	5A	0.4*	4,5,6			
50,109.1	7A	0.12	6,7,8		7	50,108.9 ^b
50,111.2	5A	0.5	4,5,6		5,6,7	50,111.4 ^c
50,114.7	7A	0.4	6,7,8	6		
50,115.6	7A	0.15	6,7,8		6	50,115.2 ^b
50,116.1	7A	0.15	6,7,8			
50,117.6	7A	0.15	6,7,8			
50,118.5	7A	0.3	6,7,8		5,6,7	50,118.5 ^c
50,120.5	5A	3*	4,5,6			
50,121.2	7A	1.2	6,7,8		5,6	50,121.3 ^b
50,123.5	7A	0.25	6,7,8	7	7	50,123.6 ^b
50,124.6	7A	0.07	6,7,8			
50,125.0	7A	0.1	6,7,8			
50,127.1	5A	0.2	4,5,6			
50,127.8	5A	0.12	4,5,6			
50,129.4	5A	0.9*	4,5,6			
50,130.2	7A	1.2	6,7,8			
50,133.8	5A	0.4*	4,5,6		6,7	50,133.5 ^b
50,134.7	5A,7A	0.5	6		6,7	50,134.7 ^b
50,135.9	5A	0.5	4,5,6			
50,138.4	7A	0.15	6,7,8	7	7	50,138.5 ^b
50,139.1	7A	0.12	6,7,8	8	8	50,139.2 ^b
50,139.6	5A,7A	0.12	6			
50,140.1	7A	0.12	6,7,8		8	50,140.1 ^b
50,143.0	7A	0.2	6,7,8			

Table 6.2. (Continued.)

Present work					Literature	
Energy (cm ⁻¹)	Observed in spectrum	Linewidth (cm ⁻¹)	J _{Set}	J _{Pol}	J	Energy (cm ⁻¹)
50,144.0	5A	0.3	4,5,6		5,6	50,143.8 ^b
50,145.3	5A,7A	0.25	6			
50,147.8	5A	0.1	4,5,6			
50,148.6	7A	0.3	6,7,8		6	50,148.3 ^b
50,152.1	5A,7A	0.15	6			
50,153.0	5A	0.3	4,5,6			
50,154.8	6A,7A	1*	6,7		6	50,154.7 ^b
50,156.0	5A	2*	4,5,6			
50,160.8	5A,6A	0.4	5,6			
50,162.2	6A,7A	0.12	6,7			
50,162.9	6A	0.2	5,6,7			
50,164.0	6A	0.25	5,6,7		7	50,163.8 ^b
50,165.1	5A	0.2	4,5,6			
50,166.0	5A,6A,7A	0.15	6			
50,166.7	6A	0.15	5,6,7			
50,168.0	6A,7A	0.1	6,7		7	50,167.8 ^b
50,168.8	5A,6A,7A	0.2	6			
50,169.7	6A	0.15	5,6,7		7	50,169.6 ^b
50,171.4	6A,7A	0.2	6,7			
50,171.9	6A,7A	0.2	6,7		5,6	50,172.3 ^b
50,173.0	6A	0.1	5,6,7			
50,174.5	7A	1.2*	6,7,8			
50,177.7	7A	0.15	6,7,8		7,8	50,177.6 ^b
50,179.1	7A	0.2	6,7,8			
50,179.8	6A,7A	0.2	6,7			
50,182.2	6A	0.15	5,6,7		7	50,182.0 ^b
50,184.2	5A,6A,7A	0.2	6		6	50,183.9 ^b
50,185.5	6A	0.15	5,6,7			
50,185.8	6A,7A	0.15	6,7			
50,187.2	6A	0.2	5,6,7		7	50,187.1 ^b
50,188.6	7A	0.15	6,7,8		7	50,188.5 ^b
50,189.4	5A,6A	0.4	5,6			
50,190.3	7A	0.15	6,7,8		8	50,190.2 ^b
50,194.7	5A,6A	0.4	5,6		5	50,194.5 ^b
50,210.6	7A	0.15	6,7,8	7	7	50,210.5 ^b
50,228.6	6A	1	5,6,7			

Table 6.2. (Continued.)

Energy (cm ⁻¹)	Present work				Literature	
	Observed in spectrum	Linewidth (cm ⁻¹)	J _{Sel}	J _{Pol}	J	Energy (cm ⁻¹)
50,242.0	5A,6A	1.2	5,6			
50,246.5	5A	1.2	4,5,6			
50,249.4	7A	0.7	6,7,8	8	8	50,249.4 ^b
50,256.2	6A,7A	0.7	6,7		7	50,256.2 ^b
50,261.3	5A,6A,7A	1	6	6	6	50,261.4 ^b
50,273.2	7A	1.6	6,7,8	8	8	50,273.1 ^b
50,277.5	7A	0.25	6,7,8	7	7	50,277.5 ^b
50,280.4	6A	1.4	5,6,7			
50,290.9	6A,7A	1	6,7			
50,301.2	5A,6A,7A	0.4	6	6		
50,303.2	6A,7A	0.3	6,7			
50,306.8	7A	0.1	6,7,8		7	50,306.8 ^b
50,307.8	6A	1.5	5,6,7			
50,308.8	7A	0.8	6,7,8		7,8	50,309.0 ^b
50,309.5	5A	0.6	4,5,6		4,5	50,309.9 ^b
50,311.7	6A,7A	0.3	6,7	7		
50,316.9	6A	1.5*	5,6,7			
50,320.0	7A	0.5	6,7,8			
50,322.7	5A	0.6	4,5,6			
50,325.6	7A	0.3	6,7,8	8	7,8	50,325.6 ^b
50,327.5	5A,6A,7A	0.4	6		6	50,327.3 ^b
50,329.5	5A	1	4,5,6			
50,331.9	7A	0.3	6,7,8	8	8	50,331.9 ^b
50,333.2	5A	1	4,5,6			
50,341.8	5A	1.8	4,5,6			
50,343.6	7A	1.3	6,7,8	7	7	50,343.5 ^b
50,346.1	5A,6A	0.8	5,6	5		
50,350.6	5A,6A,7A	0.6	6	6		
50,353.7	5A,6A	0.6	5,6	5		
50,358.0	6A	1.2*	5,6,7			
50,366.6	6A,7A	0.4	6,7		7	50,366.4 ^b
50,371.3	5A	1.2*	4,5,6			
50,372.3	7A	0.4	6,7,8		7,8	50,372.3 ^b
50,378.1	6A	0.2	5,6,7			
50,379.4	5A	0.2	4,5,6			
50,380.6	6A	0.2	5,6,7			

Table 6.2 (Continued.)

Present work					Literature	
Energy (cm ⁻¹)	Observed in spectrum	Linewidth (cm ⁻¹)	J _{Sel}	J _{Pol}	J	Energy (cm ⁻¹)
50,384.4	6A	1.2	5,6,7			
50,389.7	7A	0.4	6,7,8		6,7	50,389.8 ^b
50,392.7	5A,6A	0.6	5,6	6		
50,397.2	6A,7A	0.5	6,7	6		
50,400.8	5A	0.7*	4,5,6	4		
50,403.4	6A,7A	1.2*	6,7			
50,410.1	7A	1.5	6,7,8			
50,412.6	7A	0.3	6,7,8		8	50,412.7 ^b
50,413.8	5A,6A	0.8	5,6			
50,421.7	7A	1	6,7,8		8	50,421.8 ^b , 50,422 ^c
50,422.3	6A	1	5,6,7			
50,424.5	5A	1.2	4,5,6			
50,428.1	5A	1.3*	4,5,6			
50,432.4	5A,6A	1.2	5,6			
50,437.2	7A	0.8*	6,7,8		8	50,437.4 ^b
50,437.5	5A,6A	0.2	5,6			
50,438.9	5A,6A,7A	0.8	6	6	6	50,438.8 ^b
50,441.8	7A	0.5	6,7,8		7	50,441.6 ^b
50,443.3	7A	0.4	6,7,8		7	50,443.5 ^b
50,447.5	6A	0.4	5,6,7			
50,448.3	5A	0.6	4,5,6	5		
50,451.0	5A,6A	0.3	5,6	5		
50,457.7	6A,7A	0.3	6,7			
50,460.1	5A	1	4,5,6			
50,464.7	6A	0.5	5,6,7			
50,469.4	7A	0.8	6,7,8		7,8	50,469.0 ^b
50,471.2	5A	0.9	4,5,6	4		
50,476.1	7A	0.2	6,7,8		7,8	50,476.4 ^b
50,480.0	5A,6A	1.2	5,6			
50,486.7	5A,7A	0.8	6			
50,488.2	6A,7A	0.3	6,7			
50,490.2	5A,7A	0.2	6			
50,492.5	5A,6A	0.7	5,6			
50,494.2	5A,6A	0.3	5,6			
50,496.1	6A,7A	0.3	6,7			
50,497.4	6A	0.4	5,6,7			

Table 6.2 (Continued.)

Present work					Literature	
Energy (cm ⁻¹)	Observed in spectrum	Linewidth (cm ⁻¹)	J _{Sel}	J _{Pol}	J	Energy (cm ⁻¹)
50,498.5	7A	1	6,7,8			
50,501.3	6A,7A	0.3	6,7		7,8	50,501.3 ^b
50,519.0	6A	1	5,6,7			
50,530.7	6A	0.3	5,6,7		7,8	50,530.7 ^b
50,649.6	8A	0.25	7,8,9		9	50,649.5 ^b , 50,649.4 ^d
50,653.4	8A	1	7,8,9	8	7,8	50,653.7 ^b , 50,653.0 ^d
50,660.3	8A	1	7,8,9	8	7,8	50,660.3 ^b
50,691.4	8A	0.3	7,8,9	9	7,8,9	50,691.4 ^d
50,707.2	6B	4	5,6,7			
50,717.6	6B	4	5,6,7			
50,735.1	8A,6B	0.6	7	7	7,8,9	50,735.3 ^d
50,738.0	6B	1	5,6,7			
50,740.2	8A	0.6	7,8,9	8	7,8	50,740.1 ^b , 50,740.1 ^d
50,746.7	6B	2*	5,6,7			
50,755.9	8A	0.3	7,8,9	9	9	50,756.1 ^b , 50,755.9 ^d
50,756.5	6B	4*	5,6,7			
50,757.1	7B	1	6,7,8			
50,763.7	6B	1.8	5,6,7			
50,769.6	7B,8A	0.6	7,8	8	8	50,769.7 ^b , 50,769.5 ^d
50,770.8	7B	0.3	6,7,8		7,8,9	50,770.7 ^d
50,772.3	7B	0.1	6,7,8			
50,776.5	7B,8A	0.4	7,8	8	7,8	50,776.6 ^b
50,781.3	6B	1	5,6,7			
50,783.2	7B	0.5	6,7,8			
50,783.8	6B,7B,8A	0.6	7	7	7,8	50,783.9 ^b , 50,783.7 ^d
50,785.0	7B	0.2	6,7,8		7,8,9	50,784.9 ^d
50,785.7	7B	0.2	6,7,8		7,8,9	50,786.1 ^d
50,787.6	7B	1.2*	6,7,8		6,7,8	50,787.6 ^b , 50,787.6 ^d
50,788.4	6B	1.4	5,6,7			
50,789.3	6B	0.7	5,6,7			
50,791.9	7C	0.8	6,7,8			
50,796.7	6B	0.8*	5,6,7			
50,800.1	6B	0.7	5,6,7			
50,807.6	7C	2	6,7,8			
50,821.6	7B,7C,8A	0.4	7,8	7	7,8,9	50,821.6 ^d
50,826.0	7B	0.15	6,7,8		7,8,9	50,825.9 ^b , 50,825.7 ^d

Table 6.2 (Continued.)

Present work					Literature	
Energy (cm ⁻¹)	Observed in spectrum	Linewidth (cm ⁻¹)	J _{Sel}	J _{Pol}	J	Energy (cm ⁻¹)
50,826.8	6B,7B,7C	0.4	6,7			
50,831.4	6B	3*	5,6,7			
50,838.1	7B	0.2	6,7,8			
50,839.8	8A	0.8	7,8,9	7	7,8,9	50,840.0 ^d
50,844.3	7B,7C	0.4	6,7,8		7,8,9	50,843.9 ^d
50,849.5	8A	0.2	7,8,9	7		
50,851.0	7B,7C	2.1	6,7,8			
50,856.4	7C	0.3	6,7,8			
50,861.5	7B	0.8	6,7,8			
50,864.0	8A	0.2	7,8,9	9	7,8,9	50,864.0 ^d
50,869.3	7C	1	6,7,8			
50,875.2	7B,7C	0.2	6,7,8		8	50,875.2 ^b , 50875.3 ^d
50,883.6	7B,7C	1.5	6,7,8		6,7,8	50,883.9 ^b , 50883.7 ^d
50,892.5	7C	0.4	6,7,8			
50,903.3	7B	2	6,7,8		7,8,9	50,903.6 ^d
50,909.7	7B	0.8	6,7,8			
50,919.4	7B,7C	0.8	6,7,8			
50,922.7	7B,7C	0.6	6,7,8		7,8,9	50,922.8 ^d
50,931.4	7B,7C	0.4	6,7,8		7,8,9	50,931.6 ^d
50,932.1	7B,7C	0.7*	6,7,8		7,8,9	50,932.5 ^b , 50,932.5 ^d
50,939.9	7C,7B,5B	0.5	6			
50,942.7	7B,7C	0.3	6,7,8		7,8,9	50,943.1 ^b , 50,943.1 ^d
50,953.8	7B	0.6	6,7,8			
50,961.3	7B	0.5	6,7,8		7,8	50,961.4 ^b , 50,961.4 ^d
50,967.9	7C	2	6,7,8		7,8,9	50,967.7 ^d
50,976.7 [†]	7B	2*	6,7,8		7,8,9	50,977.4 ^d
50,979.8	7B,7C	0.4	6,7,8		7,8,9	50,980.0 ^d
50,989.5 [†]	7B,7C	2*	6,7,8		7,8,9	50,990.0 ^d
50,997.7	5B	1	4,5,6			
51,007.0	7B	0.6	6,7,8			
51,009.5	7B,7C	0.5	6,7,8		7,8,9	51,009.5 ^d
51,013.5	5B,7C	0.7	6			
51,021.0	5B,7C	0.7	6			
51,029.2	5B	1.1	4,5,6			
51,036.4	5B,6C	1	5,6			
51,041.4	5B	1	4,5,6			

Table 6.2 (Continued.)

Present work					Literature	
Energy (cm ⁻¹)	Observed in spectrum	Linewidth (cm ⁻¹)	J _{Sel}	J _{Pol}	J	Energy (cm ⁻¹)
51,049.4	5B	0.8	4,5,6			
51,053.8	5B	0.8	4,5,6			
51,058.6	5B	1.3	4,5,6			
51,062.3	5B	1.2	4,5,6			
51,103.8	6C	1	5,6,7			
51,116.8 [†]	6C	1.4	5,6,7		7,8,9	51,117.5 ^d
51,158.5	6C	0.9	5,6,7		7,8,9	51,158.3 ^d
51,182.3	7A	0.6	6,7,8		7,8,9	51,182.4 ^d
51,187.4	6C,7A	0.6	6,7			
51,192.8	7A	1	6,7,8			
51,200.1 [†]	7A	1.6*	6,7,8		7,8,9	51,199.3 ^d
51,203.4	5C	0.8	4,5,6			
51,209.0	7A	1.3	6,7,8			
51,210.9	5C	0.3	4,5,6			
51,212.5	7A	0.1	6,7,8		7,8,9	51,212.6 ^d
51,214.1	7A,6C	0.3*	6,7			
51,216.1	7A	0.8	6,7,8		7,8,9	51,216.1 ^d
51,219.0	7A	0.3	6,7,8		7,8,9	51,219.0 ^d
51,220.6	5C	1*	4,5,6			
51,225.6	7A	1.3*	6,7,8		7,8,9	51,225.8 ^d
51,227.0	5C	1.2	4,5,6			
51,232.1	5C	1.2	4,5,6			
51,232.6 [†]	7A	0.8	6,7,8		7,8,9	51,233.2 ^d
51,235.7	5C	1.4	4,5,6			
51,237.4	7A	1	6,7,8	8		
51,238.3	5C	1	4,5,6			
51,246.2 [†]	7A	1	6,7,8		7,8,9	51,246.7 ^d
51,252.6	5C	0.7	4,5,6			
51,253.1	5C,6C,7A	0.6	6	6		
51,260.3	7A,6C	0.7	6,7			
51,263.0	5C	1.6	4,5,6			
51,267.4	5C,7A	1	6			
51,271.5	7A	0.7	6,7,8	8		
51,272.7	5C,6C	0.5	5,6			
51,274.1	7A,5C	0.6	6			
51,278.2	7A,5C	0.3	6			

Table 6.2 (Continued.)

Present work					Literature	
Energy (cm ⁻¹)	Observed in spectrum	Linewidth (cm ⁻¹)	J _{Sel}	J _{Pol}	J	Energy (cm ⁻¹)
51,280.3	5C,6C	0.7	5,6			
51,287.2	7A,5C	1.1*	6			
51,290.1	7A	1.2	6,7,8		7,8,9	51,290.3 ^d
51,302.0	7A,5C	2.5	6			
51,314.2	7A,5C	1.5	6			
51,315.1	7D	1.1	6,7,8		7,8,9	51,314.9 ^d
51,320.3	7A	0.5	6,7,8		7,8,9	51,320.5 ^d
51,321.5	7A,5C	0.5	6			
51,322.7	5C	0.6	4,5,6			
51,326.6	5C	0.5	4,5,6			
51,327.0	7A	0.3*	6,7,8		7,8,9	51,327.3 ^d
51,327.8	5C	0.4	4,5,6			
51,328.3	7A	0.8	6,7,8		7,8,9	51,328.5 ^d
51,330.6	5C	0.7*	4,5,6			
51,331.6	7D	0.2	6,7,8		7,8,9	51,331.7 ^d
51,333.5	5C	0.8	4,5,6			
51,335.8	7A	0.3	6,7,8		7,8,9	51,336.0 ^d
51,337.0	7A,5C	0.7	6			
51,342.4	7A	1	6,7,8		7,8,9	51,342.6 ^d
51,344.6	7A	0.2	6,7,8		7,8,9	51,344.7 ^d
51,352.5	7A,7D	0.6	6,7,8	8		
51,357.5	5C	2	4,5,6			
51,360.3	7A,7D	0.6	6,7,8	7	7,8,9	51,360.4 ^d
51,365.8	5C,7D	0.5	6			
51,367.3 [†]	7A,7D	0.5	6,7,8		7,8,9	51,367.8 ^d
51,370.2	7A	0.4	6,7,8			
51,374.9	7A	0.4	6,7,8		7,8,9	51,375.1 ^d
51,376.2	7A,7D	0.6	6,7,8		7,8,9	51,376.4 ^d
51,377.6	7A,7D	0.3	6,7,8		7,8,9	51,377.8 ^d
51,378.5	5C	2.2*	4,5,6			
51,380.8	5C,6C	0.4	5,6			
51,381.2	7A,7D	0.6	6,7,8			
51,388.5	7D	0.5	6,7,8		7,8,9	51388.5 ^d
51,393.2	7A	0.6	6,7,8	6		
51,397.4	5C	1.1*	4,5,6			
51,400.4	5C,7A	0.3	6			

Table 6.2 (Continued.)

Present work					Literature	
Energy (cm ⁻¹)	Observed in spectrum	Linewidth (cm ⁻¹)	J _{Sel}	J _{Pol}	J	Energy (cm ⁻¹)
51,401.8	7D	0.5	6,7,8			
51,403.1	7A	0.8	6,7,8	7	7,8,9	51,403.3 ^d
51,404.2	5C	0.5	4,5,6			
51,405.7	7A	0.4	6,7,8		7,8,9	51,406.0 ^d
51,410.1	7A	0.8*	6,7,8		7,8,9	51,410.0 ^d
51,411.1	7D	0.7	6,7,8			
51,413.9	7D	0.8	6,7,8			
51,418.8	7A	1.2	6,7,8	8	7,8,9	51,418.6 ^d
51,425.5	7A	0.8	6,7,8	7	7,8,9	51,425.7 ^d , 51,425.4 ^f
51,429.8	7A	0.3	6,7,8		7,8,9	51,430.1 ^d
51,434.9	7D	0.6	6,7,8			
51,439.2	7A,7D	0.6	6,7,8			
51,441.9	7A,7D	0.7	6,7,8	8		
51,456.4	7D	0.3	6,7,8			
51,458.1	7D	0.5	6,7,8		7,8,9	51,458.3 ^d , 51,458.4 ^f
51,458.7	7D	0.6	6,7,8		7,8,9	51,459.1 ^d
51,461.0	5C	1	4,5,6			
51,462.5	7D	0.5	6,7,8			
51,465.0	7D	1	6,7,8			
51,478.1	7D	0.4	6,7,8		7,8,9	51,478.5 ^d , 51,478.5 ^f
51,494.4	7D	0.4	6,7,8			
51,503.3	7D	0.3	6,7,8			

^a Schumman et. al [97].^b Miyabe et. al [95].^c Rodrigues et. al [96].^d Manohar et. al[94].^e Greenland et al.[130]^f Marathe et al. [98]

6.3.3.2 Determination of J-values

The J-values of AI levels are determined using the method of laser polarization combinations as well as the method based on J-selection rules. In the J-selection method, as mentioned before, unique J-values are assigned to those AI levels which are excited either from three different lower levels J-1, J and J+1 or from levels J-1 and J+1, i.e. from two levels, whose J-values differ by two. The remaining AI levels where these set of excitations were not observed, two to three possible J-values were assigned. The J-values of AI levels assigned by this method are listed in column (J_{sel}) of Table 6.2.

In the polarization method, variations in the PI yield for different polarization combinations of lasers and the resultant PI yield pattern is compared with those obtained from the population–excitation dynamics calculations for three possible J-values. Fig. 6.6 shows the theoretical and experimentally measured PI yield patterns for a photoionization scheme $6 \rightarrow 6 \rightarrow 7 \rightarrow (6,7,8)$. In this scheme, the first and the second excited levels considered are $17,361.89 \text{ cm}^{-1}$ and $34,659.18 \text{ cm}^{-1}$, respectively. In Fig. 6.6, we have superimposed experimentally measured PI yield pattern for AI levels at $50,331.9 \text{ cm}^{-1}$, $50,301.2 \text{ cm}^{-1}$ and $50,197.17 \text{ cm}^{-1}$ over the theoretically calculated yield patterns for three possible J-values after normalization. The level at $50,197.17$ is an AI Rydberg level. A reasonably good match between experimentally measured patterns with one of the three theoretically calculated ones is quite evident from the figure. The unambiguous J-values of the AI energy levels at $50,331.9 \text{ cm}^{-1}$, $50,301.2 \text{ cm}^{-1}$ and $50,197.17 \text{ cm}^{-1}$ are 8, 6 and 7 respectively. The slight deviation in the experimentally measured photoionization yield values from the calculated one could be due to difficulties in realizing exact input parameters, experimentally, used in the theoretical model like state of laser polarization, uniform excitation rates, etc. But, these small deviations do not change the pattern significantly. Using

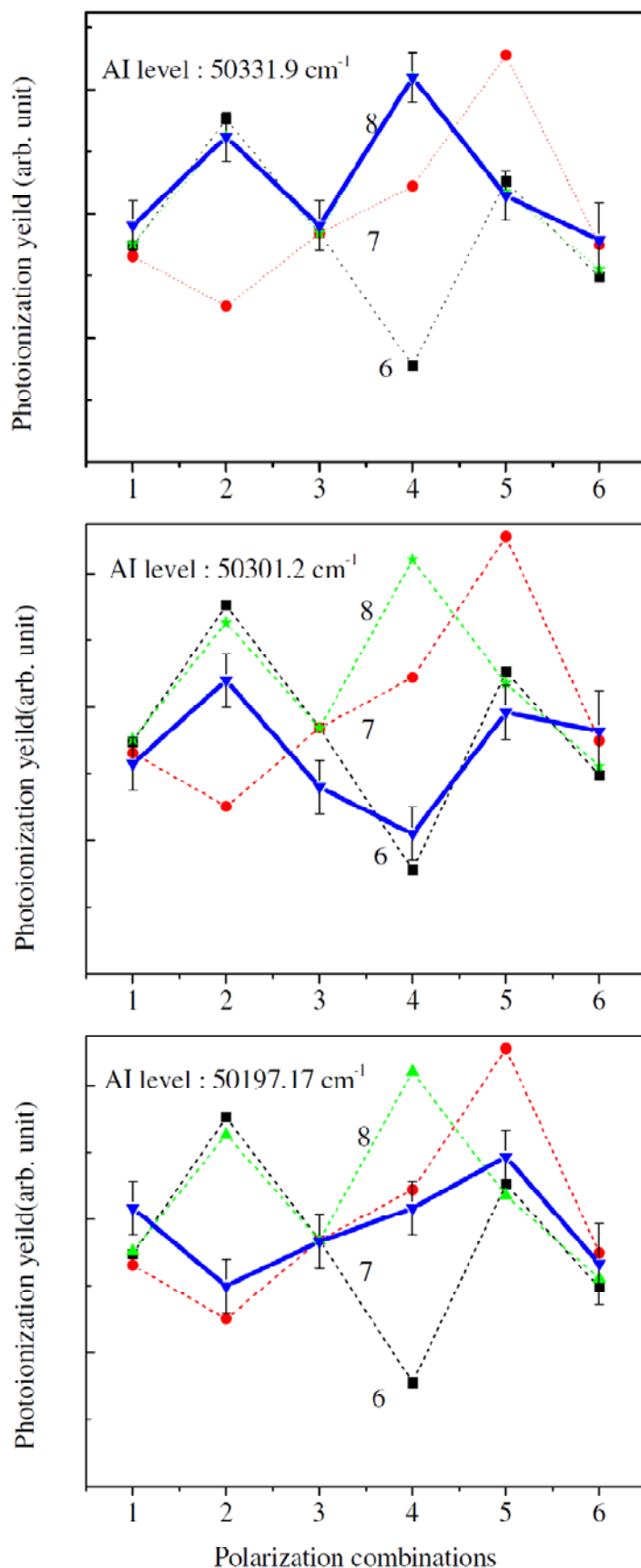


Fig. 6.6 Theoretical and experimental yield pattern for a photoionization scheme $6 \rightarrow 6 \rightarrow 7 \rightarrow (6,7,8)$. In this scheme, the first and the second excited levels considered are $17,361.89 \text{ cm}^{-1}$ and $34,659.18 \text{ cm}^{-1}$, respectively. Polarization combinations 1 to 6 denote $\pi\pi\pi$, $\Pi\pi\pi$, $\pi\pi\Pi$, RRR , $R\pi L$, $\pi\pi L$, respectively; where π , Π , R , L represents state of polarization such as vertical linear, horizontal linear, right circular and left circular, respectively. Blue line represents experimentally measured yield patterns. Measured J -values for $50,331.9 \text{ cm}^{-1}$, $50,301.2 \text{ cm}^{-1}$ and $50,197.17 \text{ cm}^{-1}$ are 8, 6 and 7, respectively.

the same methodology, we have assigned unique J-values to forty nine AI levels. The J-values of AI levels assigned by polarization methods are listed in column (J_{pol}) of Table 6.2. A good agreement has been observed in the J-values determined by both of these methods as well as the values previously reported in the literature. It has also been observed that linewidth of AI levels having large J-values i.e. $J = 8, 9$ are generally narrow, as reported earlier [28,95,97]. The plausible explanation for this phenomenon is that in an autoionization process, the atoms excited to AI levels decay to lower ionic levels of uranium (in the present case $^4\text{I}_{9/2}^{\circ}$ and $^6\text{I}_{11/2}^{\circ}$), by ejecting an electron while conserving the total energy and the angular momentum. Therefore, the width of the AI levels having higher J-values are expected to be narrow, as the ejected electron has to carry higher value of angular momentum which limits the autoionization rate due to centrifugal potential barrier [95,144].

6.3.3.3 Analysis of Rydberg Series

In addition to valence AI levels, an AI Rydberg series converging to the second-lowest ionic level ($^6\text{L}_{11/2}^{\circ}$) of uranium has also been observed in the ionization spectrum recorded from the second excited level at $34,659.18 \text{ cm}^{-1}$. A rich levels structure around $50,200 \text{ cm}^{-1}$ appearing in the photoionization spectrum presented in Fig. 6.5, is the signature of the Rydberg series. To distinguish the AI Rydberg levels from the valence levels, photoionization spectra were recorded in the presence of electric fields by synchronizing laser pulses with pulsed extraction electric field. Owing to high electric polarizability, the Rydberg levels are very sensitive to the presence of electric field. Thus, in the presence of high electric field, the autoionizing Rydberg levels may get shifted, broadened, split into many levels or disappear completely. The disappearance of the AI Rydberg levels structure in presence of electric fields of 120 V/cm has thus confirmed the Rydberg series reported earlier by Coste et al. [28] and Miyabe et al. [95] in the ionization spectra recorded from $33,421.07 \text{ cm}^{-1}$ and $34,434.792 \text{ cm}^{-1}$ levels, respectively. AI Rydberg progression observed from $34,659.18 \text{ cm}^{-1}$

is shown in Fig. 6.7. The J-values of these levels are determined by polarization method and are found to be 7. It is observed that the strength of the autoionizing Rydberg resonances decreases gradually with increasing quantum number up to 52 and thereafter the series is found to be heavily perturbed due to nearby AI levels of other configurations. Hence, only 13 members of Rydberg series are identified and listed in Table 6.3. The slight deviation, up to 0.05 cm^{-1} , in our measured energy values of Rydberg AI levels as compared to the one

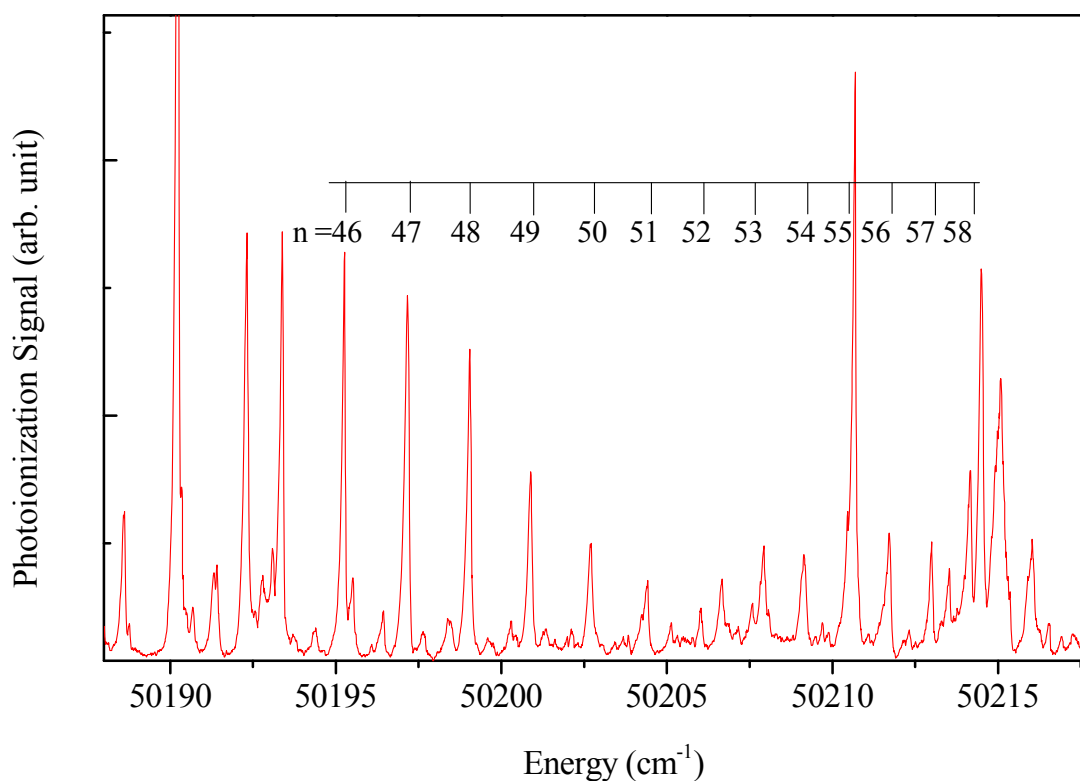


Fig. 6.7: Autoionizing Rydberg series observed from 34659.18 cm^{-1} level.

reported in literature is probably due to variation in the reported values of the second excited level ($\sim 0.035 \text{ cm}^{-1}$) used in calculating these values [28, 29]. The other reason for this deviation could be the perturbation of valence AI level present at $50,210.6 \text{ cm}^{-1}$ in the Rydberg series. The measured energy values of Rydberg AI levels are, in general, more

accurate compared to values listed in Table 6.2. This is due to the fact that the linewidth of the observed AI Rydberg progression is narrow ($\sim 0.12 \text{ cm}^{-1}$) which helps in defining the peak of the resonance more precisely. To determine the second ionization limit (I_2), we have

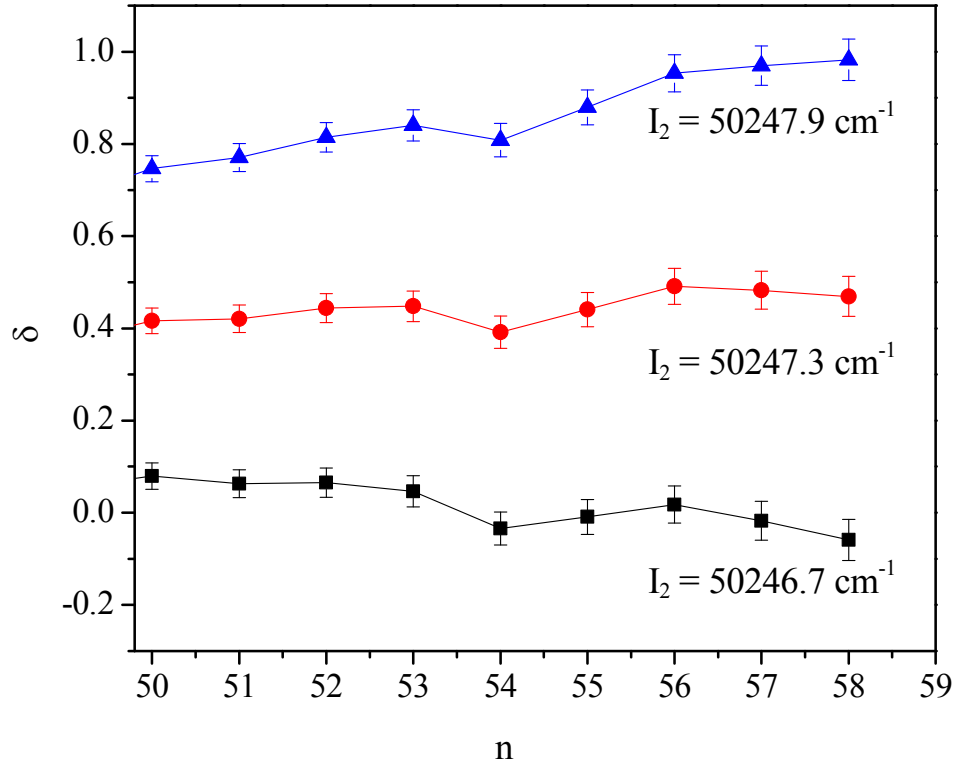


Fig. 6.8: Plot of quantum defect ($\delta = n - n^*$) versus principal quantum number (n) for various assumed second ionization limits for the AI Rydberg series of Table 3. The nearest integer corresponding to the calculated effective quantum number (n^*) has been assumed as principal quantum number.

calculated effective quantum number (n^*) for each level using the Rydberg-Ritz formula $E_{\text{Ryd}} = I_2 - R_U/(n^*)^2$ for three assumed values of I_2 (50,246.7 cm^{-1} , 50,247.3 cm^{-1} and 50,247.9 cm^{-1}). Here, E_{Ryd} is the level energy and R_U is the mass corrected Rydberg constant for uranium (1,09,737.063 cm^{-1}). Assuming the nearest integer (n) corresponding to the calculated n^* as principal quantum number, the quantum defects ($\delta = n - n^*$) have been

determined all along the AI Rydberg series for all the three values of the second ionization limit. The measured and reported energy values,

Table 6.3: Autoionizing Rydberg levels of uranium. ‘n’ represents nearest integer corresponding to the calculated effective quantum number (n^*). $\delta = n - n^*$, represents the quantum defect.

Energy (cm^{-1})	n	Present work			Reported	
		δ for assumed I_2 (cm^{-1})			Energy (cm^{-1})	
		50246.7	50247.3	50247.9	a	b
50,195.26	46	-0.19	0.08	0.34	50,195.25	50,195.27
50,197.17	47	-0.07	0.22	0.49	50,197.15	50,197.17
50,199.04	48	0.02	0.32	0.61	50,199.04	50,198.99
50,200.90	49	0.05	0.37	0.68	50,200.90	50,200.90
50,202.67	50	0.08	0.42	0.75	50,202.70	50,202.67
50,204.41	51	0.06	0.42	0.77	50,204.41	50,204.42
50,206.02	52	0.06	0.44	0.81	50,206.03	50,206.03
50,207.57	53	0.05	0.45	0.84	50,207.58	50,207.61
50,209.11	54	-0.03	0.39	0.81	50,209.05	50,209.06
50,210.44	55	-0.01	0.44	0.88	50,210.40	50,210.42
50,211.69	56	0.02	0.49	0.95	50,211.76	50,211.76
50,212.95	57	-0.02	0.48	0.97	50,213.00	50,213.00
50,214.15	58	-0.06	0.47	0.98	50,214.16	50,214.18

^a Miyabe et al. [95], ^b Coste et al. [28]

principal quantum number and δ values are listed in Table 6.3. The determined δ values as a function of principal quantum number ‘n’ for all the three values of I_2 are plotted in Fig. 6.8. The value of I_2 accepted as the second ionization limit is the one for which δ values are most constant. From the figure, it is evident that δ values are nearly constant for $I_2 = 50,247.3 \text{ cm}^{-1}$ and diverging for the remaining two. Therefore, our measured value of I_2 is $50,247.3 \pm 0.6 \text{ cm}^{-1}$, and it matches well with the value $50,247.3 \pm 0.5 \text{ cm}^{-1}$ reported by Coste et al. [28].

Chapter 7 - Resonance ionization spectroscopy of atomic uranium in U-Ne hollow cathode discharge

7.1 Introduction

In the preceding chapters, measurements of atomic parameters of uranium have been described by performing resonance ionization spectroscopy (RIS) in atomic beam coupled with time-of-flight mass spectrometer. As an alternative, photoionization studies of uranium have been carried out in a hollow cathode discharge tube (HCDT), a much simpler device compared to the bulky and expensive atomic beam setup consisting of vacuum chamber, high temperature oven, detector etc. generally used for photoionization spectroscopy of refractory elements like Zr, Gd, U etc.

Hollow cathode discharge tubes (HCDTs) are excellent sources of sputtering of their cathode material owing to their favorable electrical properties and, consequently, generators of atomic vapors of spectroscopic quality. HCDTs are generally used as a spectroscopic light source in atomic absorption and emission spectroscopy [5,148,149]. In conjunction with tunable dye lasers, these HCDTs are routinely used to generate absorption spectra of cathode material using optogalvanic spectroscopy[7,12]. Optogalvanic effect is basically a light induced change of electrical properties of the discharge. The resonant excitation of the atomic vapors in the gas discharge give rise to its impedance variation either due to change in an indirect charge production rate or through a variation in the electron temperature through super-elastic collision with excited atoms. The change in discharge impedance is picked up as a variation in the discharge current or voltage across the discharge or ballast resistor. Brogila et al. [150] have shown that OG signal consists of two components, namely fast and slow. The slow component of the OG signal is the result of resonant excitation whose duration is decided by plasma relaxation processes in the discharge tube and has characteristic times in

the μs range. The fast component of the OG signal is the result of direct photoionization produced by laser beam in the cathode dark space and instantaneous extraction of photoelectrons by the strong electric field present therein, thus having a duration roughly that of the laser pulse. Levesque et al. [151] have called this rapid optogalvanic signal a photoionization optogalvanic (PIOG) signal and systematically investigated the possibility of the use of the PIOG technique for laser spectroscopy, pointing out its potentials and limitations. Babin and Gagne [152] had used the fast signal as a diagnostic tool for measuring the width of CDS in hollow cathode discharges under different experimental conditions.

Broglia et al. [153] have investigated the high-lying states of uranium employing multistep optogalvanic (OG) spectroscopy in a commercial U-Ne hollow cathode discharge tube (HCDT) and showed that the results obtained by this simple technique are comparable to those obtained by conventional complex detection methods employing atomic beams, within the resolution limits of the two techniques. Recently, Shah et al. [99] have identified 102 even-parity autoionizing levels of uranium by performing a three-color three-step OG spectroscopy of uranium in U-Ne HCDT. However, because of many other dominating ionization processes taking place in the discharge the use of OG spectroscopy in photoionization studies has some difficulties [96]. But due to efficient extraction of photoions in the cathode dark space PIOG technique is generally more sensitive.

By employing PIOG spectroscopy technique, Levesque et al. [92] have studied single-color three-photon photoionization spectrum of uranium over a large spectral range. Stockhausen et al. [154] have used the PIOG signal to measure the photoionization cross section and number density of copper by fitting it with the theoretical model. Vas Dev et al. [93] and Marathe et al. [98] have explored this technique further to carry out two-color three-photon photoionization spectroscopy of uranium in U-Ne and U-Ar HCDT and reported the investigations on the high-lying odd-parity atomic states and even-parity AI states of uranium.

Lee et al. [155] have reported the observation of AI states of Gadolinium using time-resolved three-color optogalvanic spectroscopy by comparing the PIOG spectrum with that of Guyadec et al. [156] obtained in atomic beam. Using a pulsed U-Ne HCDT as an atomic vapor source, Rodrigues et al. [96] have studied photoionization spectra of uranium after the discharge employing multi-step photoionization spectroscopy. We have now setup a three-color PIOG spectroscopy technique for uranium in a U-Ne HCDT using three tunable pulsed dye lasers.

In this chapter, measurements of various atomic parameters of uranium using PIOG spectroscopy are presented. Using this technique, photoionization spectra of uranium have been investigated in the energy region $52,150\text{--}52,590\text{ cm}^{-1}$, not explored so far, through three different excitation pathways starting from the ground state of uranium 0 cm^{-1} ($^5L^{\circ}_6$). Further, the potential of PIOG technique has been explored to measure the isotope shifts of the high-lying levels and photoexcitation/photoionization cross section of atomic uranium. These measurements have been compared with the results obtained from atomic beam coupled with time-of-flight mass spectrometer and the results are encouraging.

7.2 Experimental setup

The general experimental setup used for PIOG spectroscopy is similar to that discussed in chapter 2. It consisted of two Nd:YAG-pumped three dye lasers (Quantel model YG 981, TDL 90), a see-through-type homemade U-Ne HCDT (cathode length 30 mm, inner diameter 8 mm), a digital storage oscilloscope for signal monitoring and a boxcar averager (BCA) for further signal processing. HCDT filled with Ne gas of spectroscopic grade at 2.2 mbar was mounted on an X-Y translational stage and operated at a discharge current of ~ 50 mA. The photograph of HCDT is shown in Fig. 7.1. It consisted of an hollow cylindrical



Fig. 7.1: HCDT used in the present experiments.

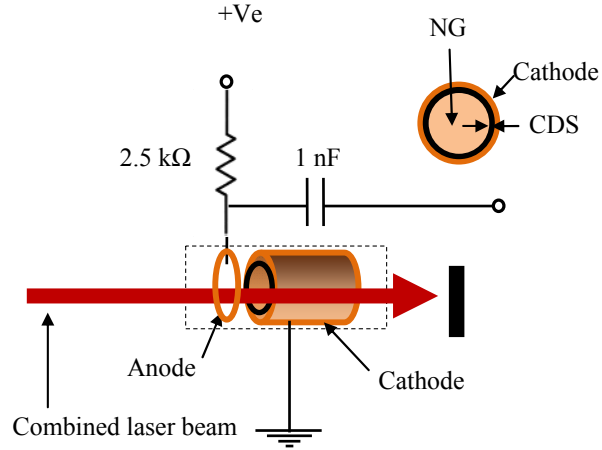


Fig. 7.2: Schematic of HCDT and electrical circuit diagram.

cathode of natural uranium which is electrically grounded and a tungsten anode placed in front of the cathode in the form of a ring. Schematic of the circuit diagram for performing PIOG spectroscopy in HCDT is shown in Fig. 7.2. A constant voltage power supply was connected across the HCDT through a current limiting resistor of 2.5 K Ω . At the anode terminal, a 1 nF decoupling capacitor was used to separate the pulsed OG/PIOG signal by blocking the DC voltage. The cross sectional view of the HCDT and variation of electric field in

the CDS is shown in Fig. 7.3 a & b. When photoionization is performed in the cathode dark

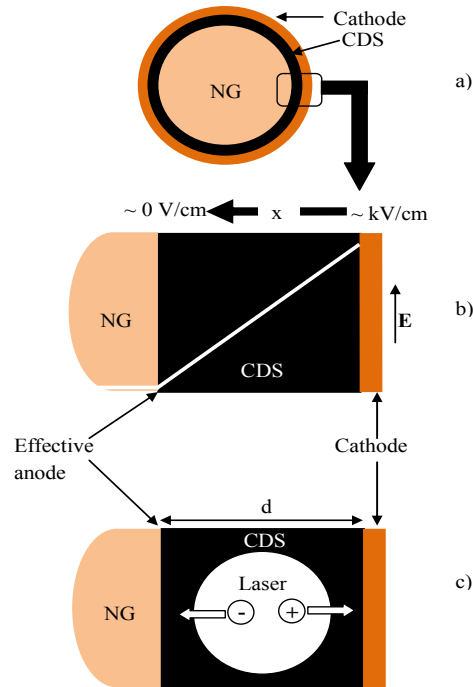


Fig. 7.3: a) Cross sectional view of the hollow cathode discharge, b) The electric field (E) distribution in the CDS. Maximum electric field at the cathode ($x = 0$) is $-2V_0/d$. V_0 is the voltage across the discharge, c) Laser induced photoionization in cathode dark space (CDS).

space (Fig. 7.3 c), photoions/electrons are efficiently extracted detected by the electric field present in the CDS. Typical collection time of the photoelectron is ~ 0.1 ns and that of photoions are in the range of few tens of ns [92,150] for a tightly focused laser beam near the cathode surface. When ionization is extended into the NG region, ion collection time extends to fraction of micro sec. In the photoionization process both the electron and ions are generated. It is very easy to identify the photoelectron signal which has large magnitude and short temporal width due to very fast collection of the electrons compare to the photoions.

In these experiments, the first-step laser wavelength (λ_1) was fixed by observing normal OG signal, across the discharge tube, when the laser beam was passed through the centre of the HCDT. The typical OG signal is shown in Fig. 7.4a. Fig. 7.4b is the temporal profile of the OG signal when DL₂ was tuned to the second-step transition wavelength (λ_2) and the laser beam position was moved close to the inner surface of the hollow cathode i.e. in the CDS. The photoionization signal appears only for those wavelengths of second dye laser when the energy of the second laser photon is more than half way between the first excited level and the ionization limit of uranium. Due to the presence of high electric field in the CDS region, the temporal shape and the duration of the normal OG signal has changed significantly, with steepening of the OG signal on the rising side. The increase in normal OG signal amplitude and reduction in its temporal width is, in general, due to the efficient and fast collection of charges in the CDS. In case of direct photoionization in CDS the electron current signal is followed by a tail of photo ions current, which may extend from few tens of ns to $\sim 1\mu\text{s}$ time scale depending upon the exact position of laser photoionization in the CDS. The merger of the direct photoionization signal tail into the rising side of the normal OG signal waveform could be the reason of the steepening. The PIOG signal, a spike at the beginning of normal OG signal (Fig. 7.4b), became more prominent. To observe the PIOG signal clearly, the oscilloscope time scale was expanded from μs to ns scale. The PIOG signal

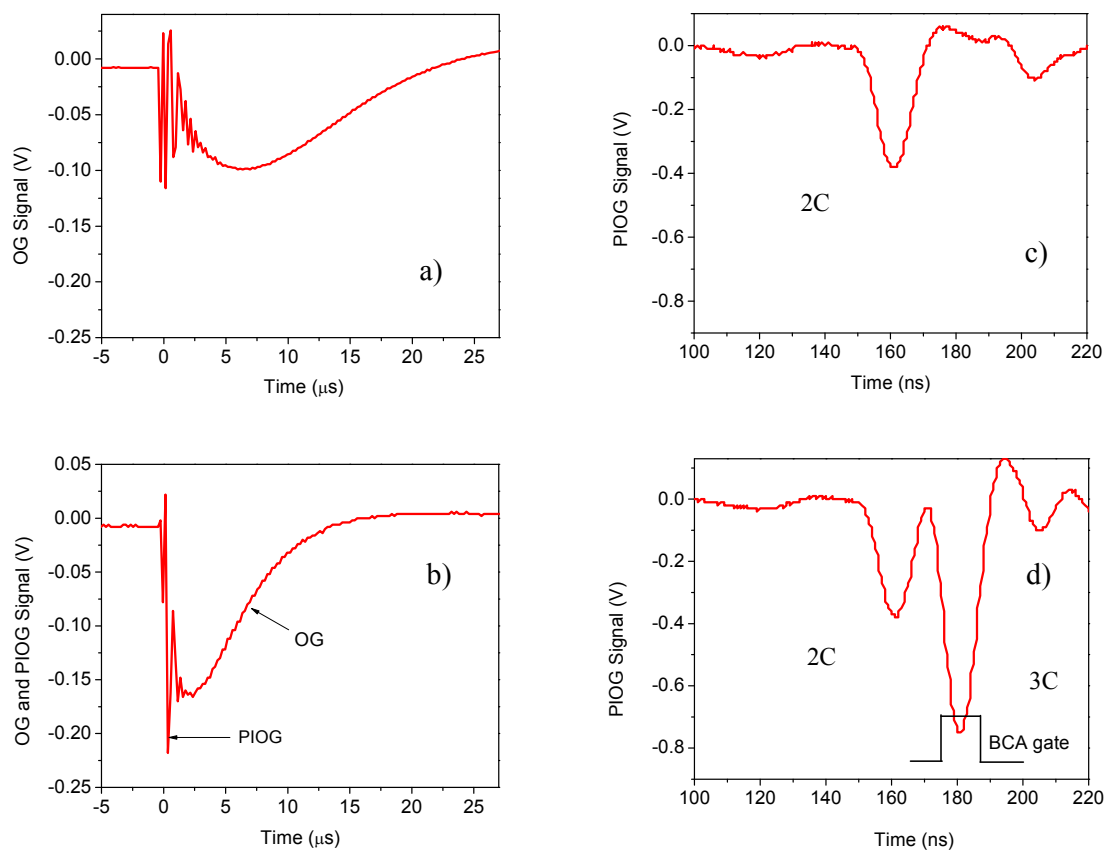


Fig. 7.4 : Typical temporal wave forms of a) normal OG signal, b) OG signal in presence of two-color three-photon photoionization, c) Two-color (2C) PIOG signal when the oscilloscope scale was stretched from μs to ns, and d) two-color and delayed three-color PIOG signal.

was optimized by adjusting the position of the HCDT parallel to the laser beam. The optimized two-color PIOG signal is shown in Fig. 7.4c. The temporal width (FWHM) of the PIOG signal is about 10 ns, which is, basically dictated by the temporal profile of the laser pulse. In the presence of the third laser, which was delayed by ~ 20 ns with respect to the second laser, the delayed non-resonant three-color PIOG signal appeared at almost all the wavelengths, in addition to the already present two-color three-photon PIOG signals. Fig. 7.4d shows the time-resolved two- and three-color PIOG signals. In hollow cathode discharges this is the first report of temporally resolving two- and three-color three-photon photoionization signals. As a result, it is possible to record a three-color spectrum with almost negligible background of two-color PIOG signal, thus attaining a very high signal to noise (S/N) ratio. The third laser power was attenuated considerably till the non-resonant three-color (PIOG) signal reduces to bare minimum. Whenever the third laser is tuned in resonance to AI levels of uranium a large enhancement in the PIOG signal, over the non resonant three-color signal, was observed. The enhancement in PIOG signal depends on the laser power and the particular scheme chosen. The optimized wavelength-dependent three-color PIOG signal was further processed using a boxcar averager and the three-color photoionization spectra of uranium was obtained by recording PIOG signal along with Fabry-Perot (FP) etalon fringes (free spectral range, $\text{FSR} \approx 0.5 \text{ cm}^{-1}$) by scanning the third laser wavelength (λ_3) in the energy region of interest. During these experiments, the laser wavelength scanning speed was 0.002 nm/sec. The three-color PIOG spectrum was calibrated by using known two-color three-photon photoionization features of uranium present in the three-color spectrum, which is known in the literature [13] with accuracy better than $\pm 0.2 \text{ cm}^{-1}$.

7.2.1 Characterization of the cathode dark space

To characterize the CDS, laser beams were focused in the CDS using Plano-convex lens of focal length 30 mm and position of the HCD was scanned in a direction perpendicular to the

laser beam direction using a micrometer based translation stage. Size of the laser beams in the CDS was about 0.4 mm. In case of focused laser beam, the OG and PIOG signals are well separated as shown in Fig 7.5a. Radial profile of the PIOG signal across the hollow cathode cylinder is shown in Fig. 7.5b. The asymmetry in the radial profile of the PIOG signal could be due to slight misalignment between the axis of the hollow cathode and direction of the

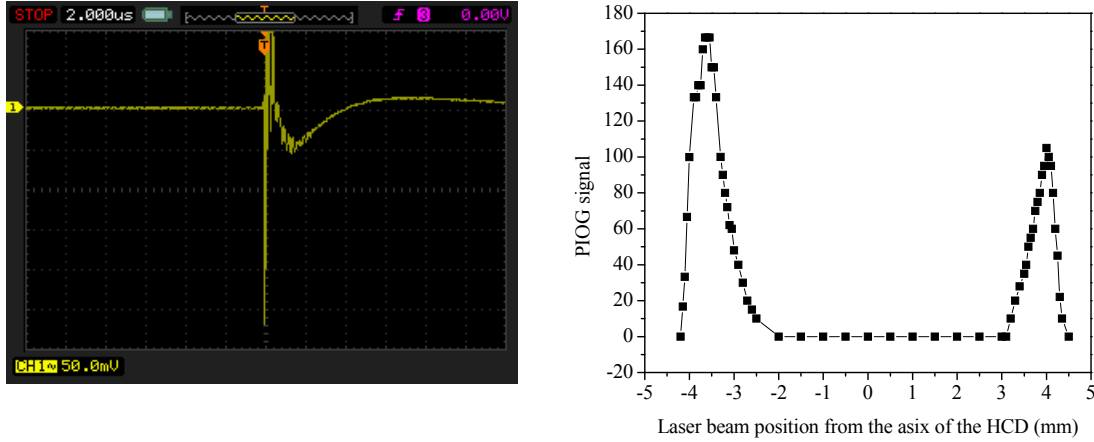


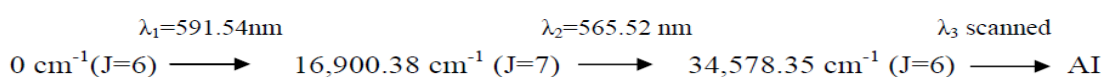
Fig. 7.5: a) Temporal profile of the PIOG and OG signal for focused laser beam, b) Radial profile of PIOG signal across the cylindrical cathode.

laser beams. It is evident from the figure that the PIOG signal is almost negligible throughout across the hollow cathode except for small regions very near to its inner surface, viz. the cathode dark space (CDS). It should be noted that for all spectroscopic experiments, we have used an aperture to select uniform part of the laser beams which fill CDS as well as part of the NG. Use of unfocused beams have several advantages over tightly focus laser beam such as: a) easier laser beam alignment with the CDS and overlap among the laser beams, b) higher signal to noise ratio due to large interaction volume, c) insignificant ionization due to nonresonant processes, d) minimum power broadening effect.

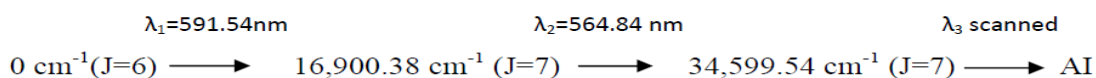
7.3 Study of autoionizing levels using three-color three-photon PIOG spectroscopy

The photoionization spectra of uranium investigated in the present studies, by performing three-color three-photon photoionization spectroscopy in the HCDT, are in the energy region 52,150-52,590 cm^{-1} , which lies much above the first ionization limit of uranium at 49,958.4 cm^{-1} . The excitation/photoionization pathways used in these investigations are:

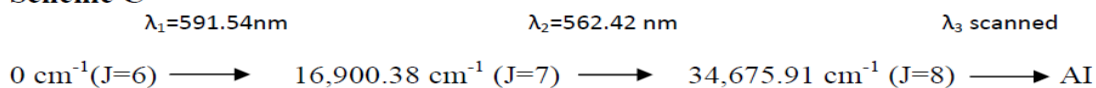
Scheme A



Scheme B



Scheme C



The first-step transition, $0 \text{ cm}^{-1} (J=6) \rightarrow 16,900.38 \text{ cm}^{-1} (J=7)$, starts from the ground state of uranium ($^5\text{L}_6$) and is common in all the pathways. The second-step transitions are chosen judiciously in such a way that it helps in reducing the uncertainty of the total angular momentum (J-value) of the AI states. The three-color PIOG spectra were recorded by fixing the first- and second-step dye lasers wavelengths at their respective values and scanning the third-step dye laser wavelength in the range 558-570 nm. The second-step transitions were chosen judiciously in such a way that it helps in reducing the uncertainty of the total angular momentum (J-value) of the AI states. The three-color PIOG spectra were recorded by fixing the first- and second-step dye lasers wavelengths at their respective values and scanning the third-step dye laser wavelength in the range 558-570 nm. A part of the three-color PIOG spectrum recorded using scheme A is shown in Fig. 7.6a. The three-color PIOG spectrum is a

composite one, containing single-, two- and three-color three-photon features, such as $3\lambda_3$, $\lambda_1+2\lambda_3$ and $\lambda_1+\lambda_2+\lambda_3$. The time delay between the three dye laser pulses will ensure that $\lambda_1+\lambda_3+\lambda_1$ or $\lambda_1+\lambda_3+\lambda_2$ type features do not appear in the spectra. In order to filter out single- and two-color a three-photon features from the three-color PIOG spectrum, the spectrum was also recorded with λ_2 blocked and is shown in Fig.7.6b. All those resonances, which disappear with the blocking of λ_2 , are three-color AI resonances for the transitions starting from the second-excited state of the excitation ladder. During these measurements the lasers per pulse energies were fixed at ~ 15 and ~ 200 μJ for the first and second steps respectively. Since the wavelength of the second step dye laser was acquired by observing two- color three-photon photoionization signal, the second dye laser energy was kept more than the saturation energy of the second step transition. The third step laser per pulse energy was kept intentionally low, variable in the range of 50-200 μJ , to minimize the power broadening of AI resonances. As a result a very few single- and two-color features have appeared in the three-color spectrum, because these features have strong dependence on laser power. This is quite evident from Fig. 7.7, when the same spectrum was repeated with a third-step laser power fifteen times higher than the one used in Fig. 7.6, while keeping the first and second steps laser powers constant. At higher laser power single- and two-color features have become more prominent but three-color spectrum has flattened due to power broadening of AI resonances and enhancement of non-resonant photoionization, which may lead to more uncertainties in the energy value measurements.

After filtering out the single- and two-color three-photon features from the three-color PIOG spectra, and ignoring all the peaks where the S/N ratio is less than three, we have identified sixty AI resonances of uranium. In general, the uncertainty in the measurements less than $\pm 0.5\text{cm}^{-1}$ has been achieved by recording the spectra several times. Some of the AI resonances, which are very broad ($>3\text{ cm}^{-1}$), the uncertainty in the measurements could be even more than

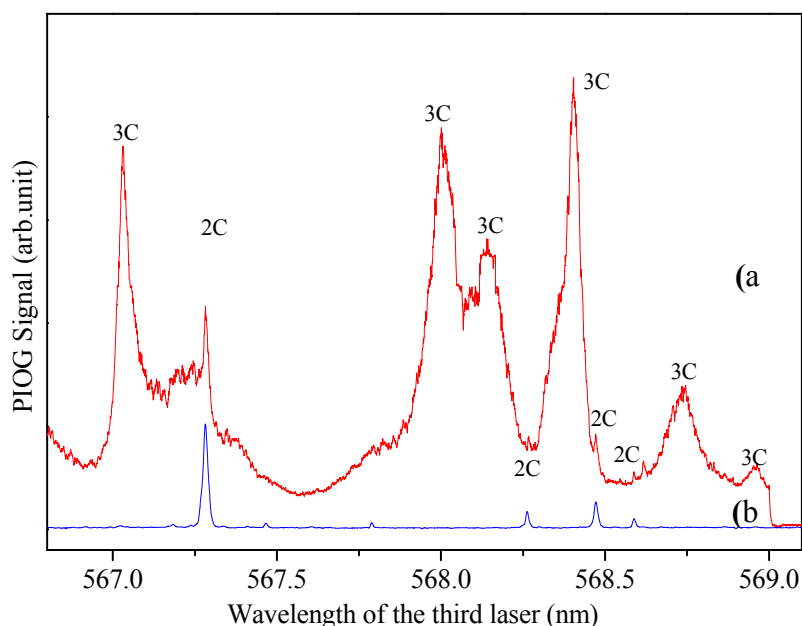


Fig. 7.6: a) A part of a three-color three-photon photoionization spectra of uranium recorded using scheme A in the energy region $52,148\text{--}52,216\text{ cm}^{-1}$. Third dye laser per pulse energy was $\sim 200\mu\text{J}$. 1C: Single-color; 2C: Two-color; 3C: three-color. b) Repeat of (a) with second dye laser (λ_2) blocked

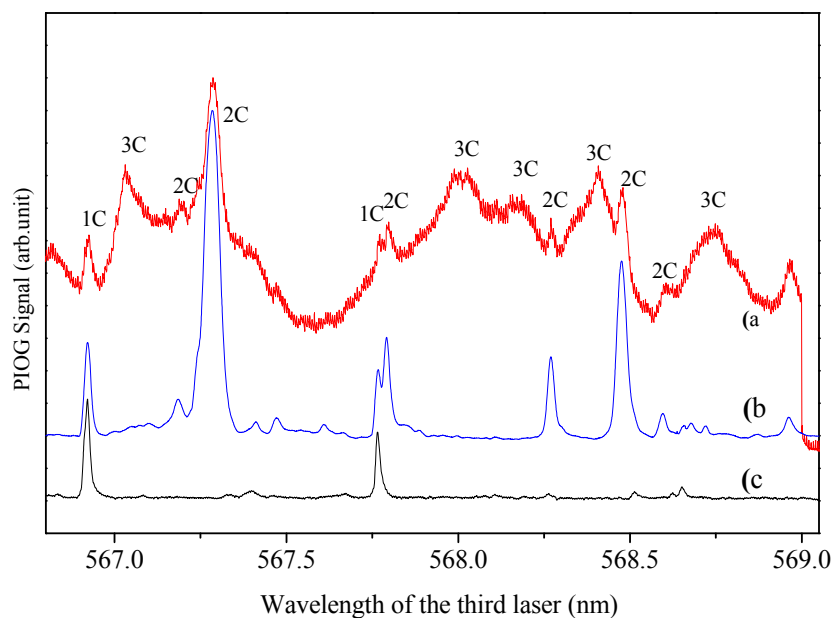


Fig. 7.7: a & b) Repeat of Fig. 7.6 a & b with third-step dye laser per pulse energy of $\sim 3\text{mJ}$, and c) Single-color three photon photoionization spectra of uranium recorded by blocking first and second lasers (λ_1 & λ_2).

Table 7. 1. New even-parity AI resonances of UI observed using three-color three-photon PIOG spectroscopy in HCDT.

Energy Level (cm ⁻¹)	Scheme	Probable J value	Energy Level (cm ⁻¹)	Scheme	Probable J value
52,156.3	A	5,6,7	52,325.0	C	7,8,9
52,162.1	B	6,7,8	52,334.2	B,C	7,8
52,166.5	A	5,6,7	52,341.6	B	6,7,8
52,167.8	B	6,7,8	52,343.7	C	7,8,9
52,175.4	A	5,6,7	52,345.9	C	7,8,9
52,179.6	A	5,6,7	52,351.0	B,C	7,8
52,208.1	A,B	6,7	52,362.8	B	6,7,8
52,216.4	B	6,7,8	52,366.3	A,C	7
52,221.4	A	5,6,7	52,371.6	A,C	7
52,225.6	A,C	7	52,387.6	A	5,6,7
52,230.1	B	6,7,8	52,390.7	B,C	7,8
52,233.8	B	6,7,8	52,393.9	A	5,6,7
52,234.2	C	7,8,9	52,404.6	C	7,8,9
52,235.8	A	5,6,7	52,417.0	A,B	6,7
52,243.7	A	5,6,7	52,428.8	C	7,8,9
52,244.6	B,C	7,8	52,437.6	A,C	7
52,251.0	A	5,6,7	52,445.6	B,C	7,8
52,254.0	A	5,6,7	52,450.6	A	5,6,7
52,258.8	B	6,7,8	52,464.7	C	7,8,9
52,262.6	C	7,8,9	52,479.5	C	7,8,9
52,265.1	A,B	6,7	52,485.2	B	6,7,8
52,274.4	C	7,8,9	52,499.2	C	7,8,9
52,281.1	C	7,8,9	52,507.1	C	7,8,9
52,300.6	C	7,8,9	52,527.1	C	7,8,9
52,303.1	A,B,C	7	52,538.2	C	7,8,9
52,309.0	C	7,8,9	52,562.0	C	7,8,9
52,311.1	B	6,7,8	52,568.6	C	7,8,9
52,314.8	C	7,8,9	52,570.9	C	7,8,9
52,320.1	A,B	6,7	52,585.0	C	7,8,9
52,320.9	C	7,8,9	52,588.7	C	7,8,9

this. Since there is no data reported in the literature on AI resonances of uranium in this energy region, all these resonances are new. According to the total angular momentum (J) selection rule, i.e. $\Delta J = 0, \pm 1$, we have assigned to them probable J-values. The resonances

with their energy values, the probable J-values, and the respective excitation scheme are given in Table 7.1. The AI resonances which have been observed through more than one excitation pathways, the ambiguity in their J-values have been reduced considerably. As one AI resonance which has been observed through all the three schemes and the other four AI resonances through schemes A&C, their J-value has been assigned uniquely i.e. 5. Nine other AI resonances which are common to schemes A&B and schemes B&C, the uncertainties in their J-values have been reduced to 6,7 and 7,8 respectively.

In HCDT, excited atoms may collide with electrons, ions and buffer gas atoms which may complicate the photoionization spectra. Also high electric field present in the cathode dark space may shift, split or completely vanish the autoionizing Rydberg levels which are very sensitive to the external electric field owing to the high polarizability of the atoms in that levels. The photoionization spectrum based on scheme A was measured simultaneously in HCDT by using PIOG technique and in the atomic beam coupled with TOF-MS. It has been found that both the spectra agree well within the measurement uncertainties. However, when we have recorded the photoionization spectra near the second ionizing limit from the second excited level $34,659.18 \text{ cm}^{-1}$ (discussed in the previous chapter) none of the AI Rydberg level were observed in the PIOG spectrum, thus PIOG technique is more suitable for studying valence autoionizing levels. It should be noted that PIOG spectroscopy may not be suitable with CW lasers due to collisional effects.

7.4 Measurement of isotope shift of odd-parity high lying levels (2nd excited levels) using two-color PIOG spectroscopy

Isotope shift of an energy level is defined as the difference in energies between different isotopes of the same element. Generally, transition isotope shift (IS) i.e. energy difference between spectral lines of isotopes is measured experimentally and the level IS of

the upper level of a transition is determined by adding the level IS of the lower level with that of measured IS. Accurate information on IS of high-lying levels is a pre-requisite in developing any isotope selective process based on multi-step resonance photoionization e. g. trace analysis of isotopes and laser isotope separation as it decides the selectivity of the desired isotope over the undesired one¹.

We have explored the potential of two-color PIOG spectroscopy to measure the isotope shifts (between ^{235}U and ^{238}U) of odd-parity high-lying (2^{nd} excited) levels of uranium in the energy region $33,950\text{ cm}^{-1}$ to $35,350\text{ cm}^{-1}$. High sensitivity achieved in PIOG spectroscopy due to efficient extraction in the CDS has enabled us to study the photoionization spectra of ^{235}U despite having the small abundance of 0.72%. The IS measurements in HCDT using multimode laser is often difficult due to large spectral width of the photoionization features resulting in poor resolution. For uranium this limitation can be overcome by choosing suitable first step transition. In case of atomic uranium, the isotope shifts of the second excited levels reported in the literature are mostly negative [74,91] i.e. energy of ^{235}U is more compared to ^{238}U . In this case, large transition isotope shift in the second step transition can be obtained by selecting first excited level with positive isotope shifts. We have chosen two 1^{st} step transitions (0 cm^{-1} - 17369.54 cm^{-1}) and (620.32 cm^{-1} - $17,468.26\text{ cm}^{-1}$) at wavelengths 575.560 nm and 593.382 nm, respectively where transition ISs are $+0.280\text{ cm}^{-1}$ and $+0.240\text{ cm}^{-1}$ respectively [74]. Based on these first step transitions two-color three-photon ($\lambda_1 + \lambda_2 + \lambda_2$) PIOG spectra were recorded by scanning λ_2 . The confirmation of the observed photoionisation resonances corresponding to ^{235}U were done by repeatedly recording the two-color photoionisation spectra for three different detunings of λ_1 : (i) in exact resonance with ^{235}U , ii) detuned from ^{235}U to towards ^{238}U by $\sim 0.08\text{ cm}^{-1}$ and iii) in exact resonance with ^{238}U . Possibility of overlapping single-color feature of ^{238}U at two-color feature of ^{235}U have been ruled out by measuring the single-color spectra of λ_2 .

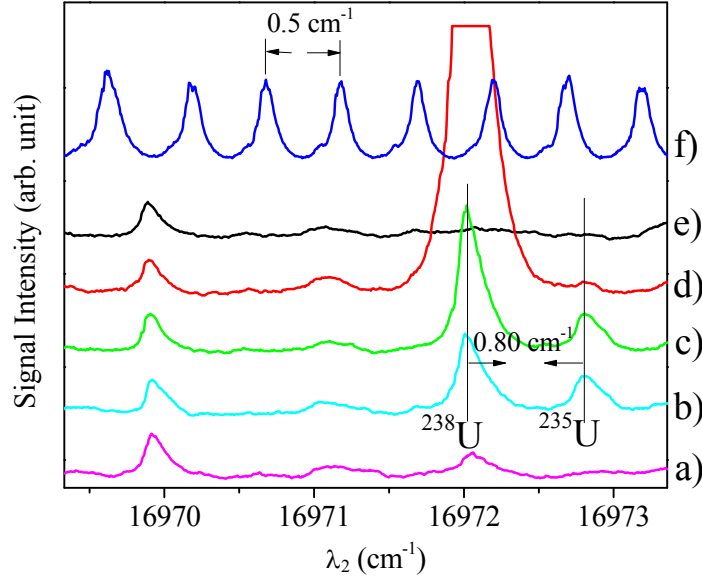


Fig. 7.8: A portion of the two color photoionization spectra for various λ_1 detuning (a) $+0.5 \text{ cm}^{-1}$, b) $+0.28 \text{ cm}^{-1}$, c) $+0.20 \text{ cm}^{-1}$ and d) $+0.00 \text{ cm}^{-1}$) from exact resonance of ^{238}U ($0 - 17369.54 \text{ cm}^{-1}$). e) single color spectrum, f) Fabry Perot etalon fringes ($\text{FSR}=0.5 \text{ cm}^{-1}$).

Fig. 7.8 shows a portion of two-color spectra for various detuning of 1st step laser wavelength. When λ_1 was detuned away from both U^{235} and ^{238}U resonance, almost no signal was observed (Fig. 7.8a). Fig. 7.8b shows the maximum ^{235}U signal when λ_1 was tuned in resonance to ^{235}U transition. On further tuning of λ_1 towards ^{238}U , the magnitude of ^{238}U signal has increased as shown in Fig. 7.8c. Fig. 7.8d shows further enhancement of ^{238}U signal and the ^{235}U signal almost diminishing to zero as λ_1 was tuned further towards ^{238}U . From these two-color photoionization spectra, the transition isotope shift i.e. difference in transition energies is measured. Isotope shift of the second excited level is determined by adding the measured 2nd step transitions isotope shifts to that of the 1st step transition isotope shift reported in the literature where ground state isotope shift is assumed to be zero. Using

similar methodology, we have measured IS of 18 odd-parity high-lying levels. The measured IS's relative to ground level are listed in Table 7.2 along with the reported values. The

Table 7.2. Measured values of isotope shifts of odd-parity levels.

Energy (cm ⁻¹)	Isotope shift (cm ⁻¹)	
	Present work	Reported
33,984.64	-0.59	-0.595 ^a
34,055.97	-0.42	
34,086.68	-0.46	-0.450 ^a
34,095.70	-0.37	
34,128.38	-0.48	-0.535 ^a
34,160.46	-0.77	-0.785 ^a
34,165.40	-0.50	
34,341.60	-0.52	
34,705.40	-0.52	-0.535 ^a
34,746.11	-0.52	-0.550 ^a
34,848.21	-0.51	-0.510 ^a
34,894.92	-0.51	-0.525 ^a
34,953.62	-0.52	-0.530 ^a
35,042.91	-0.57	
35,163.56	-0.47	
35,253.30	-0.51	
35,304.73	-0.54	-0.545 ^a
35,320.25	-0.55	

^a Miyabe et al.[91]

accuracy of these measurements is ± 0.03 cm⁻¹. It is evident from the table that the measured value of isotopes shifts using simple PIOG spectroscopy are matching well with that of Miyabe et al.[91] who have performed these measurements in atomic beam coupled with time-of-flight mass spectrometer. Due to its high sensitivity, PIOG spectroscopy could be useful to measure the isotope shifts of uranium as well as other refractory elements.

7.5 Measurement of photoexcitation/photoionization cross section of atomic uranium

The measurement of photoexcitation/ photoionization cross section of uranium has been presented in the chapter 5 by employing saturation of transition method in an atomic beam coupled with time-of-flight mass spectrometer (TOF-MS). By employing similar methodology as discussed in chapter 5 photoexcitation/ photoionization cross sections of a three-step photoionization scheme $0 \rightarrow 16,900.38 \rightarrow 34,599.54 \rightarrow 52,390.7 \text{ cm}^{-1}$ have been measured using PIOG spectroscopy and compared with our previous measurements in the atom beam. Here PIOG signal is studied as a function of laser photon fluence of the particular transition while keeping the photon fluence of the other two lasers is kept constant and the resultant curve is fitted with the solutions of the population rate equations. In this photoionization pathway, photoionization cross section at second step laser wavelength is very small compared to the second step photoexcitation cross section [110] and hence its effect on the measurement of second step cross section has been neglected. Fig. 7.9a, b and c shows the dependence of the delayed PIOG signal on the photon fluence of the first, second and the third step laser respectively. Respective photoexcitation/photoionization cross sections are given on the graph. The dependence of the delayed photoionization signal on the photon fluence of the first, second and the third step laser respectively, which has been presented in chapter 5, is shown in Fig. 7.9d, e and f. It is evident from the figures that both the measurements are matching well within the measurement uncertainties, thus demonstrating the potential of this technique. The small difference of photoexcitation/photoionization cross sections measured in the HCDT using PIOG technique in comparison to the values obtained in the atomic beam could be due to following reasons: a) collisional decay of excited atoms, b) Stark effect due to the presence of high electric fields ($\sim 4\text{kV/cm}$), c) larger Doppler width, and d) different optical thickness.

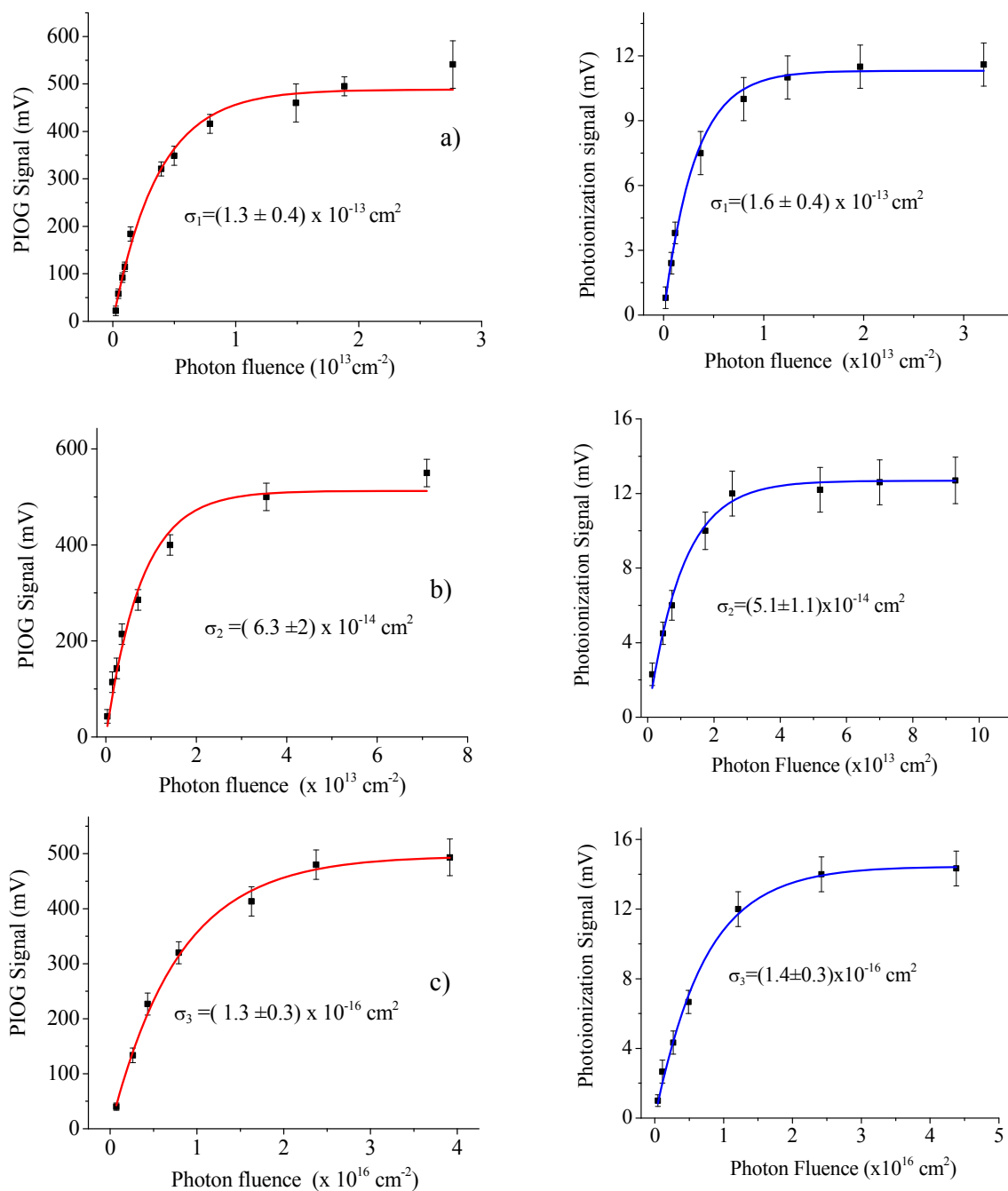


Fig. 7.9: Comparative studies of variation of photoionization signal as a function of particular laser photon fluence in HCDT using PIOG spectroscopy (a, b and c) and in TOF-MS (d, e and f) for first, second and third step respectively. Here, σ_1 and σ_2 represents the first and second step photoexcitation cross section. Also σ_3 represents the third step/photoionization cross section.

Chapter 8 - Conclusions and future scope of the work

8.1 Conclusions

The measurements of various atomic parameters of uranium such as radiative lifetimes, branching ratios, transition probabilities, photoexcitation/photoionization cross sections, energy values, total angular momenta by employing resonance ionization spectroscopy in an atomic beam coupled with a time-of-flight mass spectrometer (TOF-MS) using Nd:YAG pumped dye lasers have been presented in this thesis. The photoexcitation dynamics in a three-step photoionization process has been investigated using population rate equations. The atomic parameters like excited-level-to-excited-level transition probabilities, photoionization cross sections and J-values of autoionizing levels have been extracted by comparing the experimental measurements with the numerical calculations on the photoionization yield. As an alternate to the complex experimental setup consisting of an atomic beam source and a TOF-MS, the photoionization spectroscopy of uranium has also been carried out in a U-Ne hollow cathode discharge tube (HCDT), a simpler device, where HCDT has been used as a source of spectroscopic grade atomic vapors as well as photoion/photoelectron detector. The new spectroscopic data generated on atomic uranium could be useful for a) identification of efficient photoionization pathways for isotope selective photoionization processes of uranium, b) understanding of the photoexcitation dynamics, c) understanding of the energy level structure, above the first ionization limit.

Thesis begins with Chapter-1 which provides an introduction to resonance ionization spectroscopy. Chapter 2 describes the details of the experimental setup used for carrying out resonance ionization spectroscopy of atomic uranium.

In chapter 3, numerical study of excitation dynamics in a three-step photoionization process have been investigated for delayed and synchronous laser pulses using population rate equations. It has been found that the delayed laser pulses are more suitable for measuring photoexcitation and photoionization cross sections using saturation method. The effect of laser polarization on the photoionization yield has been studied. It was found that absolute photoionization yield for polarized and unpolarized light are significantly different but relative change in the photoionization yield for unpolarized and linearly polarized laser was found to be similar. The difference in the photoionization yield between unpolarized and linearly polarized laser found to be insignificant for photoionization schemes with increasing J-values.

In chapter 4 the measurements of branching-ratios and radiative lifetimes of atomic uranium by employing three-step delayed photoionization method have been presented. Radiative lifetimes of ten even-parity levels of uranium in the 15,500-19,000 cm^{-1} region and branching ratios of six transitions have been measured by three-step delayed photoionization technique. By combining experimentally measured radiative lifetimes and branching ratios, absolute transition probabilities of six transitions have been determined. The measured radiative lifetime values are in the range of 200 ns to 2,000 ns. The measured branching ratio values are in the range of 0.15 to 0.88 ns. Lifetimes of five levels and branching ratios of five transitions have been reported for the first time.

In chapter 5 measurements of excited-level to excited-level transition probabilities and photoionization cross sections of excited levels of atomic uranium using saturation method have been described. For the first and the third step transitions, two level systems were realized by temporally separating the laser pulses. As a test case, the cross section of 0 – 16,908.38 cm^{-1} transition was measured using saturation method and compared with the value obtained from β - τ

method which has been discussed in detail in chapter 4. Using this method photoionization cross section of ten strong autoionizing resonances from different excited levels has been measured. The measured photoionization cross sections are in the range of $1 \times 10^{-16} \text{ cm}^2$ to $1.2 \times 10^{-15} \text{ cm}^2$. However, in cases where the two-color three-photon process leads to photoionization; the assumption of an independent two level system for the second step is not valid. In these cases, photoexcitation dynamics in a three-step photoionization process of atomic uranium have been investigated by measuring two-color three-photon and delayed three-color three-photon photoionization signals as a function of the second-step photon fluence. Using population rate equation model these signals have been analyzed for the first time. The analysis has resulted in the determination of photoexcitation and photoionization cross-sections (σ_2 and σ_{2i}) simultaneously at seven values of λ_2 . From the measured values of σ_2 , we have obtained excited-level-to-excited-level transition probabilities of uranium. The transition probabilities $(9.47 \pm 2.1) \times 10^5 \text{ sec}^{-1}$ and $(49.6 \pm 13.4) \times 10^5 \text{ sec}^{-1}$ at the second-step laser wavelengths 564.84 nm and 562.95 nm respectively, match reasonably well with the values reported in the literature. Remaining five values of σ_2 and seven values of σ_{2i} are measured for the first time.

An exhaustive study of autoionizing levels of atomic uranium in the energy region up to $1,550 \text{ cm}^{-1}$ above the ionization limit has been presented in Chapter 6. Photoionization spectra have been measured using 11 different second excited levels. A detailed analysis of the photoionization spectra has revealed 346 of even-parity autoionizing levels including 199 new levels and a Rydberg series converging to the second lowest ionic level (${}^6\text{L}^{\circ}_{11/2}$) of uranium. Furthermore, by using laser polarization combinations method as well as method of total angular momentum selection rules, J-values of 72 AI levels have been assigned unambiguously. While

confirming the J-values of 16 AI levels reported previously, the unique J-values of 56 AI levels have been determined for the first time.

Chapter 7 describes three-color photoionization spectroscopy of atomic uranium using photoionization optogalvanic (PIOG) spectroscopy technique. Using this technique, photoionization spectra of uranium have been investigated systematically in the energy region 52,150-52,590 cm^{-1} through three different excitation pathways originating from its ground state ($^5L^o_6$). By analyzing the three-color photoionization spectra sixty new even-parity autoionization resonances of uranium have been identified and also assigned their probable total angular momentum (J) values according to the J-momentum selection rule. Out of these sixty AI resonances of uranium the J-values of five AI resonances have been assigned unambiguously and the uncertainties in the J-values for another nine AI resonances have been reduced considerably. In addition, the potential of PLOG technique has been explored to measure the isotope shifts of odd-parity high-lying levels and photoexcitation/photoionization cross section using saturation method as a test case.

8.2 Future scope of the work

Despite the extensive studies carried out in the present work for generating atomic data on uranium, the information on the atomic parameters is still far from complete. Thus, there is a scope to extend these measurements of atomic parameters to the new domains which have not been explored so far. The various spectroscopic techniques developed during the course of this work are universal thus can be applied to most of the elements in the periodic table.

The dense autoionizing spectra of uranium arising out of many optically active electrons could be studied more accurately by employing high resolution spectroscopy techniques such as

multi-color CW RIMS in an atomic beam. The shape of these autoionizing resonances, which is decided by the interference of the probability amplitudes of AI transitions with that of the continuum transitions, could be of interest from basic physics view point. High resolution spectroscopy employing multi-color CW-RIMS can be extended further to investigate the shape of these autoionizing resonances.

In the literature, there is not much information available on the hyperfine structure of the high-lying odd-parity atomic levels of uranium. This information is also important to develop multistep photoionization schemes for numerous applications mentioned earlier. Thus study of hyperfine structure using high resolution spectroscopic techniques will be of future interest.

Integrating a fluorescence detection system consisting of fast photomultiplier tube and monochromator with the existing TOF-MS, measurements of the radiative lifetimes of the high-lying levels and the branching ratios of the second step transitions can be done. By combining these radiative lifetimes and branching ratios, absolute transition probabilities of the second step transitions can be determined more accurately.

Appendix-1: Radiative lifetimes

Radiative lifetime is defined as the mean lifetime of an ensemble of atoms in the excited levels. Consider an assembly of atoms in which $N_k(0)$ atoms are excited into the level k at time $t = 0$. These excited atoms decay to a number of lower levels i through emission of radiation. In the absence of collisional depopulation, population replenishment by cascade from higher levels, etc., the population in level k decreases at the rate given by

$$-\frac{dN_k}{dt} = N_k \sum_i A_{ki} \quad (A1.1)$$

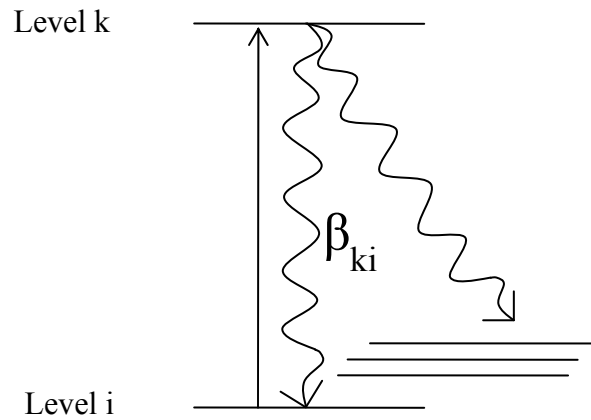


Fig. A-1: Decay of excited level k to various lower levels i .

where A_{ki} is the transition probability i.e. decay rate between the levels k and i . The reciprocal of the total decay rate is defined as radiative lifetime (τ_k) of the upper level k i.e.

$$\tau_k = \frac{1}{\sum_i A_{ki}} \quad (A1.2)$$

The solution of the equation (A1.1) is

$$N_k(t) = N_k(0)e^{\left(-\frac{t}{\tau_k}\right)} \quad (A1.3)$$

represents the exponential decay of the excited level population.

In a case where the excited level decays only through single channel, the transition probability can directly be determined from the measured lifetime of that level.

Appendix-2: Radiative lifetime of classical atom

In classical mechanics, excited electron inside an atom can be considered as an harmonically oscillating electric dipole. Energy (E) of the oscillating dipole decreases with time due to loss of power via dipole radiation. The differential equation for the loss of energy of the oscillating electric dipole can be expressed as [157]

$$-\frac{dE}{dt} = \frac{e^2 \omega^2}{6\pi \epsilon_0 m c^3} E \quad (A2.1)$$

where the ϵ_0 , m_e , c , e , ω represents permittivity of the free space, mass of the electrons, speed of the light in vacuum, electrical charge of electron and angular frequency of the light, respectively.

The solution of this equation is

$$E(t) = E(0)e^{-\gamma t} \quad (A2.2)$$

Where $\gamma = \frac{e^2 \omega^2}{6\pi \epsilon_0 m c^3}$ is the classical decay rate.

The mean lifetime of the excited state is given by

$$\tau = \frac{1}{\gamma} = \frac{6\pi \epsilon_0 m_e c^3}{e^2 \omega^2}. \quad (A2.3)$$

The classical value of the lifetime gives the fastest time in which the atom could decay on a given transition and this is often close to the observed lifetime for strong transitions.

Generally, radiative lifetimes of the excited levels of an atom, which can decay through electric dipole transition, are in the range of few ns to few hundreds of ns. In case of metastable states radiative lifetimes can be as high as fraction of a second. Metastable states decay through magnetic dipole or electric quadrupole transitions whose decay rates are five to eight order lesser

compared to the electric dipole allowed transitions [157]. The radiative decay of metastable states is difficult to observe in the laboratory due to the presence of other competitive nonradiative decay mechanisms.

According to quantum mechanics, electron can be excited to only some discrete energy levels which are the Eigen levels of the Hamiltonian of the system. The lifetimes of these levels should be infinite in principle lifetimes. But as per quantum electrodynamics due to vacuum fluctuation of electromagnetic field these levels are perturbed and hence have finite lifetimes. Thus, so called spontaneous radiative decays are induced by the vacuum fluctuation of the electromagnetic fields [158].

Appendix-3: Branching ratio

Excited atoms decay to various lower levels. Photons of different frequencies are emitted spontaneously in different decay channels. Branching ratio (β_{ki}) of a transition from level k to level i is defined as the ratio of emission intensity (I_{ki}) of i^{th} channel to the total emission intensity I , i.e.

$$\beta_{ki} = \frac{I_{ki}}{I} \quad (A3.1)$$

where $I = \sum_{i=1}^n I_{ki}$.

Appendix-4: Transition probability

Transition probability (A_{ki}) between level k to level i is defined as

$$A_{ki} = \frac{\beta_{ki}}{\tau_k} \quad (A4.1)$$

Where β_{ki} is the branching ratio and τ_k is the radiative lifetime of the k^{th} level. It is also known as Einstein coefficient of spontaneous emission. It represents the strength of a transition i.e. how easily electron can jump from one level to another level. As per quantum electrodynamics treatment of spontaneous emission, the transition probability between two degenerate levels can be expressed as [157]

$$A_{ki} = \frac{e^2 \omega_{ki}^3}{3\pi\epsilon_0 \hbar c^3} \frac{1}{g_k} \sum_{m_k m_i} |\langle i m_i | \vec{r} | k m_k \rangle|^2 \quad (A4.2)$$

Where e , ϵ_0 , \hbar , c represents electronic charge, free space permittivity, reduced Plank's constant and speed of light in vacuum respectively. ω_{ki} is the transition frequency and g_k is the degeneracy of the upper level k . Also m_i and m_k represents m^{th} magnetic quantum number of respective levels. \vec{r} stands for sum of the electrons position vector. The dipole moment (μ_{ki}) of the transition is defined as

$$\mu_{ki}^2 = \frac{e^2}{g_k} \sum_{m_k m_i} |\langle i m_i | \vec{r} | k m_k \rangle|^2 \quad (A4.3)$$

Thus the induced atomic dipole moment (μ_{ki}) is related to the transition probability through the following expressions

$$A_{ki} = \frac{\omega_{ki}^3 \mu_{ki}^2}{3\pi\epsilon_0 \hbar c^3}. \quad (A4.4)$$

The strength of an atomic transition is also often expressed in terms of oscillator strength (f_{ki}) which is a dimensionless quantity and is defined as the energy fraction of a classical dipole oscillator that can be ascribed to a transition and is expressed as [157]

$$f_{ki} = -\frac{A_{ki}}{3\gamma}. \quad (A4.5)$$

Minus sign represents emission and γ is the decay constant for one dimensional classical dipole oscillator.

Appendix-5: Photoexcitation cross section

The probability of interaction between atoms and photons is defined as photoexcitation cross section of a transition. It is expressed in units of area i.e. cm^2 . It is a derived quantity which depends on transition probability (A_{ki}), transition wavelength (λ) and spectral distribution of atoms and photons. Under monochromatic excitation and naturally broadened atomic absorption line width, photo excitation cross section below the saturation limits can be expressed as [26,52]

$$\sigma_{ik}(\omega) = \frac{\lambda^2}{4} A_{ki} \frac{g_k}{g_i} S(\omega) \quad (A5.1)$$

Where $S(\omega) = \frac{1}{2\pi} \frac{\Gamma}{((\omega_0 - \omega)^2 + \Gamma^2/4)}$ is the natural line shape, here $\Gamma = \frac{1}{\tau}$ is the total decay width (at FWHM), ω and ω_0 represents frequency of the laser and the transition, respectively. Also, g_k and g_i represents upper and lower level degeneracy. At resonance ($\omega = \omega_0$) the maximum value of the cross section is $\sim \lambda^2/2\pi$ for branching fraction of unity. In experimental conditions, this cross section value is reduced due to finite atomic absorption and laser line width. The line width of the atomic absorption is decided by various kinds of line broadening mechanisms. In case of collision less environment, the absorption line width is mainly decided by the Doppler width ($\Delta\omega_D$). With increasing absorption line width, probability of finding atoms per frequency interval decreases and thus peak cross section of the transition (at resonance) decreases according to the ratio of $\Gamma/\Delta\omega_D$. Similarly, for a fixed atomic absorption line width ($\Delta\omega_D$), average cross section of the transition decreases further with increasing laser line width ($\Delta\omega_L$) according to the ratio of $\Delta\omega_D/\Delta\omega_L$, provided $\Delta\omega_L > \Delta\omega_D$. Thus the maximum value of the

cross section is basically decided either by atomic absorption line width or laser line width whichever is larger.

In general photo excitation cross section for finite laser line width and atomic absorption line width is expressed as [26]

$$\sigma_{ki} = \frac{\lambda^2}{4} A_{ki} \frac{g_k}{g_i} \int_{-\infty}^{+\infty} S_{abs}(\omega) S_{laser}(\omega) d\omega \quad (A5.2)$$

where $S_{abs}(\omega)$ and $S_{laser}(\omega)$ represents the atomic absorption line profile and the laser line profile respectively. Basically, cross section depends on the integral of the product of the probabilities of finding atoms and photons over all the frequencies. In case of large laser line width ($\Delta\omega_L \gg \Delta\omega_D$ and Γ), the above expression for equal level degeneracies can be written as

$$\sigma_{ik} = \frac{\lambda^2}{4} \frac{A_{ki}}{\Delta\omega_L} \quad (A5.3)$$

Using this relation, the transition probability A_{ki} can be obtained from the measured value of the cross-section (σ_{ik}) for a known laser line width. For an efficient excitation of all the atoms within the atomic absorption line width, the laser line width should be greater or at least equal to the atomic absorption line width.

Bibliography

- [1] G. Herzberg, *Atomic Spectra and Atomic Structure*, Dover Publications, New York (1944).
- [2] S. Svanberg, *Atomic and Molecular Spectroscopy*, Lund (2003).
- [3] W. Demtroder, *Laser Spectroscopy: Basic concepts and Instrumentation*, Springer Verlag (2003).
- [4] V. S. Letokhov, *Laser photoionization spectroscopy*, Elsevier (2012).
- [5] B. A. Palmer, R. A. Keller, and R. Engleman Jr, Los Alamos Scientific Lab., USA (1980).
- [6] C. H. Corliss, *The Astrophysical Journal* **136**, 916 (1962).
- [7] B. Barbieri, N. Beverini, and A. Sasso, *Rev. Mod. Phys.* **62** (3), 603 (1990).
- [8] N. Piracha, M. Baig, S. Khan, and B. Suleman, *J. Phys. B: At. Mol. Opt. Phys.* **30** (5), 1151 (1997).
- [9] M. Ahmed, M. Zia, M. Baig, and B. Suleman, *J. Phys. B: At. Mol. Opt. Phys.* **30** (9), 2155 (1997).
- [10] B. Barbieri, N. Beverini, M. Galli, M. Inguscio, and F. Strumia, *Il Nuovo Cimento D* **4** (2), 172 (1984).
- [11] C. Barshick, R. Shaw, J. Young, and J. Ramsey, *Anal. Chem.* **66** (23), 4154 (1994).
- [12] J. Goldsmith and J. Lawler, *Contemp. Phys.* **22** (2), 235 (1981).
- [13] O. Kujirai and Y. Ogawa, *J. Phys. Soc. Jpn.* **67** (3), 1056 (1998).
- [14] O. Kujirai and Y. Ogawa, *J. Phys. Soc. Jpn.* **69** (9), 2845 (2000).
- [15] G. Hurst, M. Payne, S. Kramer, and J. Young, *Rev. Mod. Phys.* **51** (4), 767 (1979).
- [16] V. I. Balykin, G. Bekov, V. Letokhov, and V. Mishin, *Soviet Phys. U* **23** (10), 651 (1980).
- [17] E. Miron, R. David, G. Erez, S. Lavi, and L. Levin, *J. Opt. Soc. Am.* **69** (2), 256 (1979).
- [18] M. Oba, K. Akaoka, M. Miyabe, and I. Wakaida, *The Eur. Phys. J. D: At. Mol. Opt. Plas. Phys.* **10** (3), 349 (2000).
- [19] Y. Deniers, J. Gagne, C. Dreze, and P. Pianarosa, *J. Opt. Soc. Am. B* **3** (12), 1678 (1986).
- [20] A. Pulhani, M. Shah, V. Dev, and B. Suri, *J. Opt. Soc. Am. B* **22** (5), 1117 (2005).

- [21] S. D. Bergeson and J. Lawler, All faculty publications, 1823 (1993).
- [22] M. L. Shah, A. K. Pulhani, G. P. Gupta, and B. M. Suri, *J. Opt. Soc. Am. B* **27** (3), 423 (2010).
- [23] R. V. Ambartzumian and V. S. Letokhov, *Appl. Opt.* **11** (2), 354 (1972).
- [24] R. W. Solarz, J. A. Paisner, L. R. Carlson, C. A. May, and S. A. Johnson, UCRL-77590 (1975).
- [25] J. P. Young, G. S. Hurst, S. D. Kramer, and M. G. Payne, *Anal. Chem.* **51** (11), 1050A (1979).
- [26] V. S. Letokhov, V. I. Mishin, and A. A. Puretzky, *Prog. Quant. Electr.* **5**, 139 (1977).
- [27] R. W. Solarz, C. A. May, L. R. Carlson, E. F. Worden, S. A. Johnson, J. A. Paisner, and L. Radziemski Jr, *Phys. Rev. A* **14** (3), 1129 (1976).
- [28] A. Coste, R. Avril, P. Blancard, J. Chatelet, D. Lambert, J. Legre, S. Liberman, and J. Pinard, *J. Opt. Soc. Am.* **72** (1), 103 (1982).
- [29] E. F. Worden, R. W. Solarz, J. A. Paisner, and J. G. Conway, *J. Opt. Soc. Am.* **68** (1), 52 (1978).
- [30] N. Trautmann, *J. Alloys. Compd.* **213**, 28 (1994).
- [31] J. R. Peterson, N. Erdmann, M. Nunnemann, K. Eberhardt, G. Huber, J. V. Kratz, G. Passler, O. Stetzer, P. Thörle, N. Trautmann, and A. Waldek *J. Alloys. Compd.* **271**, 876 (1998).
- [32] M. Miyabe, M. Oba, and I. Wakaida, *J. Phys. B: At. Mol. Opt. Phys.* **31** (20), 4559 (1998).
- [33] J. Roßnagel, S. Raeder, A. Hakimi, R. Ferrer, N. Trautmann, and K. Wendt, *Phys. Rev. A* **85** (1), 012525 (2012).
- [34] R. V. Ambartzumian, N. P. Furzikov, V. S. Letokhov, and A. A. Puretsky, *Appl. Phys.* **9** (4), 335 (1976).
- [35] S. Gilbert, M. Noecker, and C. Wieman, *Phys. Rev. A* **29** (6), 3150 (1984).
- [36] A. Smith, J. Goldsmith, D. Nitz, and S. Smith, *Phys. Rev. A* **22** (2), 577 (1980).
- [37] S. Kröll and W. K. Bischel, *Phys. Rev. A* **41** (3), 1340 (1990).
- [38] P. Benetti, A. Tomaselli, and P. Zampetti, presented at the 1986 European Conf on Optics, Optical Systems and Applications, 1987 (unpublished).
- [39] N. Amin, S. Mahmood, M. Anwar-ul-Haq, M. Riaz, and M. Baig, *The Eur. Phys. J. D: At. Mol. Opt. Plas. Phys.* **37** (1), 23 (2006).
- [40] M. Kalyar, M. Rafiq, and M. Baig, *J. Phys. B: At. Mol. Opt. Phys.* **40** (12), 2307 (2007).

- [41] N. Amin, S. Mahmood, S. Haq, M. Kalyar, M. Rafiq, and M. Baig, *JQSRT* **109** (5), 863 (2008).
- [42] R. Cong, Y. Cheng, J. Yang, J. Fan, G. Yao, X. Ji, X. Zheng, and Z. Cui, *J. Appl. Phys.* **106** (1), 013103 (2009).
- [43] M. Rafiq, S. Hussain, M. Saleem, M. Kalyar, and M. Baig, *J. Phys. B: At. Mol. Opt. Phys.* **40** (12), 2291 (2007).
- [44] M. Saleem, S. Hussain, M. Rafiq, and M. Baig, *J. Phys. B: At. Mol. Opt. Phys.* **39** (24), 5025 (2006).
- [45] M. L. Shah, G. P. Gupta, V. Dev, B. Dikshit, M. S. Bhatia, and B. M. Suri, *J. Opt. Soc. Am. B* **29** (4), 600 (2012).
- [46] A. Yar, R. Ali, and M. A. Baig, *Phys. Rev. A* **87** (4), 045401 (2013).
- [47] B. Cheal and K. Flanagan, *J. Phys. G: Nucl. Part. Phys.* **37** (11), 113101 (2010).
- [48] J. Billowes and P. Campbell, *J. Phys. G: Nucl. Part. Phys.* **21** (6), 707 (1995).
- [49] V. Fedosseev, Y. Kudryavtsev, and V. Mishin, *Phys. Scr.* **85** (5), 058104 (2012).
- [50] M. Nunnemann, N. Erdmann, H.-U. Hasse, G. Huber, J. Kratz, P. Kunz, A. Mansel, G. Passler, O. Stetzer, and N. Trautmann, *J. Alloys. Compd.* **271**, 45 (1998).
- [51] S. Mayo, T. Lucatorto, and G. Luther, *Anal. Chem.* **54** (3), 553 (1982).
- [52] W. Ruster, F. Ames, H.-J. Kluge, E.-W. Otten, D. Rehklaue, F. Scheerer, G. Herrmann, C. Mühlecke, J. Riegel, and H. Rimke, P. Sattelberger and N. Trautmann, *Nucl. Instrum. Methods Phys. Res. A* **281** (3), 547 (1989).
- [53] J. Riegel, R. Deissenberger, G. Herrmann, S. Koehler, P. Sattelberger, N. Trautmann, H. Wendeler, F. Ames, H.-J. Kluge, and F. Scheerer, *Appl. Phys. B* **56** (5), 275 (1993).
- [54] H.-J. Kluge, B. Bushaw, G. Passler, K. Wendt, and N. Trautmann, *Fresenius J. Anal. Chem.* **350** (4-5), 323 (1994).
- [55] K. Wendt, G. Bhowmick, B. Bushaw, G. Herrmann, J. Kratz, J. Lantzsch, P. Müller, W. Nörtershäuser, E.-W. Otten, and R. Schwalbach, *Radiochim. Acta* **79** (3), 183 (1997).
- [56] N. Trautmann, G. Passler, and K. Wendt, *Anal. and Bio-anal. Chem.* **378** (2), 348 (2004).
- [57] V S Letokhov, C B Moore, *Sov. J. Quantum. Electron.* **6** (2), 129 (1976)
- [58] N. Karlov and A. Prokhorov, *UsFiN* **118**, 583 (1976).
- [59] N. Karlov, B. Krynetskii, V. Mishin, and A. Prokhorov, *Appl. Opt.* **17** (6), 856 (1978).
- [60] P. T. Greenland, *Contemp. Phys.* **31** (6), 405 (1990).

- [61] T. Arisawa, Y. Maruyama, Y. Suzuki, M. Kato, Y. Naruse, JAERI M-83, 124 (1983).
- [62] H. Park, D. Kwon, Y. Cha, S. Nam, T. Kim, J. Han, Y. Rhee, D. Jeong, and C. Kim, J. Korean Phys. Soc. **49** (91), 382 (2006).
- [63] D. Donohue, J. Young, and D. Smith, Appl. Spectrosc. **39** (1), 93 (1985).
- [64] V. K. Mago, B. Lal, A. K. Ray, P. R. K. Rao, and S. D. Sharma, J. Phys. B: At. Mol. Opt. Phys. **20** (24), 6531 (1987).
- [65] K. Dasgupta, K. G. Manohar, P. N. Bajaj, B. M. Suri, R. K. Talukdar, P. K. Chakraborti, and P. R. K. Rao, J. Opt. Soc. Am. B **5** (6), 1257 (1988).
- [66] A. K. Ray, B. Lal, V. K. Mago, and P. R. K. Rao, J. Opt. Soc. Am. B **9** (11), 1979 (1992).
- [67] A. I. Gomonai and O. I. Plekan, J. Phys. B: At. Mol. Opt. Phys. **36**(20), 4155 (2003).
- [68] B. A. Bushaw, W. Nörtershäuser, K. Blaum, and K. Wendt, Spectrochim. Acta, Part B **58** (6), 1083 (2003).
- [69] M. Payne, L. Deng, and N. Thonnard, Rev. Sci. Instrum. **65** (8), 2433 (1994).
- [70] A. N. Tkachev and S. I. Yakovlenko, Quantum Electro. **33** (7), 581 (2003).
- [71] B. A. Bushaw, S. Raeder, S. L. Ziegler, and K. Wendt, Spectrochim. Acta, Part B **62** (5), 485 (2007).
- [72] W. DeGraffenreid, S. C. Campbell, and C. J. Sansonetti, J. Opt. Soc. Am. B **29** (7), 1580 (2012).
- [73] W. DeGraffenreid and C. J. Sansonetti, J. Opt. Soc. Am. B **19** (7), 1711 (2002).
- [74] J. Blaise and L. J. Radziemski, J. Opt. Soc. Am. **66**, 644 (1976).
- [75] C. Kiess, C. Humphreys, and D. Laun, J. Res. Natl. Bur. Stand. **37** (1), 57 (1946).
- [76] K. Rajnak, Phys. Rev. A **14** (6), 1979 (1976).
- [77] R. D. Cowan, J. Opt. Soc. Am. **58** (6), 808 (1968).
- [78] K. Rajnak and M. Fred, J. Opt. Soc. Am. **67** (10), 1314 (1977).
- [79] S. A. Tuccio, J. W. Dubrin, O. G. Peterson, and B. B. Snavely, VIII International conference on Quantum electronics, San Francisco, 1974.
- [80] G. Janes, I. Itzkan, C. Pike, R. Levy, and L. Levin, IEEE J. Quantum Electron. **12** (2), 111 (1976).
- [81] L. R. Carlson, J. A. Paisner, E. F. Worden, S. A. Johnson, C. A. May, and R. W. Solarz, J. Opt. Soc. Am. **66** (8), 846 (1976).

- [82] L. R. Carlson, S. A. Johnson, E. F. Worden, C. A. May, R. W. Solarz, and J. A. Paisner, *Opt. Commun.* **21** (1), 116 (1977).
- [83] M. Miyabe, M. Oba, and I. Wakaida, *J. Phys. B: At. Mol. Opt. Phys.* **33** (21), 4957 (2000).
- [84] V. K. Mago, B. Lal, A. K. Ray, R. Kapoor, S. D. Sharma, and P. R. K. Rao, *J. Phys. B: At. Mol. Opt. Phys.* **20** (22), 6021 (1987).
- [85] B. M. Suri, K. Dasgupta, P. N. Bajaj, K. G. Manohar, R. K. Talukdar, P. K. Chakraborti, and P. R. K. Rao, *J. Opt. Soc. Am. B* **4** (11), 1835 (1987).
- [86] P. N. Bajaj, K. G. Manohar, B. M. Suri, K. Dasgupta, R. K. Talukdar, P. K. Chakraborti, and P. R. K. Rao, *Appl. Phys. B* **47** (1), 55 (1988).
- [87] V. K. Mago, A. K. Ray, B. Lal, and P. R. K. Rao, *J. Phys. B: At. Mol. Opt. Phys.* **21** (6), 955 (1988).
- [88] G. Shi, H. Du, S. Wang, C. Jin, and Z. Li, *J. Opt. Soc. Am. B* **17** (1), 103 (2000).
- [89] S. Raeder, S. Fies, T. Gottwald, C. Mattolat, S. Rothe, and K. Wendt, *Hyperfine Interact.* **196** (1-3), 71 (2010).
- [90] M. Smyth, L. Green, F. Sopchyshyn, and P. Leeson, *J. Phys. B: At. Mol. Opt. Phys.* **24** (23), 4887 (1991).
- [91] M. Miyabe, M. Oba, and I. Wakaida, *J. Phys. Soc. Jpn.* **70** (5), 1315 (2001).
- [92] S. Lévesque, J.-M. Gagné, and F. Babin, *Can. J. Phys.* **76** (3), 207 (1998).
- [93] V. Dev, M. L. Shah, A. K. Pulhani, and B. M. Suri, *Appl. Phys. B* **80** (4-5), 587 (2005).
- [94] K. G. Manohar, P. N. Bajaj, B. M. Suri, R. K. Talukdar, K. Dasgupta, P. K. Chakraborti, and P. R. K. Rao, *Appl. Phys. B* **48** (6), 525 (1989).
- [95] M. Miyabe, C. Geppert, M. Oba, I. Wakaida, and K. Wendt, *J. Phys. B: At. Mol. Opt. Phys.* **35** (18), 3865 (2002).
- [96] N. Rodrigues, J. Neri, C. Schwab, C. Silveira, M. Destro, R. Riva, and A. Mirage, *J. Phys. B: At. Mol. Opt. Phys.* **33** (18), 3685 (2000).
- [97] P. G. Schumann, K. Wendt, and B. A. Bushaw, *Spectrochim. Acta, Part B* **60** (11), 1402 (2005).
- [98] A. P. Marathe, K. G. Manohar, and B. N. Jagatap, *J. Phys. Conf. Ser.* **80**, 012032 (2007).
- [99] M. L. Shah, P. K. Mandal, V. Dev, and B. M. Suri, *J. Opt. Soc. Am. B* **29** (7), 1625 (2012).
- [100] D. Wort, C. Brown, and R. Plumbe, *J. Phys. E: Scientific Instruments* **12** (9), 829 (1979).

- [101] R. Avril, A. Ginibre, and A. Petit, *Z. Phys. D: At., Mol. clusters* **29** (2), 91 (1994).
- [102] M. Oba, K. Akaoka, M. Miyabe, and I. Wakaida, *Eur. Phys. J. D: At. Mol. Opt. Plas. Phys.* **21** (3), 255 (2002).
- [103] A. Petit, R. Avril, D. L'Hermite, and A. Pailloux, *Phys. Scr.* **2002** (T100), 114 (2002).
- [104] R. Avril, A. D. Petit, J. Radwan, and E. Vors, *Proceedings of SPIE*, **1859**, 38 (1993)
- [105] I. V. Chernushevich, A. V. Loboda, and B. A. Thomson, *J. Mass Spectrom.* **36** (8), 849 (2001).
- [106] R. J. Cotter, *Time-of-flight mass spectrometry*, ACS Publications (1993).
- [107] W. Wiley and I. H. McLaren, *Rev. Sci. Instrum.* **26** (12), 1150 (1955).
- [108] J. R. Ackerhalt and B. W. Shore, *Phys. Rev. A* **16** (1), 277 (1977).
- [109] G. Gupta and B. Suri, *J. Phys. D: Appl. Phys.* **35** (12), 1319 (2002).
- [110] P. K. Mandal, A. C. Sahoo, R. C. Das, M. L. Shah, A. K. Pulhani, K. G. Manohar, and Vas Dev, *Appl. Phys. B* **120** (4), 751 (2015).
- [111] C. H. Corliss, *J. Res. Natl. Bur. Stand., A* **80** (1), 1 (1976).
- [112] P. A. Voigt, *Phys. Rev. A* **11** (6), 1845 (1975).
- [113] G. Henrion, M. Fabry, and M. Remy, *J. Quant. Spectrosc. Radiat. Transfer* **37** (5), 477 (1987).
- [114] T. M. Bieniewski, *J. Opt. Soc. Am. B* **1** (2), 300 (1984).
- [115] R. Kapoor and G. D. Saksena, *Phys. Rev. Lett.* **61** (13), 1481 (1988).
- [116] R. Kapoor and G. D. Saksena, *J. Opt. Soc. Am. B* **6** (9), 1623 (1989).
- [117] J. Z. Klose, *Phys. Rev. A* **11** (6), 1840 (1975).
- [118] J. Z. Klose and P. Voigt, *Phys. Rev. A* **16** (5), 2032 (1977).
- [119] L. Hackel and M. Rushford, *J. Opt. Soc. Am.* **68** (8), 1084 (1978).
- [120] S. E. Bisson, E. F. Worden, J. G. Conway, B. Comaskey, J. A. Stockdale, and F. Nehring, *J. Opt. Soc. Am. B* **8** (8), 1545 (1991).
- [121] E. Benck, J. Lawler, and J. Dakin, *J. Opt. Soc. Am. B* **6** (1), 11 (1989).
- [122] J. Lawler, G. Bonvallet, and C. Sneden, *The Astrophysical Journal* **556** (1), 452 (2001).
- [123] P. T. Greenland, D. N. Travis, and D. J. H. Wort, *J. Phys. B: At. Mol. Opt. Phys.* **24** (6), 1287 (1991).

- [124] M. Miyabe, I. Wakaida, and T. Arisawa, *Z. Phys. D: At., Mol. clusters* **39** (3), 181 (1997).
- [125] S. E. Bisson, B. Comaskey, and E. F. Worden, *J. Opt. Soc. Am. B* **12** (2), 193 (1995).
- [126] P. Ramanujam, *Phys. Rev. Lett.* **39** (19), 1192 (1977).
- [127] O. Poulsen, T. Andersen, S. Bentzen, and U. Nielsen, *Phys. Rev. A* **24** (5), 2523 (1981).
- [128] R. C. Das, P. K. Mandal, M. L. Shah, A. U. Seema, D. R. Rathod, Vas Dev, K. G. Manohar, and B. M. Suri, *J. Quant. Spectrosc. Radiat. Transfer* **113** (5), 382 (2012).
- [129] R. W. Solartz et al., UCRL 50021, 494 (1974).
- [130] P. T. Greenland, D. N. Travis, and D. J. H. Wort, *J. Phys. B: At. Mol. Opt. Phys.* **23** (17), 2945 (1990).
- [131] P. K. Mandal, A. C. Sahoo, R. C. Das, M. L. Shah, and Vas Dev, *Appl. Phys. B* **123** (6), 192 (2017).
- [132] P. K. Mandal, A. U. Seema, R. C. Das, M. L. Shah, Vas Dev, and B. M. Suri, *JQSRT* **124**, 79 (2013).
- [133] T. Jayasekharan, M. A. N. Razvi, and G. L. Bhale, *J. Phys. B: At. Mol. Opt. Phys.* **33** (16), 3123 (2000).
- [134] E. F. Worden, L. R. Carlson, S. A. Johnson, J. A. Paisner, and R. W. Solarz, *J. Opt. Soc. Am. B* **10**, 1998 (1993).
- [135] C. Grüning, G. Huber, P. Klopp, J. Kratz, P. Kunz, G. Passler, N. Trautmann, A. Waldek, and K. Wendt, *Int. J. Mass spectrom.* **235** (2), 171 (2004).
- [136] K. G. Manohar, Doctoral thesis, Mumbai university (1991).
- [137] P. Feldman and R. Novick, *Phys. Rev. Lett.* **11** (6), 278 (1963).
- [138] P. Feldman and R. Novick, *Phys. Rev.* **160** (1), 143 (1967).
- [139] G. Bekov, V. Letokhov, O. Matveev, and V. Mishin, *JETP Letters* **28**, 283 (1978).
- [140] M. L. Shah, A. C. Sahoo, A. K. Pulhani, G. P. Gupta, B. Dikshit, M. S. Bhatia, and B. M. Suri, *JQSRT* **142**, 9 (2014).
- [141] P. T. Greenland, *J. Phys. B: At. Mol. Opt. Phys.* **21** (24), 4117 (1988).
- [142] M. Miyabe, I. Wakaida, and T. Arisawa, Resonance ionization spectroscopy for AVLIS JAERI-Conf-95-005(v2), Japan (1995).
- [143] U. Fano, *Phys. Rev.* **124** (6), 1866 (1961).

- [144] V. I. Mishin, G. G. Lombardi, J. W. Cooper, and D. E. Kelleher Phys. Rev. A **35**, 1664 (1986).
- [145] A. K. Ray, V. K. Mago, B. Lal, and P. R. K. Rao, J. Opt. Soc. Am. B **7** (2), 145 (1990).
- [146] K. Nittoh, K. Nakayama, J. Watanabe, H. Adachi, H. Ueda, and T. Yoshida, J. Phys. B: At. Mol. Opt. Phys. **27** (10), 1955 (1994).
- [147] L. Green, G. McRae, and P. Rochefort, Phys. Rev. A **47** (6), 4946 (1993).
- [148] P. J. Slevin and W. W. Harrison, Appl. Spec. Rev. **10** (2), 201 (1975).
- [149] W. Jones and A. Walsh, Spectrochim. Acta **16** (3), 249 (1960).
- [150] M. Broglia, F. Catoni, and P. Zampetti, Le Journal de Physique Colloques **44** (C7), C7 479 (1983).
- [151] S. Lévesque, J. Gagné, and F. Babin, J. Phys. B: At. Mol. Opt. Phys. **30** (5), 1331 (1997).
- [152] F. Babin and J.-M. Gagné, Appl. Phys. B **54** (1), 35 (1992).
- [153] M. Broglia, F. Catoni, and P. Zampetti, Le Journal de Physique Colloques **44** (C7), C7 251 (1983).
- [154] G. Stockhausen, W. Mende, and M. Kock, J. Phys. B: At. Mol. Opt. Phys. **29** (4), 665 (1996).
- [155] J. Lee, D. Y. Jeong, and Y. Rhee, AIP Conf. Proc., 1997.
- [156] E. Guyadec, J. Ravoire, R. Botter, F. Lambert and A. Petit, Optics comm. **76**, 34 (1990).
- [157] A. Corney, *Atomic and laser spectroscopy*, Clarendon Press Oxford (1978).
- [158] M. Auzinsh, D. Budker, and S. Rochester, *Optically polarized atoms: understanding light-atom interactions*. Oxford University Press (2010).